Calorimeter calibration and search for R-hadrons at $\sqrt{s} = 7$ TeV with the ATLAS experiment

Thesis submitted for the Master's degree in physics by

Martin Spangenberg

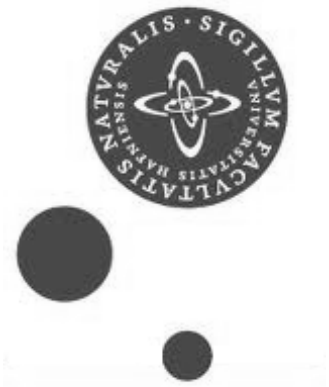

Niels Bohr Institute
University of Copenhagen
November 7, 2012

Academic advisor
Troels C. Petersen

Summary

This thesis presents a search for gluino-based R-hadrons predicted by Split Supersymmetry. One of the most potent discriminators in the search for heavy particles is the speed β, which is expected to be considerably lower than for any Standard Model particles. Emphasis is placed on the development of this discriminator, which includes the calibration of reconstructed calorimeter time-of-flight measurements, combination of the resulting β values and a final σ_β error correction based on pull distributions.

The refined discriminator is subsequently applied in the R-hadron search alongside other variables having discrimination power by optimising the signal significance through comparison to the expected background in a side-band to the signal region. Background estimation is done using a data-driven method.

Using the 2011 ATLAS data set comprising 4.7 fb^{-1} of data collected at a center-of-mass energy of $\sqrt{s} = 7$ TeV, the search has placed upper 95% CLs limits on the production cross sections of R-hadrons with masses ranging from 200 MeV to 1.5 TeV. Comparing the upper limits on production cross sections with the theoretically predicted values at each mass point yields a competitive lower limit on the gluino mass of $m_{\tilde{g}} > 981$ GeV.

Resumé

Denne afhandling udforsker den mulige eksistens af gluinobaserede R-hadroner, som er forudsagt af Supersymmetri. En af de stærkeste diskriminatorer ved eftersøgningen af tunge partikler er hastigheden β, som forventes at være betydeligt lavere end for alle partikler i Standardmodellen. Der lægges vægt på udviklingen af denne diskriminator, hvilket inkluderer kalibration af rekonstruerede time-of-flight målinger i kalorimetrene, kombination af de resulterende β-værdier og en endelig σ_β fejlkorrektion baseret på pull-fordelinger.

Den tilrettede diskriminator bliver efterfølgende anvendt på lige fod med andre variable med potentiale for diskrimination ved at optimere signalsignifikansen gennem en sammenligning med den forventede baggrund uden for signalregionen. Estimering af baggrund udføres udelukkende ved brug af data.

Ved at benytte 2011 datasættet fra ATLAS, som omfatter 4.7 fb^{-1} data indsamlet ved en energi på $\sqrt{s} = 7$ TeV, er der sat øvre 95% CLs grænser for produktionstværsnittet for R-hadroner med masser der spænder fra 200 GeV til 1.5 TeV. Ved at sammenligne de øvre grænser for produktionstværsnit med de teoretisk forudsagte værdier findes en konkurrencedygtig nedre grænse på gluino-massen på $m_{\tilde{g}} > 981$ GeV.

Contents

Introduction

Elementary particle physics is the study of the smallest known building blocks of matter in the universe and their interactions. Three of the four known forces of Nature, excluding gravity, are included in the comprehensive theoretical framework called the Standard Model, which is the current culmination of our understanding of the fundamental constituents of the universe. It combines many breakthroughs of the past, including Special Relativity and Quantum Mechanics. The former describes matter travelling at velocities close to the speed of light and at high energies, while the latter gives a fundamentally statistical description of the world at the scale of atoms and below. The combination of these insights has led to the introduction of Quantum Field Theory, which explains the observed phenomena though fundamental fields with their excitations representing the elementary particles.

The ultimate goal is the unification of all forces, just like the electromagnetic and weak forces have been shown to unify at high energies. In this respect the Standard Model is far from the final answer, and many flaws in the theory are yet to be resolved. Thousands of phycisists worldwide are searching for ways to extend the Standard Model or to discover new physics that can illuminate the missing pieces in our understanding. The latest high-energy experiment designed to seek these answers is the Large Hadron Collider situated at the border of Switzerland and France. Using data from ATLAS, one of the four main detectors at the LHC, this thesis searches for a particular type of particles called R-hadrons predicted by Supersymmetry.

The author's contribution to ATLAS

The work presented in chapter 7 has contributed to the 2012 ATLAS search for heavy long-lived sleptons and R-hadrons using the 2011 ATLAS data set. This includes the calibration of reconstructed time-of-flight measurements in the calorimeters, calculation and combination of particle speed measurements (β) and the final error correction on β measurements from both the calorimeters and the MDT and RPC technologies in the muon system.

A guide to reading this thesis

The thesis is divided into four main parts. Part one lends itself to a review of the current experimental status of particle physics and theories beyond the current knowledge, with an emphasis on Supersymmetry. The second part gives an overview of the hardware in the ATLAS detector and the experimental conditions in the LHC. In part three an in-depth treatment is given of the development of quantities used for the discrimination of particles, and finally part four lists the obtained results of the performed search for gluino-based R-hadrons.

The basic goal of the search is to be able to discriminate R-hadrons (signal) from all Standard Model processes (background) as efficiently as possible. The highest discriminatory power is achieved by discarding as much background as possible, while still identifying a large fraction of signal events, i.e. having a high signal efficiency. An essential part of any search for new physics is therefore to estimate in which processes the new particles are theorised to be produced, what their properties are and how they will interact with the detector material, all of which is treated in chapters 2 and 3. Considering this knowledge, it is then possible to estimate the applicability of various measurements and variables to the signal/background discrimination. An example of the development and refinement of such a discriminator is given in chapter 7 describing the methods used to obtain a measurement of a particle's speed and its associated error using the ATLAS calorimeters. The entire selection process is outlined in chapter 8. Once the data has been reduced to that small subset consisting of tracks being candidates for new physics, the probability that a new discovery has been made can be estimated within the framework of statistical analysis. In the case that nothing new is found, a limit can be set on the production cross section of the particles as described in chapter 11. Finally, an outlook is given on the possibility of future improvements of the analysis in chapter 14.

Part I

Theory

1 The Standard Model of Particle Physics

Since the mid 20th century the Standard Model has been the foundation of modern particle physics. It is attributable to no single person or group and is a beautiful example of the power of a global collaborative effort. The first steps were taken in the 1960's with the development of a theoretical framework for combining the electromagnetic and weak interactions, the so-called electroweak theory, which in its modern form also incorporates the Higgs mechanism giving masses to the fermions and gauge bosons. The third and final fundamental force described by the Standard Model, the strong force, reached its modern form in the 1970's with the aid of experimental evidence showing that hadrons consist of quarks.

1.1 Particles in the Standard Model

The Standard Model comprises 12 gauge bosons, 12 leptons and 12 quarks in total, if the anti-particles are counted. These are described by properties such as their mass and spin as well as the charges they carry. Many of them are closely related, differing by only a few quantum numbers such as the electron and positron having opposite electric charge, thereby in that case being the antiparticles of each other. Several other relations can be drawn between the particles thus simplifying their presentation. The framework contains two main types of particles, fermions and bosons, which will be described in the following. Please refer to table 1.1 for a complete list of particles.

1.1.1 Fermions

Fermions are spin-$\frac{1}{2}$ particles obeying the Pauli exclusion principle, and consequently they are described energy-wise by Fermi-Dirac statistics. These properties give rise to the structure seen in the periodic table of the elements, and fermions are suitably called matter particles altough only af few of them form the building blocks of atoms. A distinction is made between fermions subject to the strong force called quarks and those that do not feel the strong force called leptons.

Leptons can have both electromagnetic and weak charge and therefore interact through these two forces. The electron is an example of a lepton having unit electrical charge $-e$, which is the lowest EM charge of any known freely observable particle subject to

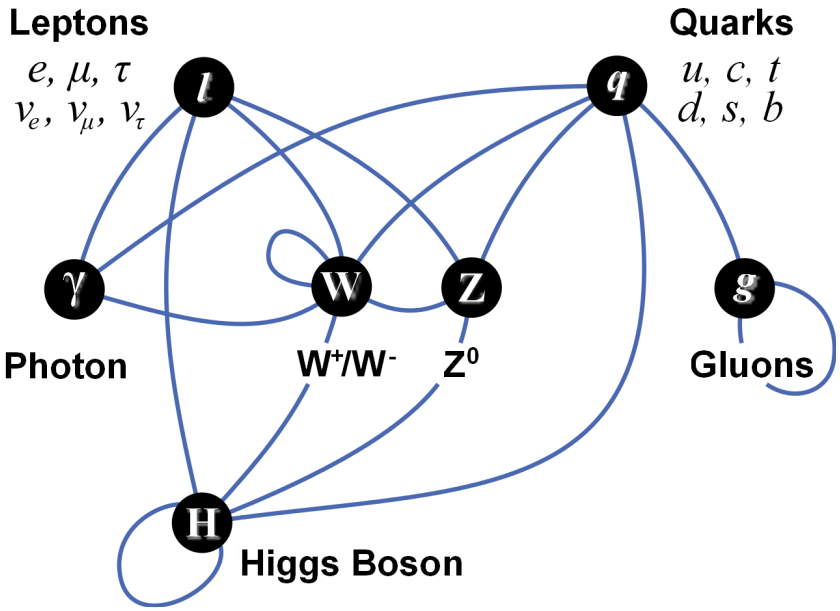

Figure 1.1: All possible interactions between particles in the Standard Model [14].

electromagnetism. Closely related to the electron are the muon (μ) and the tau (τ) lepton. These can be thought of as heavier copies of the electron. Each of these has an associated neutrino denoted ν_e, ν_μ and ν_τ respectively. These interact only through the weak force and can only be inferred in collider experiments through the observation of missing transverse energy (see section 5.1). Neutrino physics has developed rapidly in later years with the discovery of neutrino oscillations in 1998 [20] indicating that neutrinos have nonzero and different masses. At present only upper mass limits are known.

Quarks can interact through all three forces in the Standard Model. As a consequence of color confinement the quarks are never observed individually but are bound together in pairs (mesons) or triplets (baryons). Bound states of more than three quarks are theoretically possible and are a subject of continuing study [21]. All known quarks carry a fractional electric charge, but all observed bound states have their quark contents arranged in such a way that the sum of charges is the unit charge e. The two lightest quarks are the u and d quarks, also called up and down, which are the constituents of hadrons such as protons and neutrons. Together with the electron they form all the chemical elements, but only a small fraction of its total mass. As an example the proton has a mass far exceeding the sum of the masses of its three constituent quarks (1 u, 2 d). Its mass of 938.272046 MeV [1] is mostly due to the binding energy in the gluon field between the quarks (see section 1.1.2).

All the known fermions can be arranged in three so-called generations with each generation containing two quarks and two leptons. There is evidence that there may not be more than three generations of particles in the universe. At the Large Electron-Positron Collider the number of light neutrino generations has been estimated [18] to be 2.9840 ± 0.0082 in agreement with the known three generations. A massive neutrino could however constitute part of a fourth generation, and the search for fourth-generation particles is ongoing, see e.g. [19].

1.1.2 Bosons

The gauge bosons give rise to (at least) three of the four known fundamental forces of nature, these being the electromagnetic, weak and strong forces. Despite many attempts, particle phycisists have so far been unable to describe gravity within the framework of Quantum Field Theory. The force carriers are all spin-1 bosons and each of the fundamental forces is mediated by at least one such gauge boson.

Electromagnetism is the only force to have just one gauge boson associated. The photon, γ, is however quite versatile in its observable phenomena ranging from electricity and magnetism to the spectrum of electromagnetic radiation. Although the photon is responsible for binding matter together at the scale of atoms and molecules it also has infinite range due to its having no mass. The prerequisite for interaction with the photon is electric charge shared by all fermions except the neutrinos.

The weak interaction is often called the weak nuclear force as a reference to its key role in nuclear β-decays. It is mediated by three gauge bosons called the W^+, W^- and Z^0 particles. They are themselves massive and thus have an extremely short range of approximately 0.1 fm. Weak isospin determines whether a matter particle can interact through the weak force. Only particles with nonzero weak isospin undergo weak interactions, which is the case only for left-handed fermions. As the W bosons have electric charge they couple to the photon, and the weak force carriers also have self-couplings.

The strong interaction is responsible for binding together the quarks forming mesons and hadrons including the nucleons of atoms. The associated gauge bosons are the gluons, g, of which eight exist. The charge analogous to the electric charge of electromagnetism is called color charge. 'Color' can take three values called red, green and blue with each gluon having two colors or a superposition of these pairs associated with it. In contrast the quarks are only charged with one color which is altered during the interchange of gluons. Only particles with color charge interact via the strong force making it exclusive to quarks and the gluons themselves. Gluons are massless and have infinite range. However, the effective range of the interaction is only approximately 0.8 fm, which is the natural radius of a nucleon. This is due to the nature of the strong force. The strength of the interaction decreases at smaller distances, or equivalently higher energies, such that quarks can be considered free particles at sufficiently high energies. This concept is called asymptotic freedom. At larger distances the interaction strength does not decrease as opposed to electromagnetism, and extrapolating this behaviour the gluon field reaches a point where it has enough energy to produce new particles. All observed mesons and hadrons are color neutral.

The weaker binding force that holds together the nucleons to form nuclei also has its origin in the strong force but in a residual form. The particles mediating this residual strong force are virtual mesons which carry gluons with them. This force is felt by nucleons at distances of up to $1 - 3$ fm.

Particle	Abbreviation	Spin	EM charge [e]	Weak charge (Isospin, T_3)	Color charge	Mass [MeV]
electron	e	1/2	-1	$-1/2$	0	0.511
electron neutrino	ν_e	1/2	0	$+1/2$	0	$< 2.2 \cdot 10^{-6}$
muon	μ	1/2	-1	$-1/2$	0	105.7
muon neutrino	ν_μ	1/2	0	$+1/2$	0	< 0.170
tau	τ	1/2	-1	$-1/2$	0	1777
tau neutrino	ν_τ	1/2	0	$+1/2$	0	< 15.5
up	u	1/2	$+2/3$	$+1/2$	R, G, B	1.7-3.1
down	d	1/2	$-1/3$	$-1/2$	R, G, B	4.1-5.7
charm	c	1/2	$+2/3$	$+1/2$	R, G, B	1.18-1.34
strange	s	1/2	$-1/3$	$-1/2$	R, G, B	80-130
top	t	1/2	$+2/3$	$+1/2$	R, G, B	$173 \cdot 10^3$
bottom	b	1/2	$-1/3$	$-1/2$	R, G, B	$\sim 4.2 \cdot 10^3$
photon	γ	1	0	0	0	0
Z boson	Z^0	1	0	0	0	$91.188 \cdot 10^3$
W boson	$W^\pm$	1	± 1	± 1	0	$80.4 \cdot 10^3$
gluon	g	1	0	0	Color pair	0
Higgs boson	H^0	0	0	1/2	0	$\sim 125 \cdot 10^3$

Table 1.1: The properties of the particles in the Standard Model. Data has been taken from the Particle Data Group [1]. For the Higgs mass see section 1.1.3.

1.1.3 The Higgs boson

The Standard Model is still incomplete in the form described in the above sections, since there is no way to introduce mass terms for the particles if the gauge invariance of the electroweak force is to be preserved. To remedy this problem a new field was hypothesised in the 1960's. The Higgs field has a nonzero vacuum expectation value which leads to spontaneous breaking of electroweak symmetry. By coupling to the Higgs field the particles can acquire mass.

At the time of writing it is vey likely that the quantum associated with the Higgs field, the scalar Higgs boson, has been discovered. On the 4th of July 2012 the ATLAS and CMS experiments announced that a particle with properties consistent with the Standard Model Higgs boson had been discovered (see [22] and [23]). The mass quoted in table 1.1 is the approximate mass at which the new particle was discovered.

1.2 The theoretical foundation of the Standard Model

The Standard Model of particle physics is formulated within the theoretical framework known as Quantum Field Theory (QFT). This section will give a brief introduction to the concepts and principles behind the current theories of nature as they are written in the language of QFT. It is however in no way an attempt to give a fully satisfactory mathematical description which could fill many theses in itself.

1.2.1 Dynamics in a field theory

Taking a starting point in classical field theory all the dynamical information of a system can be contained within a quantity called the action. Given a system with Lagrangian L, the action S of the system is given by

$$S = \int L \mathrm{d}t = \int \mathcal{L}(\phi, \partial_\mu \phi) \mathrm{d}^4 x, \tag{1.2.1}$$

where $\mathcal{L}$ is called the Lagrangian density, but is commonly simply referred to as the Lagrangian, which will also be the convention in the following. The Lagrangian is a function of the fields and their derivatives, which are again functions of both time and spatial coordinates. Requiring that the action is stationary, that is $\delta S = 0$, will lead to the equations of motion for that particular system. This is called the principle of least action and leads to the Euler-Lagrange equations of motion for a classical system:

$$\partial_\mu \left(\frac{\partial \mathcal{L}}{\partial(\partial_\mu \phi)} \right) - \frac{\partial \mathcal{L}}{\partial \phi} = 0. \tag{1.2.2}$$

In Quantum Field Theory the generalisation of this canonical formulation is the *path integral* [47] originally developed by Richard Feynman. According to the path integral formulation the transition amplitude between two states $|\phi\rangle$ and $|\phi'\rangle$ can be written as

$$\langle \phi' | \phi \rangle = \int \mathcal{D}\phi \; e^{iS[\phi]}, \tag{1.2.3}$$

where $\mathcal{D}\phi$ denotes the sum over all possible 'paths' or configurations, and S is again the action of the system. The path integral generalizes the action principle of classical mechanics and does away with the notion of a single, unique path followed by the system. Instead the transition amplitude is a functional integral over a potentially infinite number of paths. Through the use of perturbation theory we can then recover the Feynman rules and diagrams for the desired process. An interesting property of the path integral is that the contributions from the various paths cancel in such a way that at lowest order only the classical analog remains. Higher order perturbations then give the quantum fluctuations/corrections. In quantum calculations this is referred to as LO (leading order), NLO (next to leading order) etc.

1.2.2 Symmetries

One of the most fundamental concepts in modern physics is that of symmetries. Here a symmetry should be understood in the sense that if a system is symmetric under a given transformation of variables, then the observable physical properties of the system will be identical before and after the transformation. Specifically in the case of a classical field theory the equations of motion will be invariant. The utility of studying the symmetries of a theory comes from Noether's theorem [6] which links a given symmetry to a conserved current. In this manner it is possible to discover conserved quantities that might otherwise not be immediately obvious.

Standard Model symmetries

In the Standard Model one finds a plethora of symmetries with various characteristics. One such group of symmetries is the Poincaré group in Minkowski spacetime. The Lagrangian of a system must be invariant under these transformations describing coordinate translations, rotations and so-called boosts transforming the system from one relativistic frame of reference to another. The corresponding conserved quantities include linear momentum, angular momentum and energy. The Poincaré symmetries are examples of global symmetries that are independent of the coordinates. They are also continuous since the possible values of the variables are not discretised in any way.

The Standard Model also contains a discrete symmetry constructed from the concepts of time reversal ($t \to -t$), charge conjugation (charge changes sign, $c \to -c$) and parity inversion (all spatial coordinates are flipped, $q_i \to -q_i$). None of these transformations are symmetries by themselves, and experimental evidence has shown that the weak interaction is not CP-invariant [48]. Thus only the joint operation CPT is considered a true symmetry in all parts of the Standard Model.

The kind of symmetries furthest removed from classical intuition are local gauge symmetries that are dependent on the position in space-time. Such symmetries give rise to all the gauge bosons responsible for the fundamental forces. The full set of gauge symmetries in the Standard Model can be formulated in group theory and can be written as $SU(3) \times SU(2) \times U(1)$, with $SU(3)$ describing the symmetry associated with the strong force and the gauge group $SU(2) \times U(1)$ being the foundation of the electroweak interaction.

Electromagnetism was the first force to be described by Quantum Field Theory, and its formulation is perhaps also the easiest to convey. The goal is to rectify the $U(1)$ symmetry by introducing a new term in the Lagrangian for a fermion in free space

$$\mathcal{L} = \bar{\psi}(x)(i\partial\!\!\!/ - m)\psi(x), \tag{1.2.4}$$

where ψ ($\bar{\psi}$) is the wave function of a fermion (anti-fermion) and $\partial\!\!\!/$ is a contraction of the sum $\gamma^\mu \partial_\mu$ with μ running over both time and space. γ^μ are the gamma matrices defined through the Pauli spin matrices σ^i as

$$\gamma^0 = \begin{pmatrix} 0 & \mathbb{1} \\ \mathbb{1} & 0 \end{pmatrix}, \quad \gamma^i = \begin{pmatrix} 0 & \sigma^i \\ -\sigma^i & 0 \end{pmatrix}, \tag{1.2.5}$$

where $\mathbb{1}$ is the 2×2 unit matrix. It can be seen that a $U(1)$ transformation, corresponding to a simple phase rotation of the wave function

$$\psi(x) \to e^{-i\alpha(x)}\psi(x), \quad \bar{\psi}(x) \to \bar{\psi}(x)e^{i\alpha(x)} \tag{1.2.6}$$

leaves the mass term $m\bar{\psi}\psi$ invariant, while the derivative term $i\bar{\psi}\partial\!\!\!/\psi$ changes. This can be counteracted by introducing a new field $A_\mu(x)$ transforming as

$$A_\mu(x) \to A_\mu(x) - \frac{1}{e}\partial_\mu \alpha(x). \tag{1.2.7}$$

The field is usually introduced into the Lagrangian by defining a covariant derivative given as $D_\mu = \partial_\mu + ieA_\mu(x)$. The further addition of a propagation term $F_{\mu\nu}F^{\mu\nu}$ with $F_{\mu\nu} = \partial_\mu A_\nu - \partial_\nu A_\mu$ then gives the final Lagrangian of Quantum Electro Dynamics:

$$\mathcal{L}_{\text{QED}} = \bar{\psi}(x)(i\not{D} - m)\psi(x) - \frac{1}{4}F_{\mu\nu}F^{\mu\nu}. \tag{1.2.8}$$

The newly introduced field A_μ is identified as the photon, and the propagation term $F_{\mu\nu}F^{\mu\nu}$ is equivalent to the Maxwell equations. To conclude, it is possible to derive the QED Lagrangian from the simple demand that it be invariant under $U(1)$ gauge transformations. The same basic idea is used in the derivation of both the strong and weak forces.

1.3 Unanswered questions in the Standard Model

Although the Standard Model is an extremely powerful predictive framework which is yet to be proven incorrect by experimental evidence, perhaps with the exception of neutrino masses, there are theoretical considerations that make it improbable that it is the final answer in the search for the laws governing particle physics. This problem goes much deeper than just the glaring absence of gravity in the theory. Many aspects of the framework have been constructed using what could be called a pragmatic approach. Elements such as the number of particles and generations as well as the scale of the particle masses were not implemented based on any deep philosophical insights, but to describe the observed data phenomenologically, which they do with impressive accuracy. Many fundamental questions are still left unanswered, a few of which will be discussed briefly in the following.

1.3.1 The relative size of particle masses

The masses of the fermions are parameters of the theory which are not known a priori and need to be added by hand from experimental data. Furthermore, the observed hierarchy of masses between the individual particles and between the three generations has not been explained. Such a model based on fundamental principles has long been sought within the physics community.

As mentioned in section 1.1.1 even the neutrinos seem to have mass. They were previously thought to exist only in their left-handed state making it impossible to add a renormalizable mass term [6, p. 713-715].

1.3.2 The Hierarchy problem

What has been dubbed the Hierarchy problem regards the issue of the observed scale of the particle masses. The spontaneous symmetry breaking caused by the Higgs field that generates the particle masses is problematic since the mass values are much lower than the Planck scale $m_p = \sqrt{\hbar c/G} = 10^{19}$ GeV. This is 17 orders of magnitude larger than the observed electroweak mass scale of the W and Z bosons at $\sim 10^2$ GeV. Due to very large quantum corrections stemming mainly from virtual top quarks the bare Higgs mass (the mass at infinitesimal distances) needs to be within a very narrow range to cancel these

quantum corrections almost precisely. This is necessary to explain why the electroweak scale is so low. This is an example of a 'fine-tuning' problem.

1.3.3 Unification of the forces

Due to renormalization the coupling constants of the three fundamental forces vary with the energy scale. If one plots the coupling strengths as a function of energy as seen in figure 2.2, the coupling strengths seem to coalesce into one unified force at very high energies of $\sim 10^{16}$ GeV. This has led to several Grand Unified Theories (GUTs) postulating that at energies above this GUT scale the three Standard Model symmetries are replaced by one simple symmetry.

Within the Standard Model the strengths of the forces do not meet at exactly the same point. One way to make this happen is by introducing another symmetry which sets fermions and bosons on equal footing. This is called Supersymmetry and will be the focus of the next chapter.

2 Supersymmetry and R-hadrons

Supersymmetry (SUSY) is one of many proposed theories 'beyond the Standard Model'. A common denominator of many of these theories is the concept of unification where the laws of nature simplify as the energy scale at which they are described increases. This strategy is well-founded in past theoretical successes that combined apparently separate phenomena into a common framework and explained how they could arise from the same underlying principle. This goes all the way back to Newton's description of the movement of both celestial and earthly objects [25]. History has seen several more such paradigm shifts with Maxwell's unification of electric and magnetic forces into the classical theory of electromagnetism, Einstein's insights relating mass, energy, space and time, and more recently the development of the electroweak theory.

2.1 Motivation for introducing supersymmetry

The fundamental assumption of supersymmetry is simple. The dichotomy between fermionic and bosonic fields described by the Standard Model is removed by postulating that all particles exist as pairs of fermions and bosons. For every known spin-1/2 matter particle a boson exists as its 'mirror image', and the reverse will be true for the known bosons. These are called the superpartners of the Standard Model particles and will have the same quantum numbers as their SM counterparts except for their spin. The commonly accepted naming scheme for SUSY particles is to add an *s* in front of the name in case it is the superpartner of a fermion, while the superpartner of a boson gets $-ino$ suffixed to its name. Accordingly, quarks and leptons are accompanied by bosonic squarks and sleptons while e.g. the gluons have gluinos as their fermionic counterparts.

The concept again reflects the idea of unification with the ultimate goal of uniting all four fundamental forces into a proto-force, i.e. also including quantum gravity supposedly mediated by spin-2 bosons. Supersymmetry is especially important for this purpose since only the inclusion of supersymmetry allows the description of both spin-1 and spin-2 gauge fields within the same algebra [24].

Field Content of the MSSM					
Super-Multiplets	Boson Fields	Fermionic Partners	SU(3)	SU(2)	U(1)
gluon/gluino	g	$\widetilde{g}$	8	1	0
gauge/	$W^{\pm}$, W^0	$\widetilde{W}^{\pm}$, $\widetilde{W}^0$	1	3	0
gaugino	B	$\widetilde{B}$	1	1	0
slepton/	$(\widetilde{\nu}, \widetilde{e}^-)_L$	$(\nu, e^-)_L$	1	2	-1
lepton	$\widetilde{e}^-_R$	e^-_R	1	1	-2
squark/	$(\widetilde{u}_L, \widetilde{d}_L)$	$(u, d)_L$	3	2	1/3
quark	$\widetilde{u}_R$	u_R	3	1	4/3
	$\widetilde{d}_R$	d_R	3	1	-2/3
Higgs/	(H^0_d, H^-_d)	$(\widetilde{H}^0_d, \widetilde{H}^-_d)$	1	2	-1
higgsino	(H^+_u, H^0_u)	$(\widetilde{H}^+_u, \widetilde{H}^0_u)$	1	2	1

Table 2.1: The field content of the MSSM [1, p. 1293]. The superpartners are denoted by a tilde.

A special feature of the supersymmetric algebra realized through its fermionic generators is the fact that the spin of a state can be changed by 1/2 such that a bosonic (fermionic) state can be transformed into a fermionic (bosonic) state [27, p. 88]:

$$Q\,|\text{fermion}\rangle = |\text{boson}\rangle$$
$$Q\,|\text{boson}\rangle = |\text{fermion}\rangle\,.$$

This means that starting with the spin-2 graviton state it is possible to act repeatedly by SUSY generators, Q, to obtain the full spectrum of spin states

$$2 \to 3/2 \to 1 \to 1/2 \to 0.$$

Another noteworthy property of supersymmetry is the promise of cancellation of ultraviolet divergencies which is a possible solution to the Hierarchy problem in GUTs (see section 1.3.2). Furthermore it is straightforward to construct a generalization of the Standard Model that includes SUSY [24]. It even leads to predictions at the TeV scale which can be tested. An assortment of the possible supersymmetric particles are listed in figure 2.4 along with the current lower mass limits from the ATLAS experiment. For more information on ATLAS see chapter 5.

2.2 Predictions of supersymmetry

The simplest SUSY model is an extension of the Standard Model called the Minimal Supersymmetric Standard Model (MSSM) which introduces the least amount of additional fields. For a list of particles in the MSSM see table 2.1. A problem for any supersymmetric model is the lack of evidence for the existence of the predicted particles. If SUSY were an

Name	Particle content	Charges
R-gluinoball	$\tilde{g}g$	R^0
R-meson	$\tilde{g}q\bar{q}$ or $\tilde{q}\bar{q}$	R^+, R^-, R^0
R-baryon	$\tilde{g}qqq$ or $\tilde{q}qq$	R^{++}, R^+, R^-, R^0

Table 2.2: General composition of gluino-based R-hadrons. For a comprehensive list of the possible quark content see [34].

exact symmetry the predicted particles would have the same mass as their SM counterparts. This is clearly not the case as it would have lead to their discovery long ago. To correct this shortcoming it is common to introduce a mechanism that breaks the symmetry below a certain SUSY breaking scale. This can be done in such a way that the SUSY particles belong to a mass scale much higher than that of the SM particles. If SUSY should be able to alleviate the quandary of fine tuning due to virtual corrections, this mass scale has an upper limit at the order of ~ 1 TeV [28]. Ergo it should be possible to confirm or refute SUSY at the current generation of colliders with the Large Hadron Collider at the forefront.

2.2.1 Stable Massive Particles

When contemplating the possibilities for the existence and the properties of new particles (composite or fundamental) beyond the Standard Model, it is often instructive to look at the properties of the known particles *in* the Standard Model. Although electrons are heavier than e.g. neutrinos, they are prohibited from decaying into them due to the conservation of electric charge. The proton, which is of course a composite particle, owes its stability to other conserved quantum numbers; baryon and lepton number. Another useful example is the neutron. The only possible decay channel is β decay, $n \rightarrow p^+ + e^- + \bar{\nu}_e$, involving an intermediate weak gauge boson in the form of a W^-, which gives it a fairly long lifetime in free space. When bound in hadronic matter on the other hand, it can be extremely stable. Drawing inspiration from the considerations above, one is able to theorise about the existence of new particles and states having many of the same characteristics as the particles already observed, and this can be a tentative guideline when planning a new search strategy.

Many extensions to the Standard Model contain predictions of new exotic particles that can be directly detected in collider experiments. This implies that they should leave a sufficiently strong signal in the detector material through electromagnetic or strong interactions. Such states should be relatively heavy, since they have not yet been detected, and have a sufficiently long lifetime to traverse the detector before decaying. This has led to the common designation of the name Stable Massive Particle (SMP) to states with these properties.

2.2.2 R-parity

One way to construct stable supersymmetric states is to postulate a new conserved quantity with mutually exclusive values assigned to SM and SUSY particles respectively. One such possible quantum number is R-parity defined as [31]:

$$R = (-1)^{3B+L+2S} \tag{2.2.1}$$

with B being the baryon number, L the lepton number and S the spin of the particle. Plugging in the values of these three numbers for the known particles, it is seen that SM particles will have $R = +1$ while SUSY particles will have $R = -1$. This naturally leads to at least one new stable particle since the Lightest Supersymmetric Particle (LSP) has no available phase space for decay if R-parity is conserved. The LSP could be one of four neutralinos predicted by many models as electrically neutral particles with couplings at the strength of the weak interaction. A neutralino could therefore be a candidate for dark matter due to its feeble interaction strength combined with a considerable mass making it non-relativistic as opposed to neutrinos. Unfortunately, such a particle would not be directly detectable but could be inferred through conservation of momentum.

In the most general SUSY models the accidental symmetries that lead to baryon and lepton conservation in the Standard Model are no longer upheld. R-parity is again useful since it defines an explicit symmetry of a combination of B and L. Without R-parity or similar symmetries the proton would not be protected from decay, which contradicts results from experiments such as the Super-Kamiokande setting limits on the proton lifetime of $> 10^{33}$ years [32].

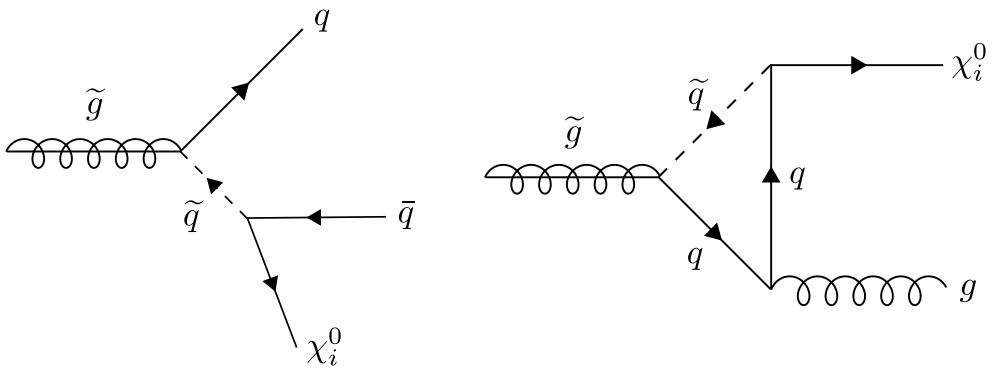

Figure 2.1: Gluino decay. Left: tree-level diagram of gluino decay into two quarks and a neutralino. Right: 1-loop diagram of gluino decay into a gluon and a neutralino.

2.2.3 Split Supersymmetry

A specific way to construct a theory containing SMP candidates beyond the LSP is to assume that there is more than one mass scale associated with the SUSY particles. In a scenario called Split Supersymmetry the masses of the particles are divided into a low scale at experimentally available weak scale energies to which the higgsinos and gaugeinos belong, and a much higher inaccessible scale encompassing all the scalars such as the squarks, except the ordinary Higgs. Since gluinos can only decay through squarks their decay is highly suppressed due to the high squark masses in this model, making them candidates for SMPs. The available decay modes are three-body decays into two quarks and a chargino or neutralino

$$\tilde{g} \to \tilde{q}q \to q\bar{q}(q') + \chi_i^0(\chi_i^{\pm}) \tag{2.2.2}$$

or two-body decays into a gluon and a neutralino

$$\tilde{g} \to g + \chi_i^0 \tag{2.2.3}$$

as illustrated in figure 2.1. The gluino lifetime $\tau_{\tilde{g}}$ depends on both the gluino mass $m_{\tilde{g}}$ and the mass scale of the sfermions, $\tilde{m}$. An approximate formula for this dependence can written as [33]:

$$\tau_{\tilde{g}} = \frac{4\text{ s}}{N} \times \left(\frac{\tilde{m}}{10^9\text{ GeV}}\right)^4 \times \left(\frac{1\text{ TeV}}{m_{\tilde{g}}}\right). \tag{2.2.4}$$

According to the values of $m_{\tilde{g}}$ and $\tilde{m}$ it is possible that the available decay modes are sufficiently slow for the gluino to be categorized as an SMP. The gluino lifetime is illustrated in figure 2.3 at various parameter values. Consequently, the discovery of a long-lived gluino would not only be a very strong indication of Split Supersymmetry, it would also be an opportunity to measure the scale of the sfermion masses.

2.3 R-hadrons

As described in section 1.1.2 particles subject to the strong force will always arrange themselves in color-neutral configurations. Gluinos and squarks are no exception and one could imagine bound states of gluinos (R-gluinoballs), in analogy to their SM counterparts, or gluinos and squarks that bind themselves to SM quarks to form so-called R-hadrons, which will be the focus of the rest of this thesis. Gluinos are fermionic color-octets (C_8) while squarks are color-triplets (C_3) and hadronise into bound states consisting of the supersymmetric particle and a differing number of quarks called the Light Quark System (LQS). A summary of the types of possible bound states is given in table 2.2. A comprehensive list of the possible quark combinations in R-hadrons can be found in [34].

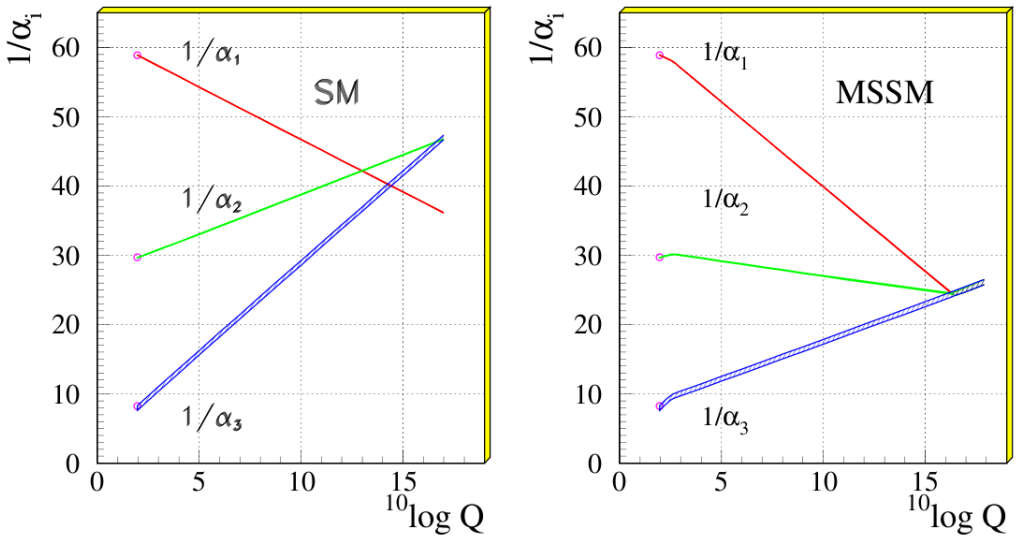

Figure 2.2: The evolution of the inverse coupling constants in the Standard Model (left) and in the minimal supersymmetric extension to the Standard Model, MSSM (right). Unification of all three forces is seen to happen only with the inclusion of SUSY. The α_i represent, in numerically ascending order, the EM, weak and strong coupling constants [24].

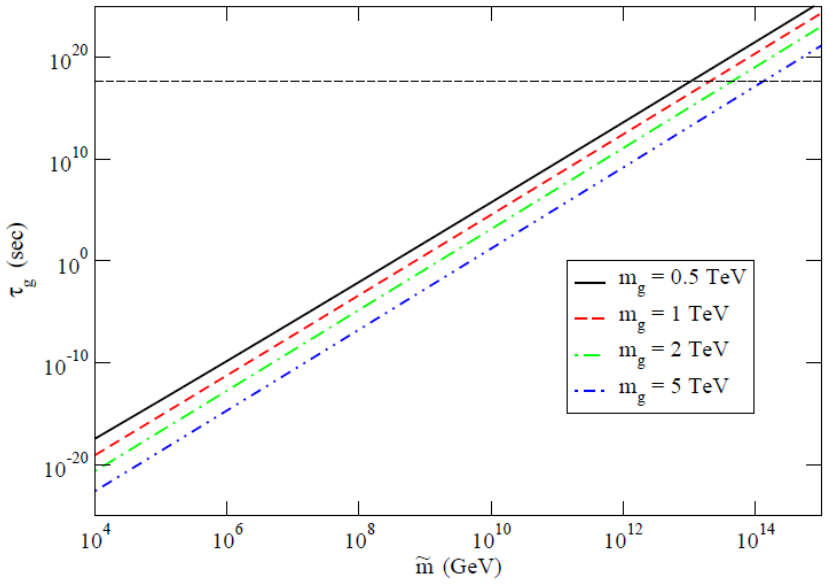

Figure 2.3: The gluino lifetime in Split Supersymmetry as a function of the sfermion mass scale at various values of the gluino mass according to equation 2.2.4 [33].

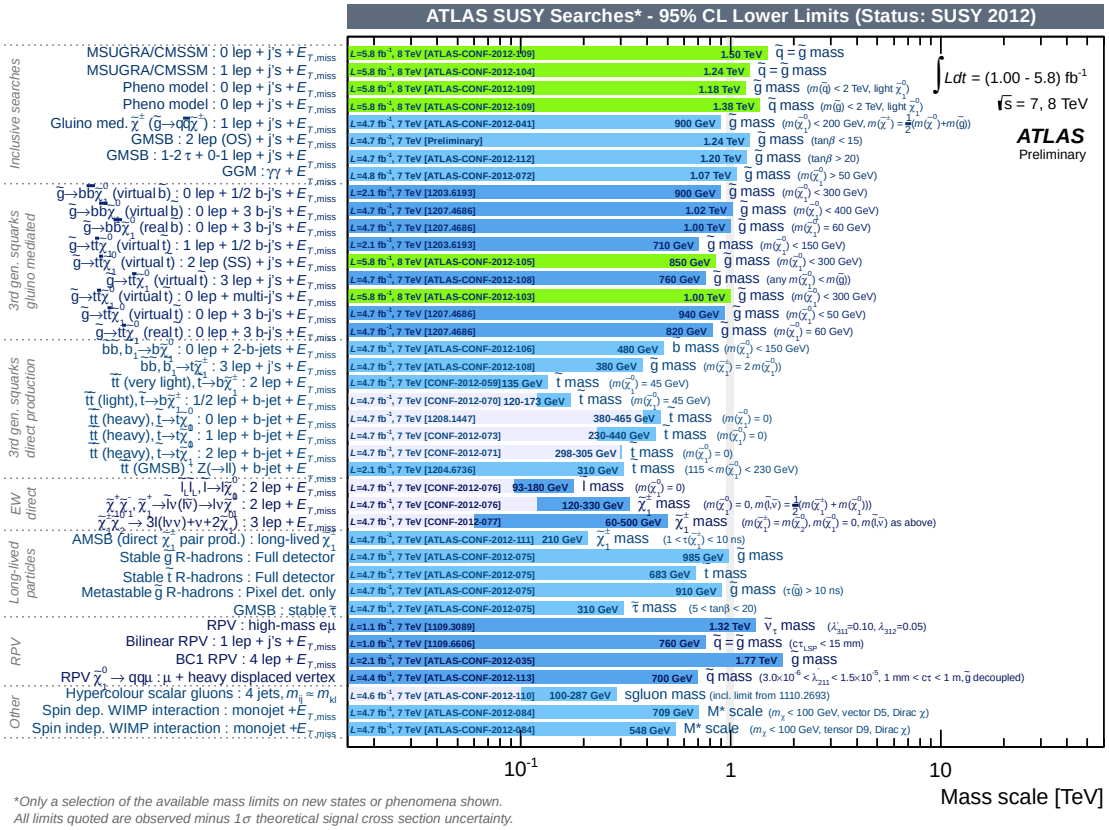

Figure 2.4: A representative selection of the 2012 mass limits on supersymmetric particles found through analysis of data from the ATLAS detector under various theoretical assumptions [26]. The official mass limit on gluino-based R-hadrons is seen to be 985 GeV (see also figure 11.2).

3 R-hadron production and detection

The LHC enables phycisists to search for SMPs, including R-hadrons, with masses well into the TeV range. If they exist at this mass scale, they will be produced in acceptable amounts for searches based on statistical methods.

3.1 Production mechanisms

The production of SMPs at colliders is usually attributed to pair production [28]:

$$p_1 + p_2 \rightarrow X_1 + X_2, \tag{3.1.1}$$

where p_1 and p_2 are some constituents of the colliding beam particles, while X_1 and X_2 are new particles belonging to the same new theory. Single particle production $p_1 + p_2 \rightarrow X$ is also possible, but this would imply that the inverse reaction could also take place, which corresponds to the decay $X \rightarrow p_1 p_2$. Since the decay width is proportional to the production rate, the most abundantly produced single SMPs would also be the shortest-lived.

The direct production rate of colored SMPs (color triplets) is proportional to the strong coupling constant of $O(\alpha_s^2)$, while that of color singlets, i.e. leptonic SMPs, is of $O(\alpha_{\text{ew}}^2)$. The production rate of SMPs with color charge is thus a factor $(\alpha_{\text{ew}}/\alpha_s)^2$ larger due to this effect alone. A further relative reduction in the direct production of leptonic SMPs comes from the fact that they cannot couple directly to the gluon field in the colliding particles. A Pythia simulation predicting the pair production cross section of exotic fourth-generation quarks and leptons at the LHC is shown in figure 3.1. The cross section of the quarks clearly dominates. High rates of leptonic SMP production can instead be sought in the decays of heavier particles with color charge.

Many possible scenarios exist in which the produced particles are stable enough to pass through and interact with the detector material. If the SMP contains the LSP of the theory and R-parity is conserved, or if the SMP is a gluino-based R-hadron and Split Supersymmetry is assumed, then the SMPs can be considered stable at distances compared to the size of the detector.

In the case of gluino production the leading-order parton interactions are [30]

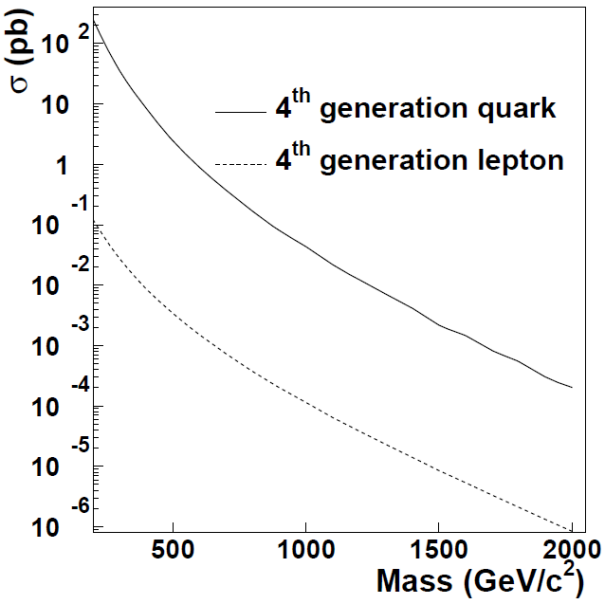

Figure 3.1: A Pythia simulation predicting the pair production cross section of 4th generation quarks and leptons at the LHC [28].

$$g + g \rightarrow \tilde{g} + \tilde{g} \tag{3.1.2}$$

$$q_i + \bar{q}_i \rightarrow \tilde{g} + \tilde{g} \tag{3.1.3}$$

$$q_i + g \rightarrow \tilde{q}_i + \tilde{g} \text{ (and c.c.)} \tag{3.1.4}$$

where the subscript i indicates the quark flavor and 'c.c.' is charge conjugation. A range of Feynman diagrams for the above interactions are given in figure 3.3.

3.2 Energy loss in matter

Electrically charged particles traversing material such as a particle detector will have a characteristic energy loss due to excitation or ionization of the atoms in the material by energy transfer from the incident particle to the electrons of the atoms. The amount of energy loss is not easily described by a single formula over the range of all possible incident particle momenta, but for relevant momenta in the GeV range and low TeV range for heavy particles the Bethe formula (sometimes called Bethe-Bloch) is a good description of the mean rate of energy loss. To quantify what is meant by the 'rate of energy loss' a useful variable known as the *stopping power* can be defined as the mean energy loss per distance L traversed in a material weighted by the density ρ of the given material. Defining $x = L/\rho$ the Bethe formula describes the stopping power dE/dx for moderately relativistic particles:

$$-\frac{dE}{dx} = Kz^2\frac{Z}{A}\frac{1}{\beta^2}\left[\frac{1}{2}\ln\frac{2m_e c^2\beta^2\gamma^2 T_{\max}}{I^2} - \beta^2 - \frac{\delta(\beta\gamma)}{2}\right], \tag{3.2.1}$$

where $T_{\max}$ is the maximum energy that a free electron can obtain:

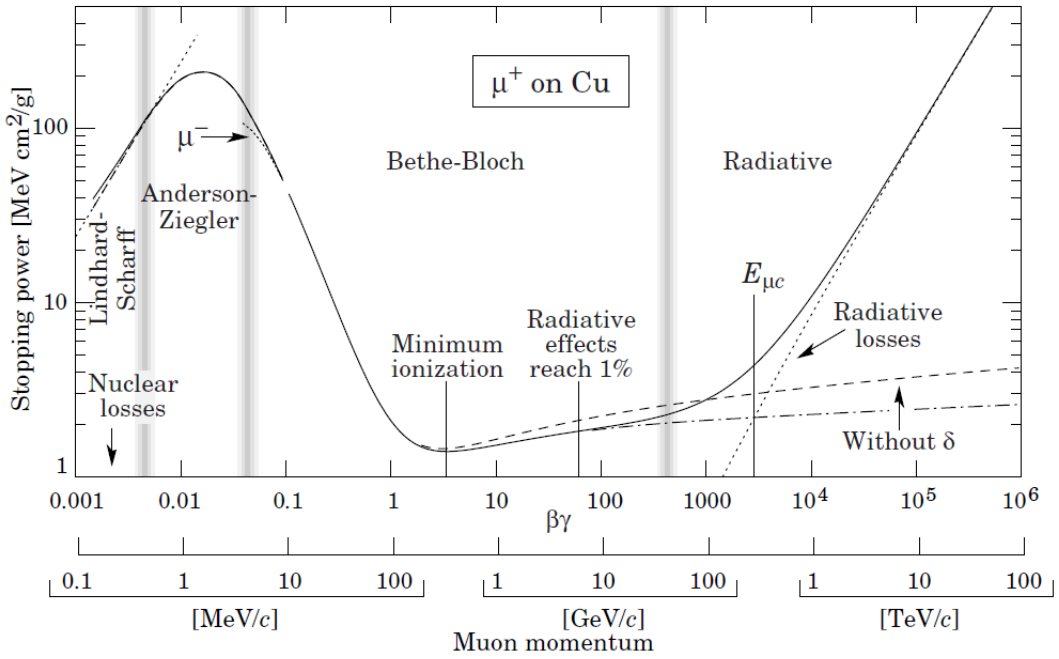

Figure 3.2: Stopping power of muons incident on copper for a wide $\beta\gamma$ range. Figure is taken from [28].

$$T_{\max} = \frac{2m_e c^2 \beta^2 \gamma^2}{1 + 2\gamma\frac{m_e}{M} + \frac{m_e}{M}^2}. \tag{3.2.2}$$

See table 3.1 for a description of the variables. The Bethe formula is an accurate description of the stopping power for a wide range of materials in the approximate interval $0.1 < \beta\gamma < 1000$. The Bethe curve for the example of muons on copper is illustrated in figure 3.2 as part of larger $\beta\gamma$ interval described by various other effects. Notice that the Bethe formula is independent of the mass of the incident particle since $\beta\gamma = p/m$. Instead plotting the stopping power as a function of momentum results in the dE/dx rise at low $\beta\gamma$ happening at different momenta characteristic to each type of particle (figure 3.4).

3.3 Matter interactions of R-hadrons

The gluino or squark is by far the heaviest constituent in the R-hadron and will have a highly localised wave function, while the LQS will be distributed over normal hadronic distances. The mass of an R-hadron is expected to follow the same formula as a lowest-excitation ordinary hadron [35]

$$m_{Had} \sim \sum_i m_i - k \sum_{i \neq j} \frac{(\mathbf{F}_i \cdot \mathbf{F}_j)(\mathbf{S}_i \cdot \mathbf{S}_j)}{m_i m_j}, \tag{3.3.1}$$

where m_i are the constituent masses, $\mathbf{F}_i$ are the color SU(3) matrices, $\mathbf{S}_i$ the spin SU(2) matrices and k a parameter giving the mass a dependence on how the wave function behaves at the origin. If several R-hadrons with different squark, gluino or LQS content

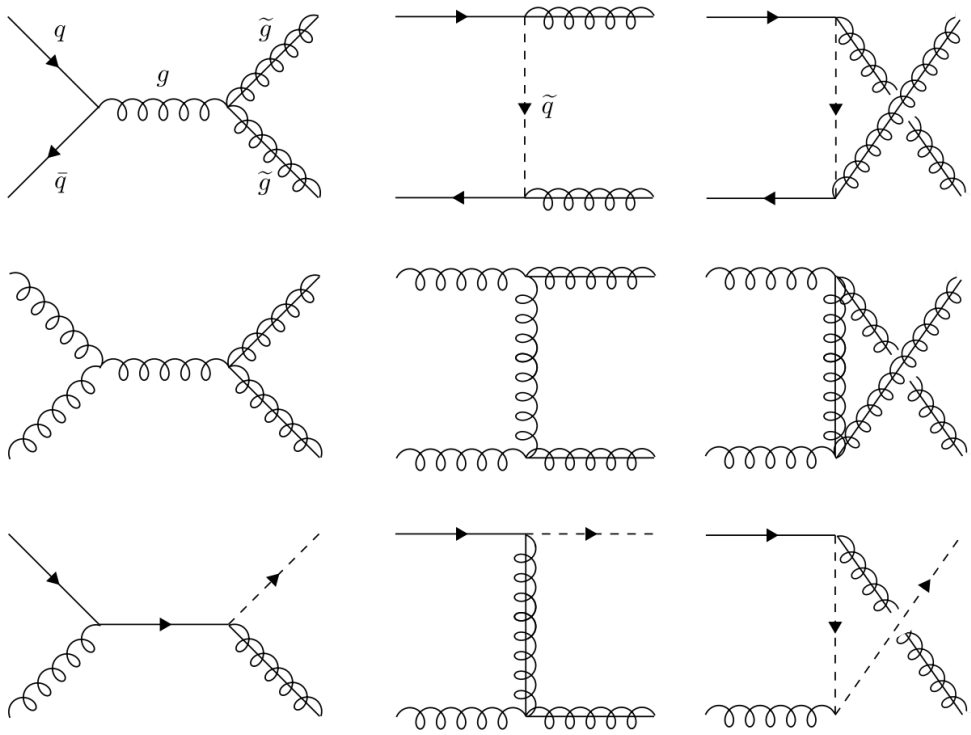

Figure 3.3: Feynman diagrams showing pair production of SUSY particles resulting in one or two gluinos in the final state.

exist, the lightest state would be expected to have the highest production rate in the detector. However, if this state is assumed to be neutral, only the less abundant, more massive states would be good candidates for a search.

Only the LQS is expected to participate in the majority of interactions with the detector material [28] due to the high mass of the gluino. A large fraction of the R-hadron momentum would therefore pass relatively unhindered through the detector, giving R-hadrons many of the same characteristics as muons. It is therefore expected that muons are the largest source of background in an R-hadron search.

An R-hadron could potentially interact strongly with the detector material resulting in an exchange of quarks in its LQS. A new combination of quarks has the potential to alter the electric charge of the R-hadron. With an LQS consisting of the known quarks having electric charges of $-1/3$ or $+2/3$, the possible combinations result in R-hadron charges of -1, 0, 1 or 2 in units of e. With the exception of initial or final states having zero charge, in which case tracking is not possible, all other transitions can be investigated.

The above considerations illuminate the fact that a search strategy is highly dependent on the R-hadron model. The present thesis will concentrate on a search for gluino-based R-hadrons with the described gluino production mechanisms. Interactions with the detector material are given by a generic interaction model described in [29], which is simulated in Geant4 [49].

Symbol	Definition	Units or Value
M	Incident particle mass	MeV/c^2
E	Incident part. energy γMc^2	MeV
T	Kinetic energy	MeV
$m_e c^2$	Electron mass $\times c^2$	0.510988918(44) MeV
ze	Charge of incident particle	
Z	Atomic number of absorber	
A	Atomic mass of absorber	g mol^{-1}
K/A	$4\pi N_A r_e^2 m_e c^2/A$	0.307075 MeV g^{-1} cm^2 for $A = 1$ g mol^{-1}
I	Mean excitation energy	eV
$\delta(\beta\gamma)$	Density effect correction to ionization energy loss	
N_e	Electron density	(units of r_e)$^{-3}$

Table 3.1: Variables used in the Bethe formula (a subset of the values in the table found in [1]).

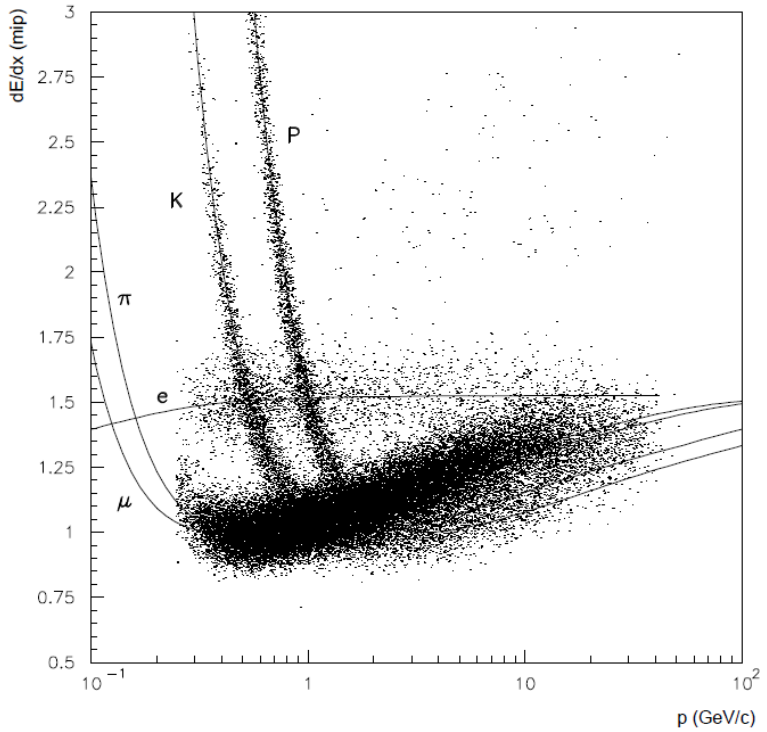

Figure 3.4: Stopping power for various particles as a function on momentum given in units of MIPs. Notice the position of the low-momentum dE/dx rise characteristic to each particle type. Figure is taken from [38].

Part II

The experiment

4 Collider physics at the LHC

In 1994 the construction of the world's current highest-energy particle accelerator was approved by the council of The European Organization for Nuclear Research (CERN) [3, p. 1]. The machine was named the Large Hadron Collider (LHC) due to its function as a proton-proton collider. Installation was done in the existing 27 km circular tunnel at the border between Switzerland and France in which the Large Electron-Positron Collider (LEP) was operated until 2000.

The LHC is a high energy, high luminosity accelerator designed to reach an energy of 7 TeV per proton per beam, giving a center-of-mass collision energy of 14 TeV, at an instantaneous luminosity of 10^{34} $\mathrm{cm}^{-2}\mathrm{s}^{-1}$. Alternatively, lead ions can be accelerated to an energy of 1.38 TeV per nucleon to study heavy ion collisions. At the time of writing, however, the nominal collision energy has not yet been attained. A setback happened in 2008 due to an electrical fault, which resulted in a quenching incident of about 100 bending magnets causing mechanical damage and release of helium [5]. Consequently, the first proton-proton runs at $\sqrt{s} = 900$ GeV used for physics analysis were not completed until the end of 2009. The 2011 data set was collected at $\sqrt{s} = 7$ TeV and is the basis for the work in this thesis.

4.1 Why a hadron collider?

The choice of a hadron collider as the next big CERN endeavour should be seen in the context of the state of particle physics in general. When the LHC was commissioned the main goals of the physics community were to either complete the Standard Model picture by discovering the Higgs boson or perhaps extend knowledge beyond the Standard Model by finding evidence for theories such as supersymmetry, technicolor or extra dimensions. Colliding hadrons is ideal for this purpose due to the wide range of energies accessible at the same operating parameters of the machine and at the same center-of-mass energy (See section 4.4). This makes hadron colliders able to scan a large phase space and a wide interval of particle masses. Hadron colliders are often called 'discovery machines' for this reason. The disadvantage is the chaotic conditions of the collisions generating a large amount of background, which sets high demands on the granularity and time resolution of the detectors and lowers the possible precision of the measurements.

Had the basic particles already been discovered, precision measurements would be the preferred choice. This is the goal of electron-positron colliders such as CERN's Compact Linear Collider (CLIC) or the proposed International Linear Collider (ILC). Using leptons

(elementary particles) provides a very clean environment to perform precision measurements at a narrow energy range. Hence prior knowledge is needed of the energies at which the new particles are produced.

4.2 The journey to near-light speed

The LHC storage ring is the final destination in a long line of steps needed to produce the protons and accelerate them from rest. These include previous CERN flagships, now demoted to serve LHC with high-energy protons and ions. Some of these machines were built in the mid 1900's and have been operated by several generations of phycisits. Since no single accelerator can operate at at all energies up to the full design energy of the LHC, the re-use of older existing accelerators is a cost-effective way to feed particles into the LHC.

The protons are extracted by ionizing stored hydrogen and are subsequently injected into the Alvarez Proton Linac, also called Linac 2, a linear accelerator operational since 1978 capable of accelerating the protons to 50 MeV (See figure 4.1). The protons are already travelling at roughly 30% of the speed of light ($0.3c$). The next stop on the protons' itinerary is the Proton Synchrotron Booster raising the energy to 1.4 GeV ($0.9c$). The oldest of the accelerators, the Proton Synchrotron (PS) from 1959 followed by the Super Proton Synchrotron (SPS) then take over to further raise the energy to 25 GeV (0.999c) and 450 GeV (0.99997c) respectively. At these energies relativity clearly comes into play keeping the particles at almost the same speed, while the energy is increased more than an order of magnitude. Once the protons have been accelerated by the SPS and having already travelled more than 6 million kilometers in the process, they are ready to be injected into the LHC storage ring. Here they are accelerated to their final energy and collided at the detectors placed around the ring, of which the the four main experiments are ALICE, ATLAS, CMS, and LHCb.

4.3 Numbers and concepts

The accelerator tunnel has eight straight sections and eight arcs designed for LEP's eight crossing points and long straight sections with RF cavities to compensate for energy losses due to synchrotron radiation. These are not necessary for the LHC since protons radiate considerably less than electrons, meaning that the optimal configuration would have had longer arcs. The internal diameter of 3.7 meters of the underground tunnel made it necessary to design the proton rings with a twin-bore magnet system instead of two completely separate proton rings. To reach proton beam energies of 7 TeV a magnetic field of 8.33 T is needed for the main dipole magnets. This high field strength is achieved by using superconducting magnets cooled to temperatures below 2 K using superfluid helium.

4.3.1 Luminosity

An indispensible concept at particle accelerators is that of luminosity. The (instantaneous) luminosity of a particle beam is defined as the relation between the number of observed

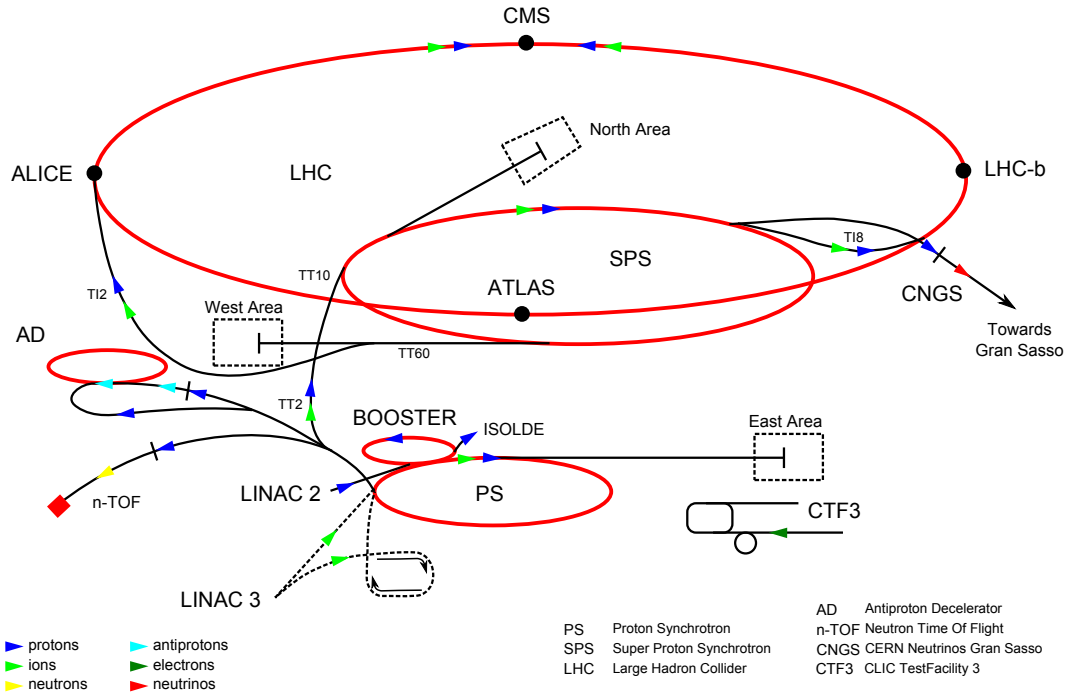

Figure 4.1: Drawing of the the CERN accelerator complex [13] including the various machines used to prepare protons for injection into the LHC.

events of a given type per unit time and the cross section for that type of event:

$$N = \mathcal{L}\sigma \tag{4.3.1}$$

Given that a particle beam has been circulating for some time interval T with a time-dependent luminosity $\mathcal{L}(t)$, the integrated luminosity during that time interval is then

$$L = \int_0^T \mathcal{L} dt \tag{4.3.2}$$

The luminosity in a collider can be calculated as

$$L = \frac{N_b^2 n_b f_{\text{rev}} \gamma}{4\pi \varepsilon_n \beta^*}. \tag{4.3.3}$$

The variables used in the calculation are the number of particles per bunch N_b, the number of bunches per beam n_b, the frequency of revolution f_{rev}, the number of bunches k, the relativistic gamma factor γ, the emittance of the beam in the transverse direction ε_n and the beta function at the collision point β^*. This value should be scaled by a geometric factor depending on the crossing angle between the beams. Figure 4.2 shows the efficiency of the ATLAS data collection in 2011.

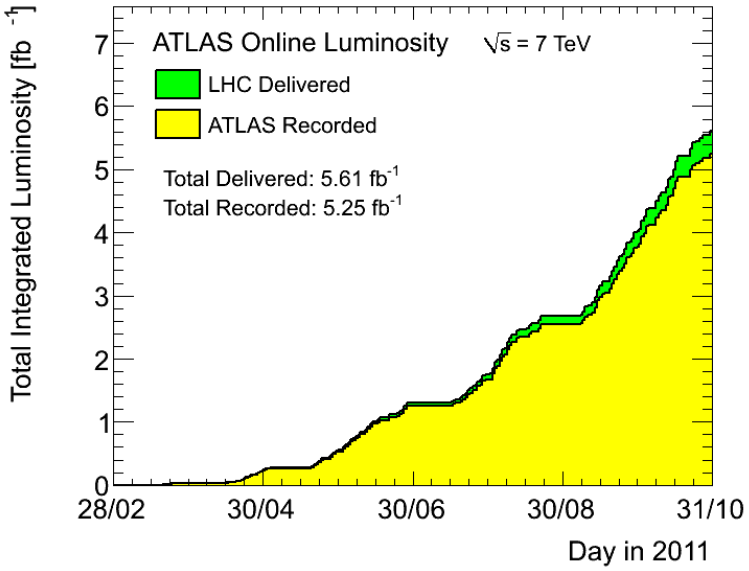

Figure 4.2: The amount of integrated luminosity collected by ATLAS as a function of date compared to the total luminosity delivered by the LHC.

4.4 Parton distribution functions

The non-elementary nature of hadrons complicates the theory of their interactions. The individual partons inside the protons in a collider beam can in principle have momentum in all three spatial directions, but the extremely high momentum in the beam direction and the effort to collimate the beam makes the perpendicular momentum components negligible, and they will not be treated in the following.

In a collision between two protons it is possible for one or more partons from each proton to interact with each other. The interacting partons can be valence quarks, virtual sea quarks or gluons. Two energy scales are usually identified as the *soft* scale at energies below or comparable to the binding energy of the proton, and the *hard* scale at considerably higher energies, where the partons can be considered free particles during their interaction. The present analysis is focused on the hard interactions, which are assumed to be the only kind of interaction involving the required amount of energy to produce R-hadrons. In case the hard process produces a colored particle, it may emit a gluon as final state radiation (FSR), or one of the interacting partons may emit a gluon before the hard interaction, which is called initial state radiation (ISR). Gluons with sufficient energy can change the topology of the event in the detector by producing jets. These arise in a subsequent process where the gluons undergo parton showering, creating a swarm of quarks and gluons, and finally hadronize into a jet of colorless particles.

If the partons participating in the interaction are denoted i and j, then the fraction of the hadron momentum P_{hadron} carried by each of them can be written as

$$x_{i,j} = \frac{P_{i,j}}{P_{\text{hadron}}}. \tag{4.4.1}$$

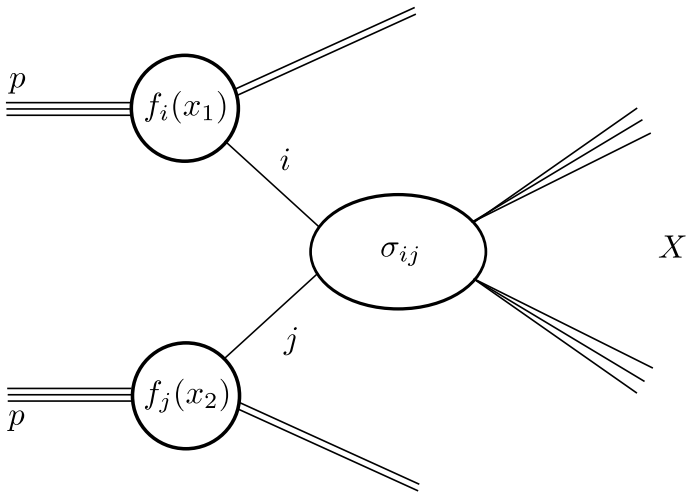

Figure 4.3: Illustration of a parton interaction in a proton-proton collision. The partons i, j have probability densities $f_{i,j}(x)$ to have a fraction x of the proton momentum, and the cross section of the hard interaction producing some final state X is $\sigma_{i,j}$.

This determines how much momentum/energy is available to the produced particles following the collision. The probability of a collision taking place involving partons with certain x-values is contained in the Parton Distribution Functions (PDFs) $f_i(x)$, where i is the particular parton involved. As the PDFs describe the proton binding mechanism in the non-perturbative QCD energy region, these cannot be calculated from first principle but must be obtained as experimental fits to large sets of data. Several groups are dedicated to obtaining these fits, among which the results of the Coordinated Theoretical-Experimental Project on QCD (CTEQ) are widely used. Another collaboration supplies the Martin-Stirling-Thorne-Watt Parton Distribution Functions (MSTW). The probability functions are dependent on the energy scale, also called the momentum transfer scale, involved in the interaction. This is the product of the energies of both partons, $Q^2 = x_i x_j s$. Since radiative processes become more prevalent at higher Q^2 the PDFs will be biased towards lower x-values when the energy scale increases. An illustration of a p-p collision with a single parton interaction is given in figure 4.3. Figure 4.4 shows the MSTW 2008 PDFs at two values of Q^2.

The PDFs are crucial elements in the theoretical calculations of particle production cross sections. According to the factorization theorem for deeply inelastic scattering [37] the total cross section is a combination of long and short distance contributions, with the PDFs taking the role of the long distance part. The hard process cross sections that are calculable from perturbative QCD constitute the short distance part. The factorized cross section can then be calculated as

$$\sigma_{pp\to X} = \sum_{ij} \int_0^1 \mathrm{d}x_1 \mathrm{d}x_2 f_i(x_1, \alpha_s(\mu_r), \mu_f^2) f_j(x_2, \alpha_s(\mu_r), \mu_f^2) \times \\ \times \hat{\sigma}_{ij\to X}(x_1, x_2, Q^2, \alpha_s(\mu_r), \mu_r^2, \mu_f^2), \tag{4.4.2}$$

where μ_r is the renormalization scale factor on which the running strong coupling constant

α is dependent, and μ_f is the factorization scale that describes the proton model. According to the value of μ_f the proton can either be approximated by the valence quark model or the more complicated picture where virtual sea quarks and gluons are also prevalent.

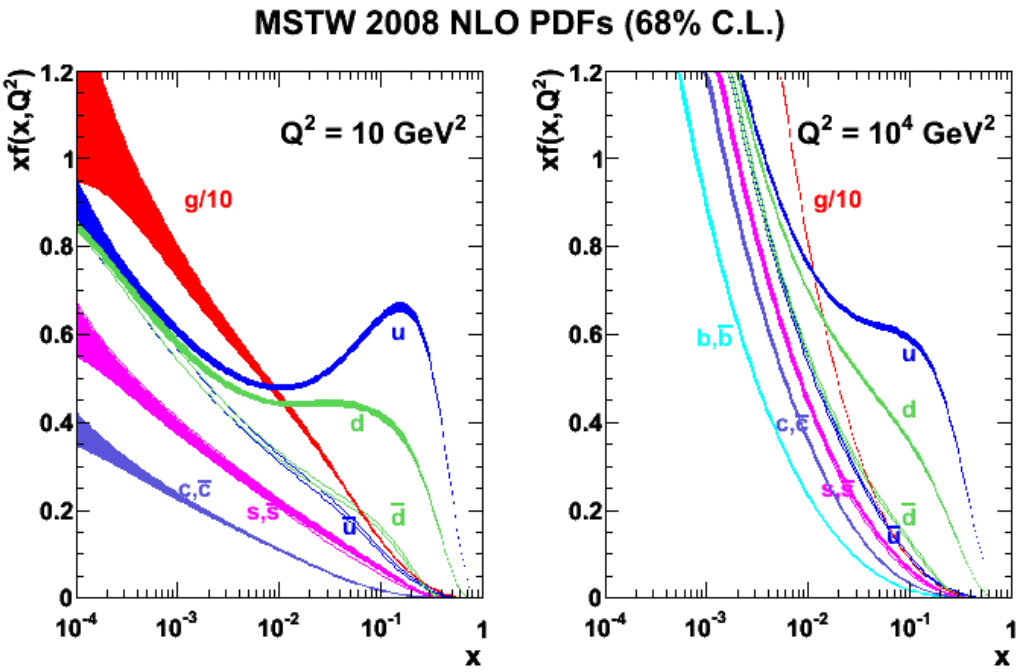

Figure 4.4: The MSTW 2008 Parton Distribution Functions [50] at a momentum transfer scale of $Q^2 = 10$ GeV^2 (left) and $Q^2 = 10^4$ GeV^2 (right). Both valence quark, sea (anti-)quark and gluon functions are shown.

5 The ATLAS detector

The ATLAS detector (A Toroidal LHC ApparatuS) is one of two general purpose detectors situated along the LHC ring, the second being CMS. Its main purpose is to investigate physics at the TeV scale utilising a high center-of-mass energy of up to 14 TeV, which the LHC has been designed to reach. This includes both the continuing effort to test the Standard Model at higher energies than ever before, as well as the search for new physics beyond the Standard Model.

Being a general purpose detector, ATLAS is designed to reconstruct all possible types of particle events stemming from pp collisions. This necessarily makes ATLAS a complex combination of many subdetectors, each with its own specialised purpose. The operating parameters of the LHC also impose constraints on the detector parts. The large production energies require a strong magnetic field of 2 Tesla in the Inner Detector (see section 5.2) to measure the momentum and charge of high $p_\perp$ particles. The high nominal luminosity of 10^{34} $\mathrm{cm}^{-2}\mathrm{s}^{-1}$ demands a high time resolution of the various detectors as well as fine-grained tracking due to overlapping events (pile-up). As the physically largest of the four main detectors at the LHC, ATLAS is 44 m long and 25 m high while weighing 7,000 tonnes. It is installed at Point 1 in the LHC ring, situated very close to CERN's Meyrin site.

An overview of the constituents of ATLAS is given in this chapter with focus on the parts most relevant for the analysis in the following chapters. Any information in this chapter without an explicit source reference originates from the ATLAS documentation [2].

5.1 Definition of coordinates and variables

The basis for all spatial calculations in ATLAS is a right-handed coordinate system with its origin placed at the nominal interaction point at the center of the detector. The z-axis is oriented in the direction of the beam pipe, while the positive x-axis is defined to point towards the center of the LHC ring, and the positive y-axis points upwards. Thus the xy-plane is orthogonal to the direction of the particle beams. Alternatively, a cylindrical coordinate system is used with azimuthal angle ϕ and preserving the above z-axis definition. The polar angle from the beam direction is denoted θ.

The initial momentum of the interacting partons along the z-direction is not known due to the nature of the collisions described in section 4.4. Only the transverse component is known; a very good approximation is that the initial transverse momentum is zero. This is not an exact statement since transverse fluctuations can also occur, but at such low scales

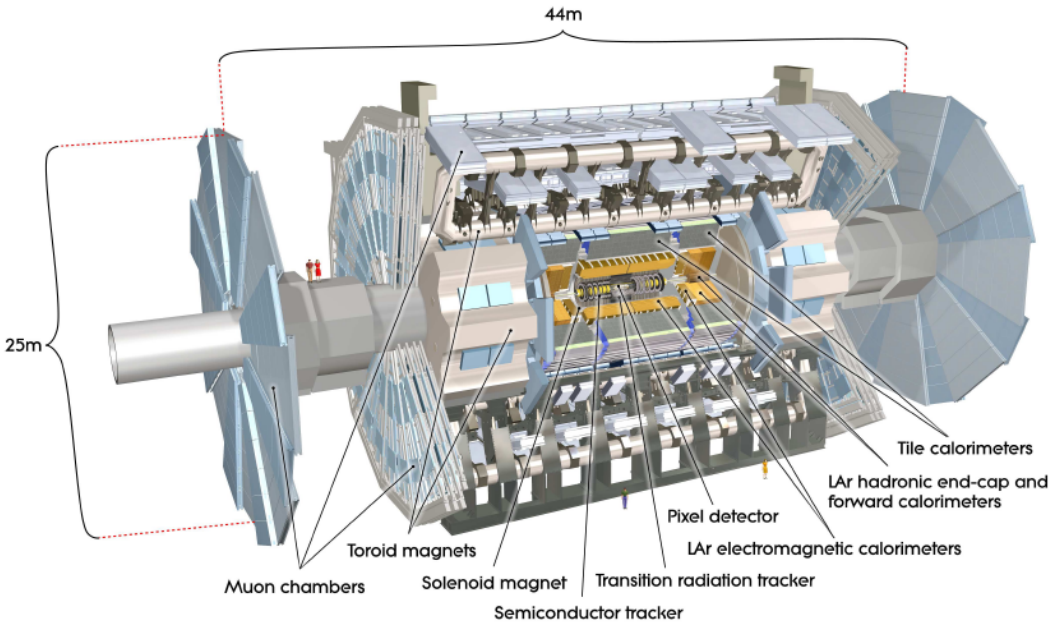

Figure 5.1: Full view of the ATLAS detector illustrating the placement of tracking systems, calorimetry, muon spectrometer and magnets.

that the above approximation is possible. The natural way to express quantities such as momentum and energy is thus by using their transverse component:

$$p_T = \sqrt{p_x^2 + p_y^2} = p\sin(\theta), \tag{5.1.1}$$

$$E_T = \sqrt{m^2 + p_T^2 \cosh \eta}. \tag{5.1.2}$$

Another important concept is that of missing transverse energy, E_T^{miss}. It refers to energy that is not detected but is necessary to uphold energy and momentum conservation in a collision. Particles such as neutrinos are not directly detected due to their feeble interaction strength, so the only practical way to infer their existence is by applying conservation laws and calculating the direction and amount of missing energy. The missing transverse energy is defined as

$$E_T^{\text{miss}} = -\sum_i (p_T)_i. \tag{5.1.3}$$

A widely used variable in particle physics is the rapidity $y = 1/2\ln[(E + p_z)/(E - p_z)]$. It relates different relativistic frames of reference by describing the hyperbolic angle associated with the Lorentz boost necessary to transition from one frame to the other. Its additive nature under such Lorentz boosts is in stark contrast to the complex rules of velocity addition. The polar angle θ can be substituted with the so-called pseudorapidity η defined as the low mass limit of rapidity: $\eta = \lim_{m\to 0} y$. This quantity is useful for highly relativistic particles where $\eta \sim y$ since the kinetic energy is dominating. The pseudorapidity can be written as

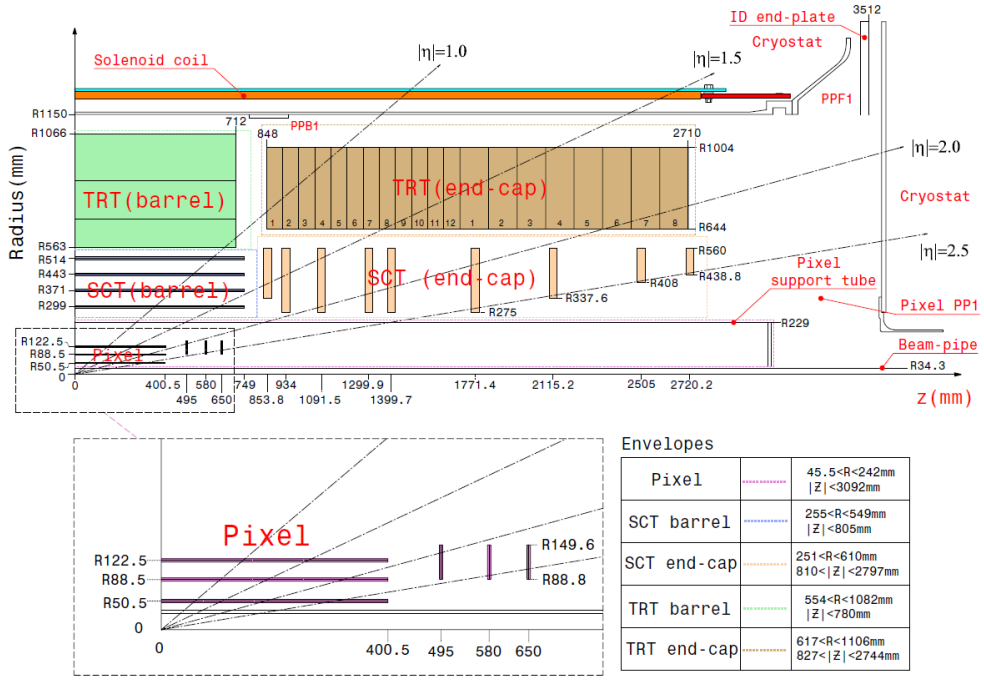

Figure 5.2: An illustration of one half of the Inner Detector showing the relative placement of the layers in the Pixel, SCT and TRT with respect to the beam pipe (radius) and central collision point (z-axis).

$$\eta = -\ln\left(\tan\frac{\theta}{2}\right). \tag{5.1.4}$$

In isolation studies and other analyses where it is important to know how close the produced particles are to each other when traversing the detector, the quantity ΔR is defined to describe the angle between the trajectories of any two particles. Considering the fact that on average the distribution of particles is uniform in both ϕ and η (for $|\eta|$ below a certain threshold depending on the collision energy, defining a 'rapidity plateau', and that the detector granularity reflects this, the angle (or isolation cone) is sensibly defined in the η–ϕ plane as

$$\Delta R = \sqrt{(\Delta\eta)^2 + (\Delta\phi)^2}. \tag{5.1.5}$$

5.2 The Inner Detector

The innermost part of ATLAS, the Inner Detector (ID), is designed to provide high precision tracking of electrically charged particles for $|\eta| < 2.5$ and enables the reconstruction of particle momenta, primary collision vertices as well as secondary vertices of short-lived particles. This is achieved by a combination of three distinct detection systems, each utilising different technologies. Placed closest to the beam pipe are two silicon based subsystems named the Pixel and SCT detectors providing pixel tracking and silicon strip detection. A detector based on straw tubes (TRT) is positioned as the third system, which provides both tracking and electron identification based on transition radiation detection at $|\eta| < 1.9$.

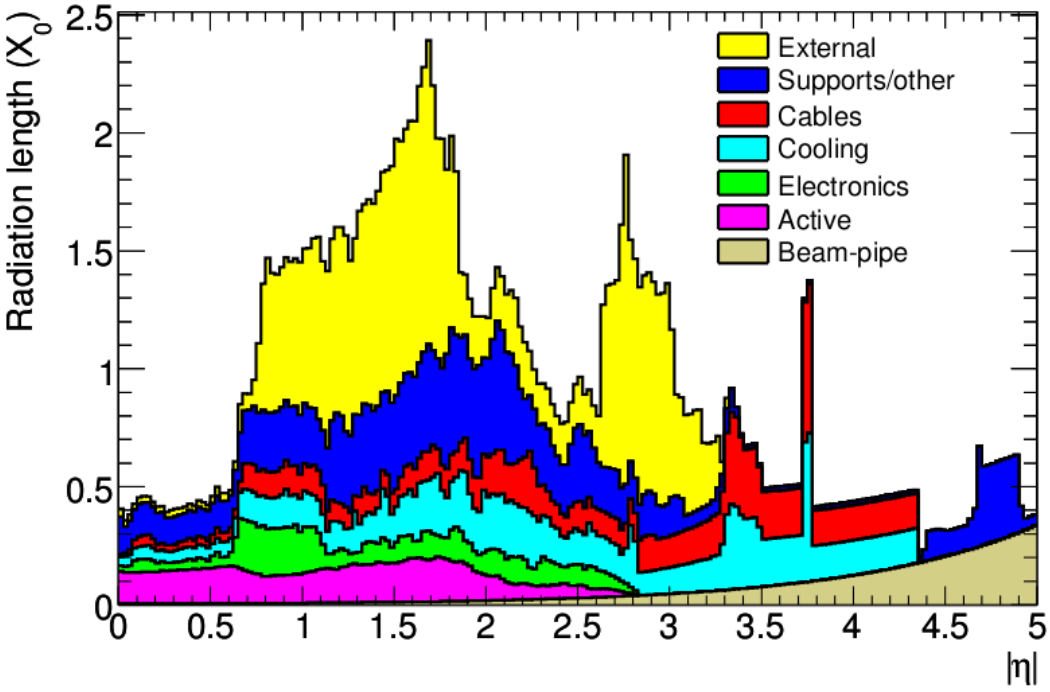

Figure 5.3: The material budget for various parts of the Inner Detector given in radiation lengths (X_0) as a function of $|\eta|$. The distribution has been averaged over ϕ. The central region (low $|\eta|$) is most sensitive to new physics, and the material budget is accordingly very low in this region.

As a tracking system, the Inner Detector is designed to minimise the interaction of the produced particles with the detector services and support structure to let particles reach the outer detector parts while losing as little energy as possible. The material budget is a trade-off between the desired low interaction rate and the need for a stable mechanical structure, readout electronics, cooling etc. The amount of material that particles must traverse is given in units of interaction lengths, which is the mean distance traversed by a high energy electron through the material before it only possesses $1/e$ of its initial energy. The ID material budget is displayed graphically in figure 5.3.

5.2.1 The Pixel Detector

The detector system positioned closest to the beam pipe is the Pixel detector. It consists of 1744 pixel modules, each having an active detection area of 63×19 mm^2, a thickness of 250 μm and each containing 46080 pixels. The modules are arranged in three layers parallel to the beam pipe at $0 < |\eta| < 1.7$ (barrel) complemented by three vertical disks on each side covering the interval $1.7 < |\eta| < 2.5$ (endcap). All three layers have identical tracking precision with each module having a spatial resolution of $10(R-\phi)$ $115(z)$ μm.

With its first layer positioned at a radius of just 50.5 mm from the beam pipe the Pixel detector is necessarily designed using highly radiation resilient materials. The proximity to the proton interactions makes the Pixel detector essential for reconstructing secondary vertices of short-lived particles, which is used extensively in e.g. b-physics.

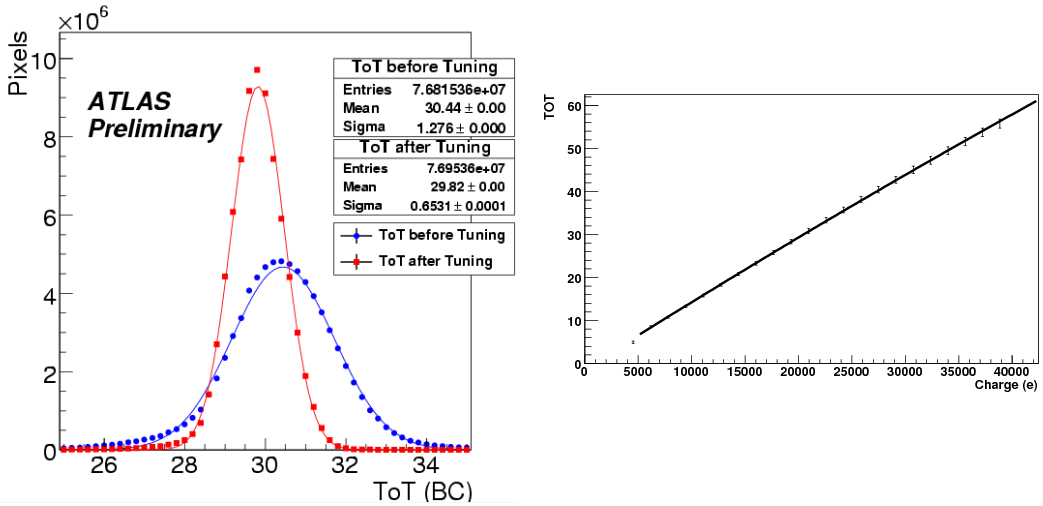

Figure 5.4: Left: Tuning of Pixel ToT using MIPs. Right: Relation between Time over Threshold and injected charge. A clear linear relationship after calibration is observed. Both plots taken from the Pixel Detector TWiki [17].

dE/dx measurement

For each triggered collision event a list of hits is provided by the Pixel detector. The discrimination between noise and signal in each pixel cell is done using a voltage threshold. The initial analog charge signal first needs to be amplified and is then compared to the discrimination threshold. The signal is subsequently digitised to contain the spatial coordinates of the hits as well as the Time over Threshold (ToT). Since the pixel cells have been calibrated to have a linear ToT response versus charge deposition (figure 5.4), the energy loss dE/dx of particles traversing the cell can be obtained. The response is tuned such that minimum ionising particles (MIPs) correspond to a specific ToT. In figure 5.4 a value of 30 bunch crossings at 25 ns spacing has been chosen.

It is possible to reconstruct $\beta\gamma$ of a particle from Pixel dE/dx measurements. The chosen procedure follows the method in [43], which uses a five parameter function to describe how the most probable value (MVP) of the particle energy loss depends on dE/dx:

$$MPV_{dE/dx}(\beta\gamma) = \frac{p_1}{\beta^{p_3}} \ln(1 + (|p_2|\beta\gamma)^{p_5}) - p_4. \tag{5.2.1}$$

5.2.2 The Semi-Conductor Tracker

The SCT resembles the Pixel detector in function and layout but relies on narrow silicon strips instead of pixels. The strips are combined in slightly rotated pairs on each module. The total number of 4088 modules are placed in four coaxial layers in the barrel region and 9 disk layers in each of the two endcaps. The modules covers an area of 63 m^2 which gives almost hermetic coverage with potential for a least four space-point measurements at all pseudorapidities $|\eta| < 2.5$. The spatial resolution for a module is 17 μm (R-ϕ) and 580 μm (z).

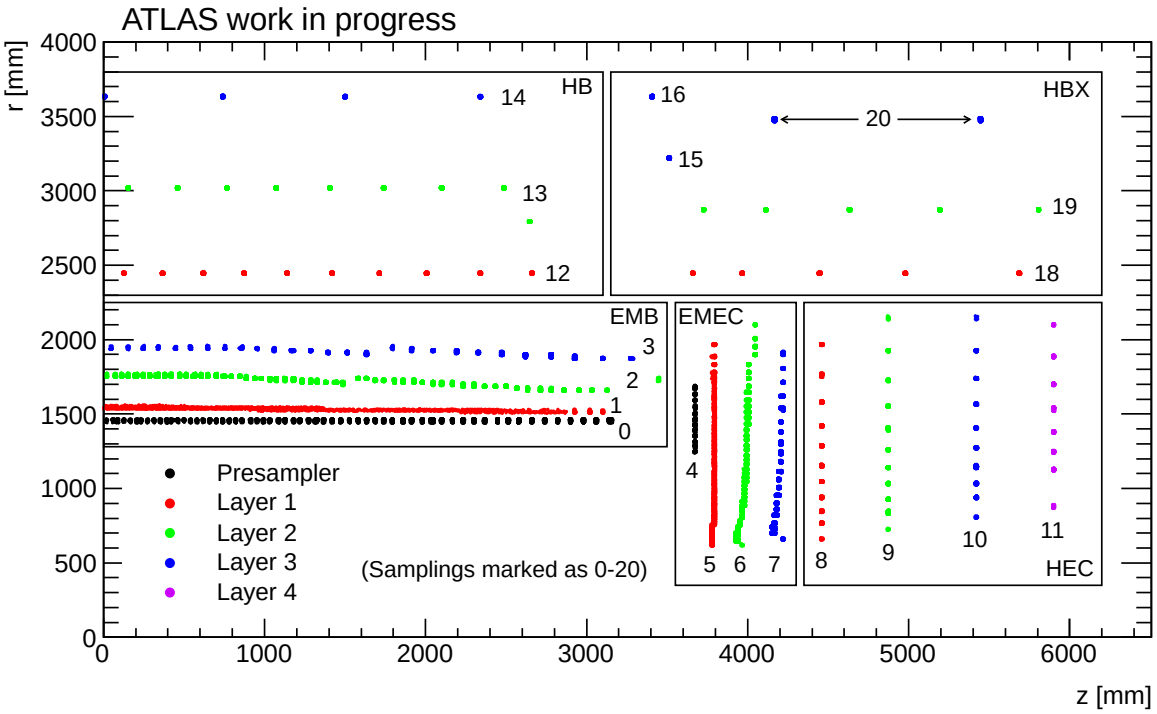

Figure 5.5: The (r, z) coordinates of the center of all cells in the ATLAS calorimeters. The divisions show cells belonging to the electromagnetic barrel (EMB), electromagnetic endcap (EMEC), hadronic barrel (HB), hadronic extended barrel (HBX) and hadronic endcap (HEC). These are again divided into layers (distinguished by color) and samplings (enumerated from 0 to 20). Sampling 17 has no attributed cells. Layers are the units on which timing calibration is performed (see chapter 7).

5.2.3 The Transition Radiation Tracker

The Transition Radiation Tracker (TRT) is built up of proportional chambers consisting of straws within a radiator material in such a way that the probability of transition radiation by relativistic particles is maximised. The emitted photons have a typical energy of a few keV, corresponding to X-rays. The TRT thus has finely developed particle identification (PID) capabilities for the purposes of discriminating e.g. pions from electrons. The straw resolution is 140 μm (R-ϕ), and the total number of hits per track averages at 35.

The straws are made of mylar coated kapton and have a radius of 2 mm. The cathode consists of a 0.2 μm aluminium layer in the form of a coating on the inside of the straws, while the central anode is a 31 μm wide tungsten wire with a gold coating. The medium in the straws consists of 70% Xe, 27% CO_2 and 3% O_2. The TRT amounts to a total number of 298,304 straws arranged in two endcaps, each with 122880 straws, and a barrel region with 52544 straws.

The readout is performed using two threshold values with the low threshold (LT) tuned for minimum ionising particles at 250 eV, while the high threshold (HT) triggers at ~6 keV for identification of transition radiation.

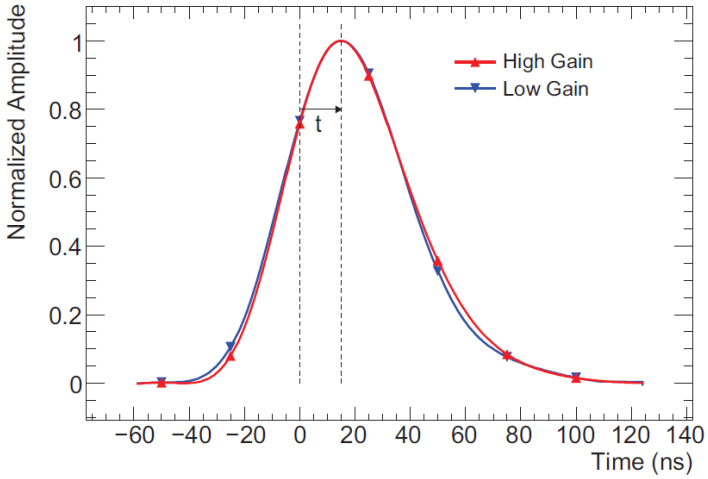

Figure 5.6: Example of a pulse shape fitted to the signal from a Tile calorimeter cell [4].

5.3 Calorimeters

Outside the Inner Detector the particles reach an electromagnetic and a hadronic calorimeter system. The pseudorapidity coverage of these calorimeters goes up to $|\eta| < 4.9$ if the forward calorimeter is included. The calorimeter parts used in the present analysis are the liquid argon (LAr) barrel and endcap and Tile calorimeters extending to $|\eta| < 3.2$. The region with Inner Detector tracking is fitted with a high-precision LAr electromagnetic calorimeter with a hermetic and fine grained accordion geometry with high energy precision. As a result, this region ($|\eta| < 2.5$) yields high precision measurements on photons, electrons and missing transverse energy.

The hadronic calorimeter is based on different technologies depending on the pseudorapidity. In the barrel region it is based on scintillating material interleaved with steel tiles as absorbant, earning it the name 'Tile calorimeter'. The endcap region is again LAr based. This technology has been chosen for its radiation hardness and linearity as well as the possibility of replacing the argon over time as it gets ionised.

Contrary to the tracking purposes of the Inner Detector, the calorimeters are designed to absorb the full energy of the particles. The combined depth should therefore correspond to a large number of radiation lengths. A detailed view of the geometric placement of all individual calorimeter cells and their division into layers can be seen in figure 5.5.

5.3.1 The Tile Calorimeter

The ATLAS Tile calorimeter (TileCal) is a cylindrical hadronic sampling calorimeter. It uses steel as the absorber material and plastic scintillators as the active layers. It covers radii from 2280 mm to 4230 mm while the η coverage extends to $|\eta| \lesssim 1.7$. The calorimeter is subdivided into a central barrel covering $|\eta| \lesssim 1.0$ and an extended barrel covering $0.8 \lesssim |\eta| \lesssim 1.7$. Both barrel parts are divided into 64 modules spaced evenly in azimuthal angle ϕ. The cells in each module are placed in three layers called A, BC and D layers in the central barrel and A, B and D layers in the extended barrel as illustrated in figure 5.7. In the following analysis each layer in the central and extended barrel are combined such that the Tile calorimeter is divided into three layers only.

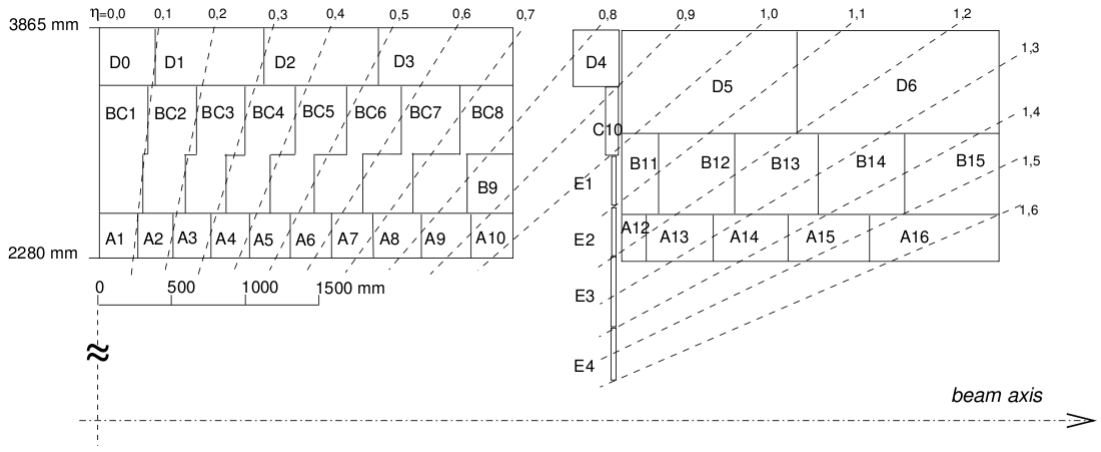

Figure 5.7: A schematic rendering of the individual cells in the three TileCal layers. The Barrel and Extended Barrel parts of the Tile calorimeter are combined into three layers.

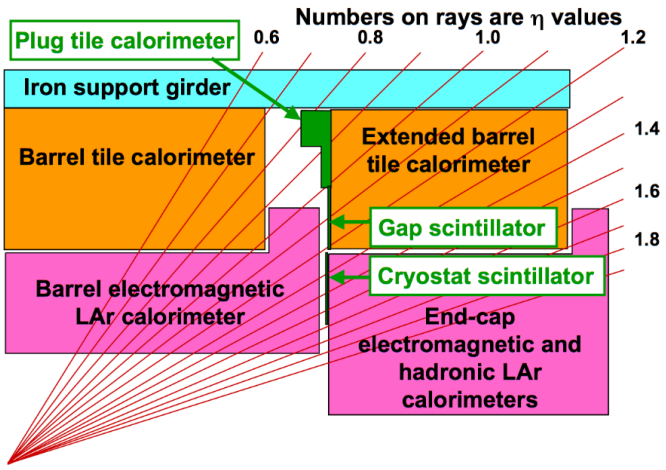

Figure 5.8: Overview of the Tile and LAr calorimeters and their η coverage.

Timing reconstruction in the Tile calorimeter is done by fitting a pulse shape to the digitally sampled signal when a hit in a cell is detected. The pulse shape is parameterised as [4]

$$f(t) = Ag(t_0 - t) + ped, \tag{5.3.1}$$

where A is the amplitude, g is the pulse shape function and ped is the pedestal value. See figure 5.6 for an illustration.

5.3.2 The LAr calorimeters

Liquid argon is used as the active detector medium in the electromagnetic barrel (EMB) and endcap (EMEC) calorimeters, as well as in the hadronic endcap (HEC). They are all sampling calorimeters, using lead plates for the EM calorimeters and copper plates for the

HEC calorimeter. The EM calorimeters consist of accordion-shaped absorber cells. This geometry provides complete ϕ coverage without azimuthal gaps.

The barrel EM calorimeter covers the region $0 < |\eta| < 1.475$ and consists of 4 layers. The EMEC calorimeter also consists of 4 layers and covers the region $1.375 < |\eta| < 3.2$. The 4 layers of the HEC calorimeter cover the range $1.5 < |\eta| < 3.2$.

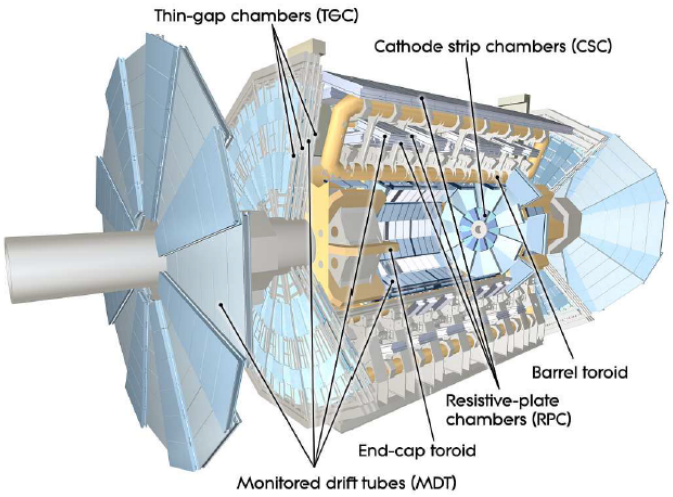

Figure 5.9: The positions of the various parts of the ATLAS muon system.

5.4 The Muon Spectrometer

The Muon Spectrometer (MS) is the outermost and hence the last part of ATLAS that particles can potentially meet on their trajectory. It is designed to detect charged particles that are able to penetrate the barrel and endcap calorimeters, and to measure their momentum for $|\eta| < 2.7$. The momentum measurement is enabled by large toroid magnets. Depending on the radius R and azimuthal angle ϕ the field strength has values from 0.15 T to 2.5 T. To give a sense of the momentum resolution achievable in the MS, a track with three MDT hits has a relative uncertainty of

$$\frac{\sigma_p}{p} = \frac{\Delta S \times p}{500\ \mu\text{m}}, \tag{5.4.1}$$

with an assumed sagitta resolution ΔS of 45 μm. This corresponds to a resolution of $\sim 10\%$ for a 1 TeV track.

A wide range of detector technologies are used in the MS including monitored drift tubes (MDT), multi-wire proportional chambers (cathod strip chambers, CSC), resistive plate chambers (RPC) and thin gap chambers (TGC), where the last two technologies are used for triggering. For an illustration see figure 5.9.

Monitored Drift Tubes

The MDTs are drift chambers with aluminium tubes filled with a gas mixture containing argon. The chamber sizes increase in direct relation of their distance from the interaction

point. The MDT chambers cover the region $|\eta| < 2.7$, except for the innermost layer where they are replaced by CSC chambers for $2 < |\eta| < 2.7$. The large restitution time inherent to the MDT technology of close to a μs makes it unfit for use at high pseudorapidities with high particle occupancy, but in the central detector region it provides very precise spatial resolution.

Cathode Strip Chambers

The CSC technology is used in areas where the MDT's can no longer cope with the high particle track density. The CSC's measure both track coordinates simultaneously through charge collected on two planes of orthogonal strips. Tracks are measured in four CSC planes, which is less than in the MDT's, but the faster time response helps regain tracking precision. The total area covered by CSC chambers is $\sim$65m^2.

Technologies used for triggering - RPC and TGC

Two complementary triggering systems with high time resolution are in place in the MS with RPC's used in the barrel region and TGC's in the endcaps. The time resolution needs to be on the order of nanoseconds to successfully identify the bunch crossing that each track belongs to. The trigger detectors are required to provide acceptance in the range $|\eta| < 2.4$ and in all ϕ directions.

5.5 The ATLAS trigger system

Given the extremely high luminosity at which the LHC is designed to run, it is impossible to record every single event. At the current 50 ns bunch spacing, bunch crossings occur at a rate of $2 \cdot 1/(50 \cdot 10^{-9}\text{s}) = 40$ MHz. The collision rate is several times higher if one includes pileup. This should be compared to the capabilities of the storage system, which can only record approximately 200 events per second. It is therefore necessary to rely on complex algorithms to quickly select only the events that are interesting for physics analysis. For this purpose the ATLAS trigger system has been developed as a combination of custom built hardware placed locally at the detector followed by a data farm based on commercially available computers.

The trigger system is designed to run in three stages/levels. The hardware based Level 1 (L1) trigger starts by selecting signatures from high-p_{T} particles in the muon spectrometer or calorimeters at reduced granularity. This results in a reduced output rate on the order of 75 kHz. For each accepted event the L1 trigger defines a region of interest (RoI) containing the identified trigger object. Within the RoI the detector information is passed on to the Level 2 (L2) software trigger.

The L2 analyses the data at full granularity and precision within the RoI, which corresponds to roughly 2% of the total event data. This reduces the rate output to approximately 3.5 kHz. The final stage of the event selection is carried out by the event filter (EF), which again reduces the event rate to about 200 Hz, which is able to be written to tape. The EF

analysis procedures are performed offline, and each event takes on average four seconds to process.

Branching can only happen from a lower level trigger to a higher level trigger. So an L2 trigger can only be seeded by one specific L1 trigger, and an EF trigger can only be seeded by one specific L2 trigger.

6 Data retrieval and Monte Carlo

Any experimental particle physics analysis needs data, and lots of it. Statistics is commonly the main limiting factor for both precision measurements and searches for new physics at the energy frontier, this analysis included. It is therefore of utmost importance to collect as much useful data from the available collisions as possible. However, increasing the statitistics indefinitely will not lead to an arbitrarily high precision due to the inherent limitations of the detector. Systematic uncertainties play an increasingly dominant role in the high-statistics limit. Relevant systematic errors for the present analysis will be discussed in chapter 10.

In this chapter an outline is given of how the collected data is prepared for analysis and how R-hadron signal samples are produced and weighted to correspond to the collected integrated luminosity.

6.1 Triggering

Triggers are chosen by considering basic assumptions about the production mechanism described in chapter 2. The most common production channel is predicted to be gg fusion for low masses changing to $q\bar{q}$ annihilation for higher masses, in conjunction with ISR jets.

MET trigger

In searches for rare events only unprescaled triggers are of interest. If only a fraction of the events passing the trigger were kept in the analysis, an unknown part of the signal events would be lost due to this prescaling. This would invalidate the limits on production cross-sections found in the subsequent analysis. The luminosity changed in the LHC throughout 2011 resulting in a varying event rate, and the availability of unprescaled triggers in data changes accordingly for each run period. To obtain the largest possible data sample the unprescaled MET trigger with the lowest cut value available in each run period will be utilised. A summary of these triggers can be seen in table 6.1. For example EF_xe60_noMu is a trigger at Event Filter level demanding a missing transverse energy of at least 60 GeV while being muon system agnostic (being independent of the muon system). Turn-on curves as a function of missing energy for two trigger thresholds are shown in figure 6.2.

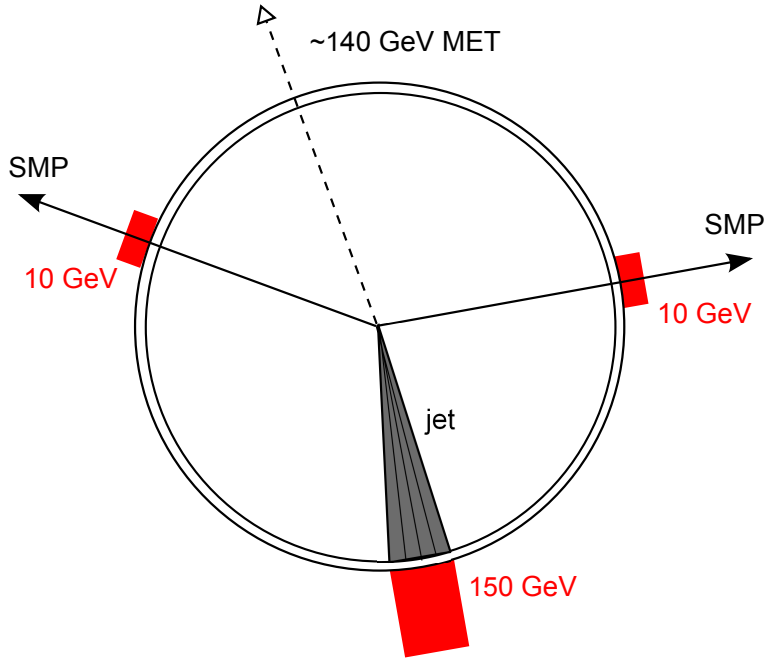

Figure 6.1: An illustration of missing transverse energy in an event with pair produced SMPs and an associated jet.

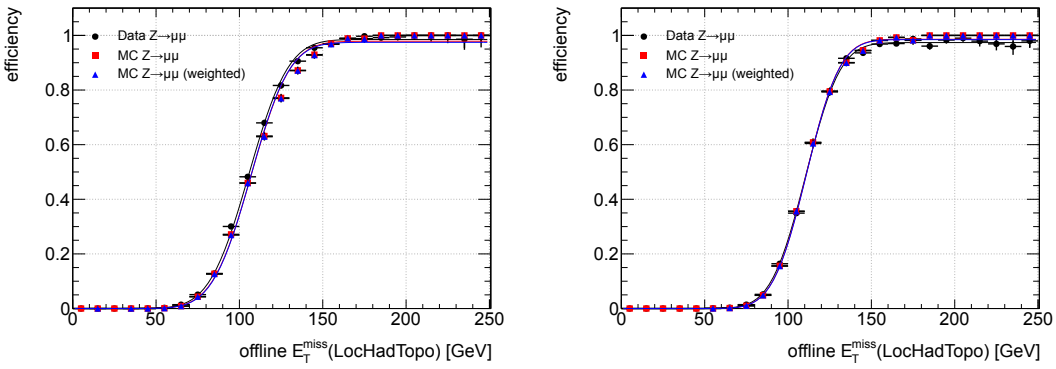

Figure 6.2: Efficiencies of the MET triggers EF_xe60_verytight_noMu (left) and EF_xe70_noMu (right), estimated using $Z \to \mu\mu$ data and MC [43].

Muon trigger

The error calibration on β measurements from MDT's and RPC's in chapter 7 uses unprescaled muon triggers with a threshold of 18 GeV [43]. Offline muons are selected with $p_T > 50$ GeV. Data from the L1 muon triggers is only passed to the high-level trigger if it can be assigned to the collision bunch crossing. Out-of-time particles arriving in the muon system after the following bunch crossing has taken place are therefore not triggered on. Since virtually all triggered particles in data are in-time muons, the efficiency has been estimated using simulations of R-hadrons. The result is shown in figure 6.3. Due to the typically low values of β for heavy R-hadrons the muon triggers have a low efficiency for

Run periods	Trigger
D, E, F, G, H	EF_xe60_noMu
I, J, K	EF_xe70_noMu
L, M	EF_xe60_verytight_noMu

Table 6.1: The lowest unprescaled MET trigger thresholds applied to the data for individual run periods.

this type of event, but the combination of MET and muon triggers does increase the signal efficiency by a few percent.

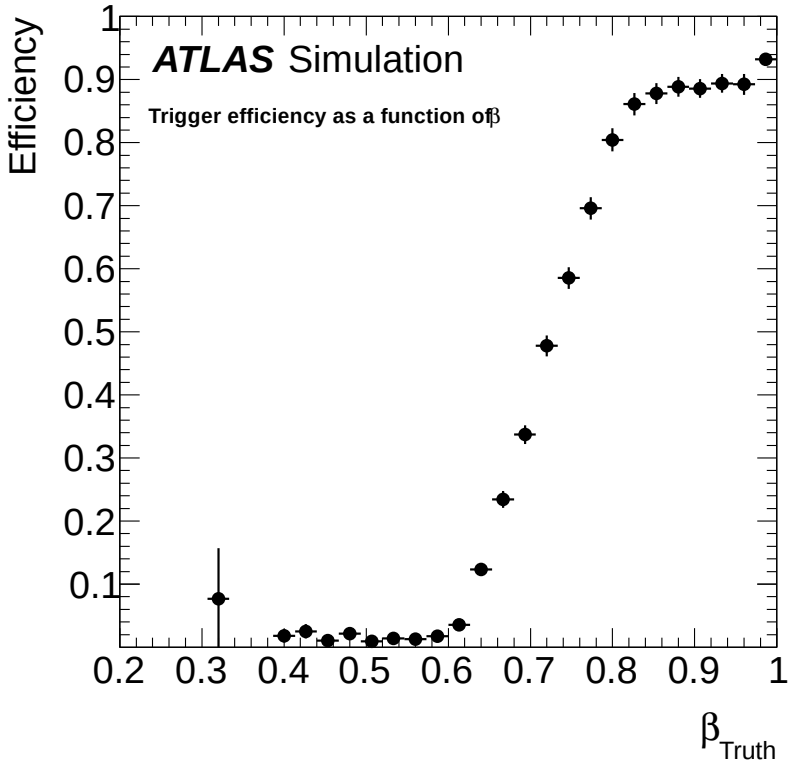

Figure 6.3: Efficiency of the muon trigger for simulated R-hadrons as a function of β [43]. The problem with out-of-time particles begins already at $\beta \sim 0.7$.

6.2 Signal samples

All signal samples have been produced by the ATLAS Central Production and are considered official samples to be used for physics analysis. The simulations were performed at a collision energy of $\sqrt{s} = 7$ TeV corresponding to the LHC operating energy in 2011. 14 mass hypotheses were chosen at fixed mass intervals ranging from 200 GeV to 1.5 TeV. The range of selected masses was chosen based on the theoretically predicted production cross sections of the R-hadrons, which naturally depends on both their mass and the center-of-mass energy of the p-p collisions.

6.2.1 Monte Carlo weighting

Monte Carlo samples are usually produced before or during the corresponding data taking period. Since MC samples should simulate the actual conditions in both the LHC and ATLAS, it is necessary to introduce weighting factors that correct for deviations in the generated amount of integrated luminosity in each data period (event weighting) as well as in the pileup conditions (pileup reweighting [16]) compared to the collected data.

A Monte Carlo sample is produced by requesting the generation of a certain number of events. Consequently, the integrated luminosity of the sample depends on the cross section for the type of generated event. In order to correctly simulate the amount of collected data, the MC sample must be weighted to achieve the same amount of integrated luminosity [16]. The weight can be calculated as

$$W = \frac{\sigma L}{N_0}, \tag{6.2.1}$$

where σ is the cross section of the given process, L is the integrated luminosity and N_0 is the number of generated events in the original sample. This is done with individual weights for each data taking period.

Another effect that must be taken into account is the amount of pileup present in a given event. Since pileup is directly proportional to the instantaneous luminosity, pileup reweighting is performed using the average pileup in each lumiblock, which is the smallest amount of data where the luminosity is determined. The present analysis is applied to slow-moving particles, which makes out-of-time pileup important, that is the pileup originating from previous bunch crossings. Therefore the pileup is also averaged over all bunch crossing IDs (BCIDs) in a lumiblock. These are unique IDs given to each possible combination of two bunches moving in opposite directions.

As the signal samples are generated with gg fusion and $q\bar{q}$ annihilation separately, it is also necessary to apply a weight factor to each event based on the relative production cross sections of the two contributions. If N_{gg} and $N_{q\bar{q}}$ are the number of generated events for each production type while σ_{gg} and $\sigma_{q\bar{q}}$ are their individual production cross sections, the relative weight factors k to be applied are

$$(k_{gg}, k_{q\bar{q}}) = (\sigma_{gg}, \sigma_{q\bar{q}}) \cdot \frac{N_{gg} + N_{q\bar{q}}}{\sigma_{gg} N_{gg} + \sigma_{q\bar{q}} N_{q\bar{q}}}. \tag{6.2.2}$$

Table 6.2 shows the production cross sections for each investigated mass hypothesis estimated with Pythia. The cross section ratio is seen to change from gg fusion dominated at the low masses to $q\bar{q}$ dominated at higher masses.

The generated MC sample is thus weighted with a constant factor W to have the same integrated luminosity as data in each data taking period, as well as on a per lumiblock basis using the average pileup $\langle\mu\rangle_{\mathrm{LB,BCID}}$ over all bunch crossing IDs in the lumiblock, and lastly with a factor k depending on the relative abundance of gluino pairs in the two production channels.

$m_{\tilde{g}}$ [GeV]	σ_{gg} [pb]	$\sigma_{q\bar{q}}$ [pb]
200	430.51	43.84
300	35.38	7.13
400	4.76	1.67
500	0.87	0.48
600	0.19	0.15
700	$4.63{\cdot}10^{-2}$	$5.51{\cdot}10^{-2}$
800	$1.26{\cdot}10^{-2}$	$2.07{\cdot}10^{-2}$
900	$3.69{\cdot}10^{-3}$	$8.16{\cdot}10^{-3}$
1000	$1.13{\cdot}10^{-3}$	$3.22{\cdot}10^{-3}$
1100	$3.62{\cdot}10^{-4}$	$1.32{\cdot}10^{-3}$
1200	$1.15{\cdot}10^{-4}$	$5.43{\cdot}10^{-4}$
1300	$3.85{\cdot}10^{-5}$	$2.23{\cdot}10^{-4}$
1400	$1.32{\cdot}10^{-5}$	$8.99{\cdot}10^{-5}$
1500	$4.44{\cdot}10^{-6}$	$3.64{\cdot}10^{-5}$

Table 6.2: The gluino pair production cross sections for gg fusion and $q\bar{q}$ annihilation at each mass hypothesis. Notice the change in relative size at each end of the mass range.

6.3 Data samples

The data samples used in the present analysis have been collected during the 2011 run of the LHC. The total amount of data collected during this period corresponds to 4.7 fb^{-1}. Two data streams were chosen for different purposes. Calibration studies made use of the Zmumu data stream containing muons reconstructed to originate from a Z boson, while the R-hadron search was done using the JetTauEtMiss stream, which is made for reconstruction and calibration of hadronic and tau jets as well as missing energy in the ATLAS calorimeters.

6.3.1 Good run list

During data taking it is important to keep track of the status of all the subdetectors in ATLAS. Specific detector parts could be offline or faulty during a period where data taking continues in the rest of the detector. During operation a database is updated with the status of all detector parts at any given time. This enables the generation of good run lists (GRL) for any data stream or any subset of the collected data. If some of the detector parts relevant for a particular data stream are malfunctioning or have unacceptable performance, the problematic luminosity blocks (lumiblocks) are omitted in the good run list. This is a list of all lumi blocks where the detector performance was optimal. If problems arise in only part of a lumi block, the whole lumi block is generally discarded. However, certain detector performance groups have optimized the data rejection further.

Tools are available for generating a personal customized good run list if necessary, but this is customarily limited to the production of a single common good run list used by all

members of an analysis group to ease comparison of results. The analysis in this thesis is done based on a previously generated good run list from the ATLAS SUSY Working Group. The GRL is also needed to get a correct estimate of the total integrated luminosity of the accepted data. Luminosity calculation has been done using the ATLAS Luminosity Calculator [15].

6.3.2 LAr error

In the LAr calorimeters the overall quality of the data taken is transferred to a flag called 'LAr error'. This can have three values reflecting whether the data was without problems (0), contained problems but was recoverable (1) or was irrecoverable (2). ATLAS requires that all corrections and calibrations of LAr data is completed within a 36 hour period, after which the physics data streams are processed. An example of a LAr error of value 1 is a subset of data that was not calibrated within this time frame. An irrecoverable LAr error of 2 can be due to corruption of data or large changes in the detector conditions within a run. All data with a LAr error value below 2 is considered acceptable.

6.3.3 Initial data reduction (Skimming)

The analysis is done using D3PD ROOT ntuples generated locally at the Niels Bohr Institute from the ATLAS ESD files. In this way the ESD data objects are converted to a flat data structure divided into "containers" for each collision event. Each container consists of a vector for each physics variable. Accessing the data belonging to a particular reconstructed particle in an event is then equivalent to reading a specific entry in each vector in the relevant container.

6.3.4 Track reconstruction and truth matching

Tracks can be reconstructed as standalone tracks in the Inner Detector with an algorithm such as *trkpt5*, as muons in the MS, or as combined tracks if a satisfactory match is found between the reconstructions in the two detector parts. Several reconstructions are available such as *mu_muid* and *mu_lowbeta*. The former is the reconstruction of choice for the error calibration of MDT and RPC speed measurements in chapter 7, while the latter muon reconstruction will be used for momentum estimation for the simulated R-hadrons in chapter 12 since it is optimised for track fitting on low β particles.

In addition to the various track reconstructions the MC simulation ntuples contain *truth* data, which is the exact values of mass, momentum, direction in η–ϕ etc. given to the particle at event generation. The truth data may be linked to the reconstructed tracks through a Monte Carlo id number for each tracks, but if no such id numbers are provided then track matching must be performed if truth data is needed. The matching is done by minimising the value of

$$\Delta R = \sqrt{(\eta_{\text{reco}} - \eta_{\text{truth}})^2 + (\phi_{\text{reco}} - \phi_{\text{truth}})^2} \tag{6.3.1}$$

by looping over all reconstructed tracks for a given truth object. If the closest reconstructed

track in η–ϕ space has ΔR_{min} less than some threshold value, the truth data is attributed to the track.

Part III

Development of the β discriminator

7 Calorimeter data calibration

In order to gain knowledge about the existence of R-hadrons, it is necessary to discriminate the R-hadrons (signal) from all Standard Model processes (background) as efficiently as possible. The highest discriminatory power is achieved by discarding as much background as possible while still identifying a large fraction of signal events, i.e. having a high signal efficiency. In this chapter a description is given of the methods used to develop and optimise the measurement of a particle's speed β and its associated error σ_β using the ATLAS calorimeters.

The presented work in this chapter is a contribution to the official 2012 ATLAS search for heavy long-lived sleptons and R-hadrons [43]. This article will be referred to in the following as the collaborative effort. Although the final search presented in later chapters is only based on particle speeds measured in the calorimeters, the contribution to the collaborative efftort has been the calibration of such measurements in both calorimeters and muon spectrometer (MDT and RPC). All three calibrations are presented but with emphasis on the calorimeter calibration.

7.1 Reconstruction of time and β measurements

The search for exotic stable massive particles (SMPs) and the calculation of the mass of SMP candidates is highly dependent on the ability to make precise measurements of their speed. Theories involving slow moving particles ($\beta \ll 1$) enable the isolation of candidates using Time-of-Flight (ToF) measurements. The ATLAS Tile and LAr calorimeters have sufficiently high timing resolutions to distinguish highly relativistic SM particles from the slower moving SMPs. The time resolution depends on the energy deposited in the cell and also the layer type and thickness, but typical numbers are 2 ns at 1 GeV, and generally better for the Tile calorimeter as seen in figure 7.12.

To ensure the highest possible timing accuracy in each calorimeter layer it is necessary to calibrate the data using particles with known speeds. It is then possible to shift the ToF values such that they are in agreement with the known values. The viability of such a calibration depends on the assumption that the particles used for calibration have similar characteristics to the SMPs in question when depositing energy in the calorimeters. In the present analysis both muons and jets are considered for this purpose. It is expected that more detected energy depositions will be present for jets in the calorimeters than for muons, resulting in differing detector responses to be compared with the simulated R-hadron signal samples. Since simulations are used to predict the discovery potential of the R-hadrons in

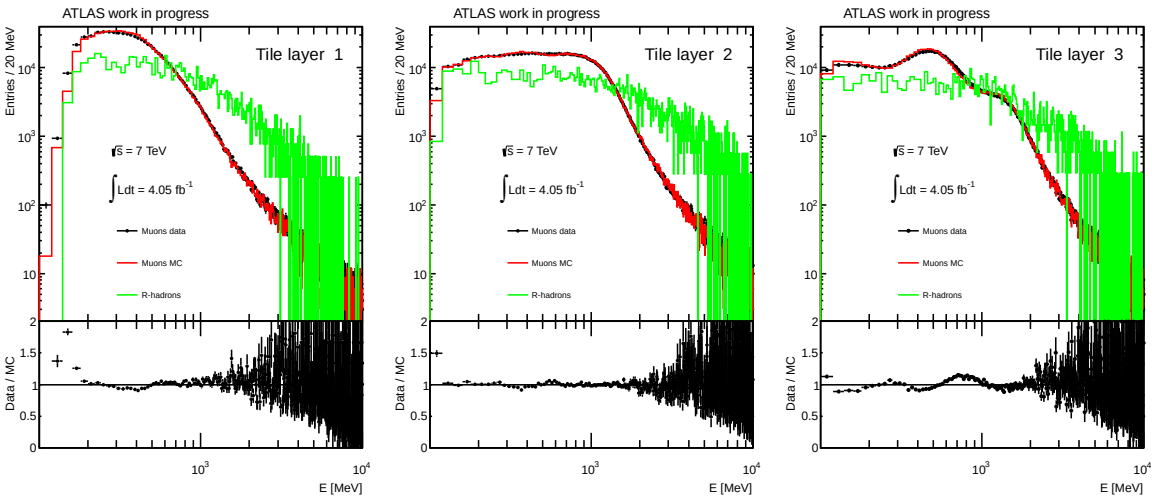

Figure 7.1: The distribution of energy depositions in the three layers of the Tile calorimeter for muons data and Monte Carlo as well as R-hadrons with masses of 100 GeV to 1 TeV. The MC and signal distributions have been scaled to the same area as data for better comparison.

different mass ranges, it must also be ensured that Monte Carlo is in agreement with data. If the simulations do not account for all sources of statistical uncertainty, the ToF values can be smeared by comparing to data using error propagation.

One of the main backgrounds to the signal of R-hadrons arises from muons. This is yet another motivation for calibrating the cell timing using muons to increase the accuracy of the resulting β measurements. This will result in better separation between signal and muons.

This chapter contains the following parts. First, the principle behind timing measurements is explained. The methods for calibrating ToF measurements from data and Monte Carlo are then introduced. Subsequently the calculation and weighting of particle β values from individual cells belonging to the same reconstructed track is given, and several methods of data reduction are discussed to minimize the muon and jet backgrounds. A final study of the errors on β is then undertaken in section 7.2 to ensure accurate error estimation.

7.1.1 Muon and jet selection

To ensure high quality samples of muons and jets, a range of initial quality cuts are performed. The chosen cuts follow the recommendations of the Combined Muon Performance Group and the Jet Working Group. The specific cuts for the muon and jet selection are shown in table 7.1. As a final cleaning measure, an overlap removal with loose electrons is performed.

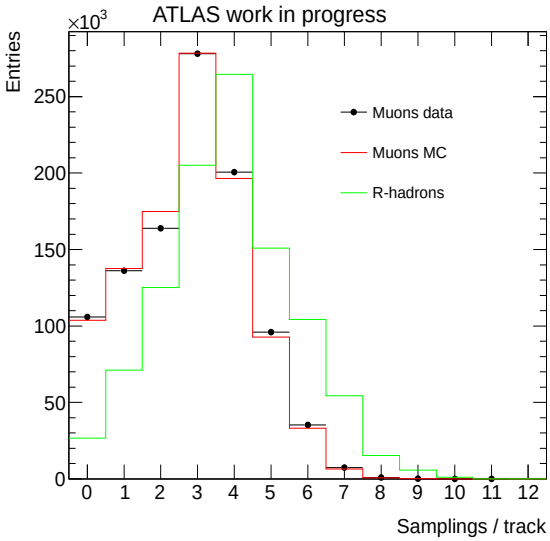

Figure 7.2: The total number of samplings left by each muon and R-hadron track when passing through the ATLAS calorimeters. The MC and signal distributions have been scaled for comparison. The signal distribution is taken for a combination of R-hadron samples in with masses between 100 GeV and 1 TeV.

Muon selection
A designation of at least 'loose' is required
At least 1 hit in the Pixel B layer if B layer hit expected
At least 2 Pixel hits or dead Pixel sensors traversed
At least 6 SCT hits or dead SCT sensors traversed
A maximum sum of 2 Pixel holes or SCT holes traversed
At least 6 TRT hits or outliers and less than 90% outliers (for $\lvert\eta\rvert < 1.9$)
$p_T > 10$ GeV
$\lvert M_{Z,\mathrm{reco}} - 91.1876\mathrm{GeV}\rvert < 5$ GeV
Jet selection
A designation of at least 'tight' is required
$p_T > 10$ GeV

Table 7.1: Cleaning of muon and jet samples for use in the calorimeter calibration.

7.1.2 Measuring Time-of-Flight

The convention in the ATLAS calorimeters is to reconstruct the Time-of-Flight of particles such that $t_{\mathrm{reco}} = 0$ is the ToF of a relativistic particle produced at the primary interaction point. This value is thus displaced from the actual time t by an interval depending on the calorimeter cell. The relation between the reconstructed and actual times can be written as

$$t_{\mathrm{reco}} = t - \frac{d_{\mathrm{cell}}}{c}, \tag{7.1.1}$$

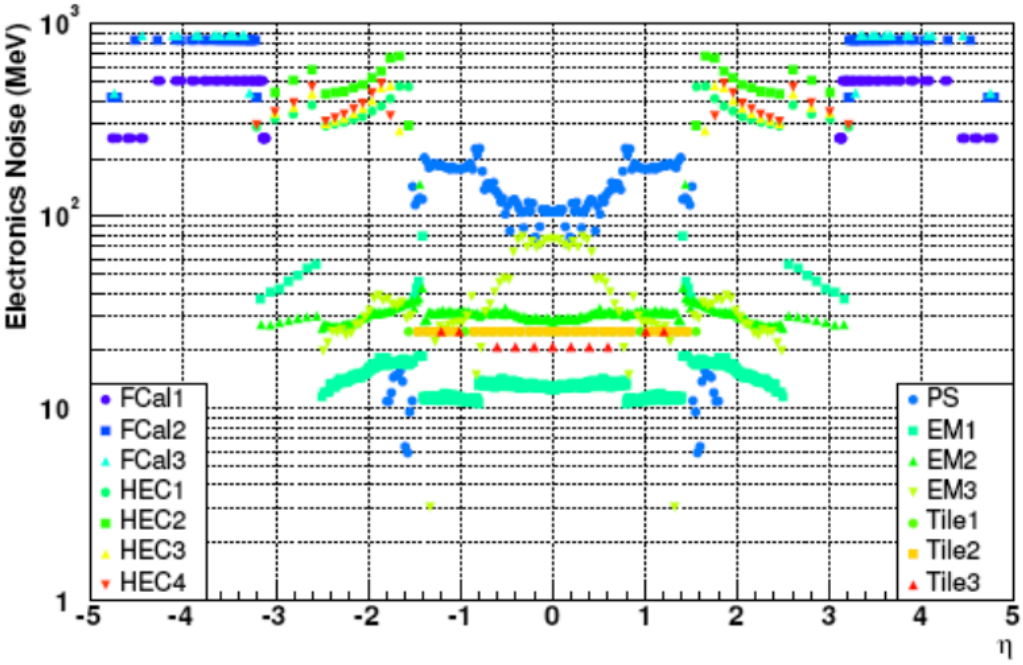

Figure 7.3: Incoherent noise in the ATLAS calorimeters as a function of peudorapidity. Energy measurements below these thresholds are inaccurate and are discarded.

Barrel layer	PS	EM1	EM2	EM3	Tile1	Tile2	Tile3	
Energy cut [MeV]	100	100	100	100	100	100	100	
Endcap layer	PS	EM1	EM2	EM3	HEC1	HEC2	HEC3	HEC4
Energy cut [MeV]	200	200	200	200	500	500	500	500

Table 7.2: Minimum values of the energy depositions used in the analysis for each layer in the ATLAS calorimeters.

where d_{cell} is the distance from the interaction point to the central point of the cell. Energy depositions from e.g. relativistic muons or jets would therefore be reconstructed with values of t_{reco} centered around zero. The slower moving SMPs would instead be reconstructed with positive values of t_{reco} determined by the distance to the cell and the deviation of its speed from c.

The calorimeter cells have an inherent noise level, which must be taken into account if their measurements are to be trusted. This is an unavoidable fluctuation added to each calorimeter cell signal, which is independent of the collision environment. This incoherent signal noise of each calorimeter layer varies, and minimum values for accepted energy deposits used in the analysis are summarised in table 7.2. These values have been extracted from the plot in figure 7.3.

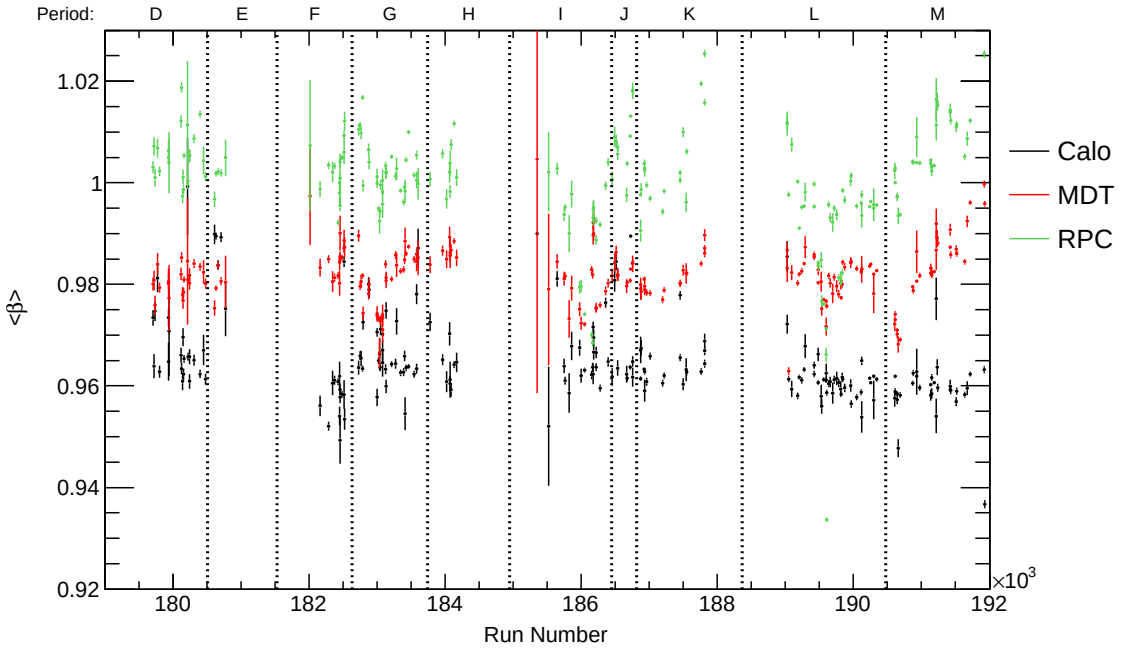

Figure 7.4: The observed misalignment of the ATLAS and LHC clocks as seen in β measurements from the calorimeters, MDT and RPC as a function of run number.

7.1.3 Calibration of reconstructed cell times

To ensure that the SMP search is based on the most precise data possible, the reconstructed cell times are calibrated before calculating and weighting the corresponding β values. The calibration makes use of the fact that virtually all muons and jets are produced at relativistic speeds with $\beta \sim 1$. The distribution of cell times is therefore expected to follow a Gaussian distribution centered at $t_{\text{reco}} = 0$. The actual detector data is observed to have distribution means deviating from zero. Furthermore, this deviation is dependent on the cell energy deposition. To correct this, the data is divided into 45 energy bins in the range 100 MeV – 15 GeV with the first and last bin being overflow and underflow. From each bin the mean and width of the distribution of reconstructed cell times are obtained, where the width is obtained as the standard deviation of all data points. It could also have been done using a Gaussian fit, which could decrease the influence of outliers in the distribution, but fit stability considerations and the general high quality of the muon and jet samples spoke in favor of avoiding the fits. The means are subsequently used to calibrate the cell times by subtracting them from the t_{reco} values belonging to the respective energy bins.

The analysis also makes use of Monte Carlo simulations. To predict the behaviour of the signal left by R-hadrons it is paramount that the simulated data accurately describes the detector performance. Since a large discrepancy is observed between the standard deviations of cell time distributions in data and simulation, the MC distributions are smeared to agree with data. The MC simulation is run using both muons and jets, each with individual calibration values. This is done to investigate whether the expected energy depositions of R-hadrons are best described by muons or jets.

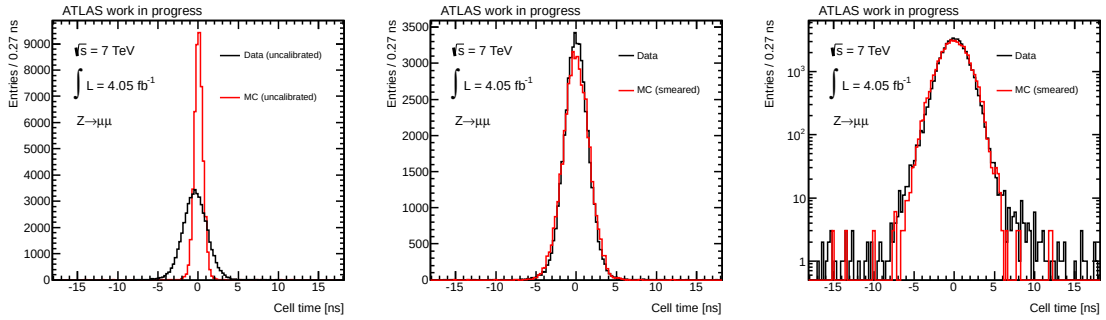

Figure 7.5: Left: A comparison of reconstructed cell times for energy depositions in the range 450 MeV $< E <$ 500 MeV. Middle: The same cell time distributions calibrated according to equations 7.1.2 and 7.1.3. Right: A logarithmic plot of the calibrated distributions.

Alignment of ATLAS and LHC clocks

The distribution of t_{reco} in the whole detector is observed to have a mean deviating from zero. This overall shift in the timing is dependent on the run number, with the shift attributed to a relative misalignment of the ATLAS and LHC clocks. The shift is corrected for the entire detector as a whole, since the source of the shifts is assumed to be an overall shift of the ATLAS clock. The effect of this shift was subtracted from all calorimeter time measurements before performing any further calibrations. Since the basic time data was not available for the MDT and RPC, a visualisation of the shift has been made using particle speeds as seen in figure 7.4.

Calibration versus energy

The calibration of cell times in data is given by:

$$t_{\text{reco}}^{\text{cal}} = t_{\text{reco}} - \mu_{\text{data}}(E) \tag{7.1.2}$$

For Monte Carlo the calibration is given by:

$$t_{\text{reco}}^{\text{cal}} = t_{\text{reco}} - \mu_{\text{MC}}(E) + r.\text{Gaus}(0.0, \sigma_{\text{smear}}) \tag{7.1.3}$$

where $r.\text{Gaus}(\mu,\sigma_{\text{smear}})$ is a random number taken from a gaussian distribution with mean μ and spread σ_{smear}.

The amount of smearing given by σ_{smear} in a given energy bin is found from combination of errors:

$$\sigma_{\text{smear}}(E_i) = \sqrt{\sigma_{\text{data}}(E_i)^2 - \sigma_{\text{MC}}(E_i)^2} \tag{7.1.4}$$

In figure 7.12 the values of μ and σ from data are displayed as a function of energy for each of the 14 calorimeter layers. Optimally, a continuous function should be fitted to the σ-values to be used when assigning an error to each reconstructed cell time. As described in [2] the resolution can be approximated by two contributions combined in quadrature:

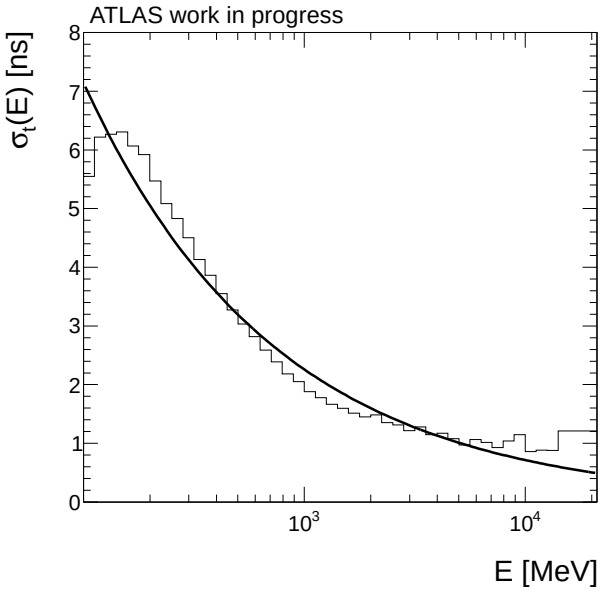

Figure 7.6: A fit using function 7.1.5 to the uncertainties of reconstructed cell times in Tile layer 1 as a function of energy deposition. The approximation fails at both high and low energies. The errors are negligible and are not shown.

$$\sigma_t(E_i) = \frac{p_0}{\sqrt{E_i}} \oplus \frac{p_1}{E_i} = \sqrt{(\frac{p_0}{\sqrt{E_i}})^2 + (\frac{p_1}{E_i})^2} \tag{7.1.5}$$

The first term describes statistical errors, while the second term is due to noise in the electronics. However, for very low energy depositions this overestimates the error, as can be seen in figure 7.6, where the function 7.1.5 has been fitted to the measured uncertainties of Tile layer 1. Since an equivalent function covering the whole energy range is difficult to obtain, a constant value is used within each bin. This will however only have a minimal impact on the analysis since the values are only used indirectly for weighting β-values calculated from t_{reco}. Additionally it is seen in the figures that for wider energy bins the σ-values vary less. In most layers there is a lack of data in several energy bins. To make sure that the calculated values are accurate, it is required that each energy bin has at least 25 entries. Data from bins with less entries is discarded.

7.1.4 Determination of β

Having reconstructed the Time-of-Flight it is possible to formulate the speed β of a particle as a function of t_{reco}:

$$\beta_i = \frac{v}{c} = \frac{d_{\text{cell}}}{tc} = \frac{d_{\text{cell}}}{(t_{\text{reco}} + \frac{d_{\text{cell}}}{c})c} = \frac{d_{\text{cell}}}{t_{\text{reco}}c + d_{\text{cell}}} \tag{7.1.6}$$

7.1.5 Resolution of β

To enable the discrimination of slow-moving SMPs from Standard Model background or to reconstruct their mass, it is important to have a precise measurement of their speed. It is

therefore of high priority to obtain the most precise β value possible. Using the fact that the majority of the particles under consideration leave energy depositions in more than one calorimeter cell, given that they have sufficient energy, the reconstructed β values from each cell can be weighted according to their errors to obtain a more precise estimate. It is however much simpler to initially study the quantity β^{-1}, since this is directly proportional to t_{reco} (see equation 7.1.6). Since this is a direct observable it is expected to follow a gaussian distribution. This justifies the use of the normal weighted average, where each value is weighted according to its inverse error squared:

$$\begin{aligned} \beta^{-1} &= \frac{\sum_{i=0}^{N} \beta_i^{-1}/\sigma^2_{\beta_i^{-1}}}{\sum_{i=0}^{N} 1/\sigma^2_{\beta_i^{-1}}} \\ \sigma^2_{\beta^{-1}} &= \frac{1}{\sum_{i=0}^{N} 1/\sigma^2_{\beta_i^{-1}}} \end{aligned} \tag{7.1.7}$$

Once a properly weighted β^{-1} value has been found, β is simply calculated as its inverse. The error on β is then given by error propagation as $\sigma_\beta = \beta^2 \sigma_{\beta^{-1}}$.

7.1.6 Consistency check

To make sure that a weighted β value makes sense, one can look at the probability that all the data points are in agreement with the weighted value. This is done by calculating the χ^2:

$$\chi^2 = \sum_i \frac{(\beta^{-1} - \beta_i^{-1})^2}{\sigma^2_{\beta_i^{-1}}}. \tag{7.1.8}$$

If the probability of this χ^2 value compared to the number of degrees of freedom is found to be below 0.001 an attempt is made to remove the data point that lies the most standard deviations from the weighted value. The remaining data points are subsequently reweighted but still only accepted if the χ^2 probability exceeds 0.001. No direct cut on the number of samplings is performed in the analysis. If only one sampling is present for a track, the consistency check is not possible, but exclusion of these tracks would remove roughly 10 percent of the data.

The χ^2 consistency check turns out to be detrimental to the signal efficiency in the R-hadron search to a much larger degree than the benefits it provides for background reduction. This selection cut was therefore dropped in the end, but its effects on signal efficiency and the amount of observed data can be seen in table 8.2.

7.2 Further efficiency and calibration studies

7.2.1 Detector response of R-hadrons calibrated with muons and jets

Before continuing with further corrections on the reconstructed particle speeds, a conclusion is needed regarding which timing calibration is to be applied. From the two parallel

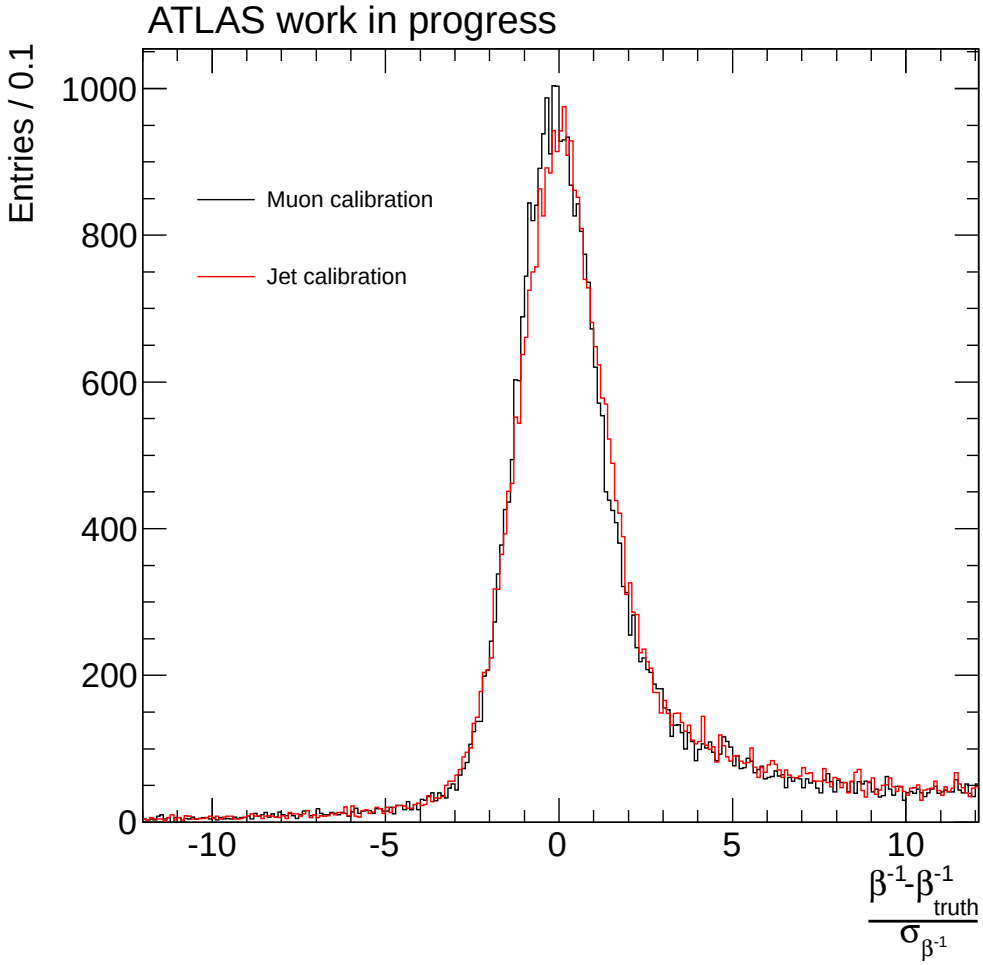

Figure 7.7: Pull plot of β^{-1}-values of R-hadrons calibrated with muon and jet Monte Carlo respectively. The two calibrations have practically the same result.

calibrations developed using muons and jets, the resulting β values are be compared. In figure 7.7 is seen a pull plot giving the deviation of the reconstructed value β^{-1}_{reco} from the MC truth value $\beta^{-1}_{\text{truth}}$ scaled by the error $\sigma_{\beta^{-1}}$. To gain a fair amount of statistics ten signal samples from 200 GeV to 1000 GeV have been combined. The plot gives a sense of how well the β reconstruction is while taking into account how large the errors are. If the pull distributions fail to produce a clear peak around zero, or they are shifted systematically to one side compared to zero, it is a clear sign that the reconstruction is inaccurate. Even the errors can be checked (assuming Gaussianly distributed values) by seeing how much the width of the distribution deviates from unity. Although the reconstruction is not perfect for either calibration, no significant discrepancies are observed between them. The choice therefore falls on the tried and true calibration using muons. For an estimation of the systematic uncertainty induced by the choice of calibration pertaining to the signal efficiency in the R-hadron search in subsequent chapters, see section 10.2.

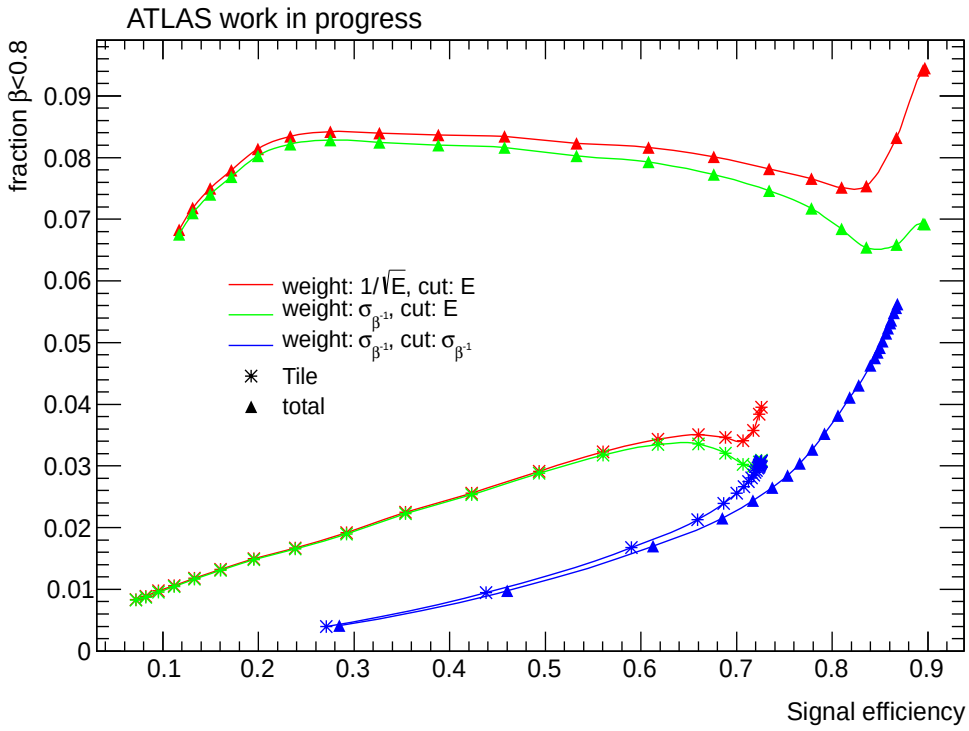

Figure 7.8: The fraction f_β of β measurements for muons with values below 0.8 as a function of signal efficiency.

7.2.2 Optimising data efficiency and reducing background

Due to the very low expected cross section for R-hadrons, the efficiency of the β-measurement must be taken into consideration. It is therefore necessary to investigate how to improve the β resolution and minimise the amount of background while retaining high efficiency. Since R-hadrons are expected to have β values below ~ 0.8, the amount of muons or jets that enter the SMP analysis as background in the R-hadron signal region can be estimated by the fraction of the particles having $\beta < 0.8$. This will be referred to as f_β below. This amount of background should be compared to the efficiency at the given cut. To ensure the lowest possible background at a given efficiency, several methods for data reduction and weighting of the β measurements have been considered. Weighting has been performed using the energy depositions in calorimeter cells as well as using $\sigma_{\beta^{-1}}$. Data reduction has been done by either setting a minimum accepted energy in individual cells or by cutting on $\sigma_{\beta^{-1}}$.

A comparison of $f_\beta < 0.8$ for both muons and jets for three possible combinations of weighting and cuts can be seen if figure 7.8. When using only the three layers in the Tile calorimeter, the efficiency prior to any energy or error cuts is $\sim 70\%$ for muons and $\sim 60\%$ for jets. Both efficiencies are raised to $\sim 90\%$ when including the LAr calorimeters. When applying cuts to the data, the inclusion of the LAr calorimeters only results in a lower f_β when cutting on $\sigma_{\beta^{-1}}$. The advantage of a $\sigma_{\beta^{-1}}$ cut over an energy cut is substantial at all levels of efficiency. This fact can be understood by regarding figure 7.12, where the timing

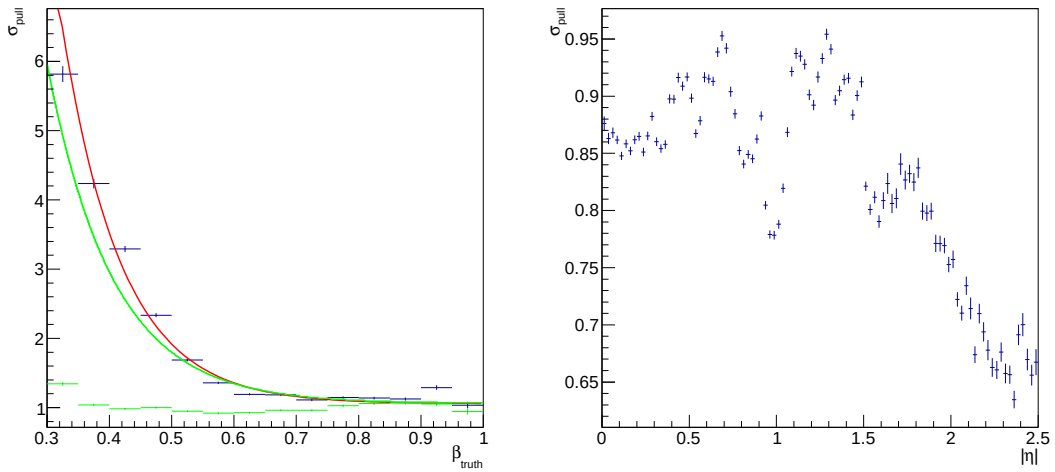

Figure 7.9: Error calibration of weighted β-values for the calorimeters. Left: Calibration as a function of β_{truth} using signal MC. The red curve is the best fit to the data. The green curve is the function used for calibration. The green data points are pull widths after calibration. Right: Calibration factors as a function of pseudo-rapidity using $Z \to \mu\mu$ data. Similar correction curves are obtained for the MDT and RPC.

uncertainty in each layer varies greatly at comparable energies. Choosing a fixed energy cut will therefore remove data with varying uncertainty depending on the layer. Cutting on $\sigma_{\beta^{-1}}$ ensures that only the weighted β-values with the highest uncertainty are removed. This implies the assumption that the calculated errors are accurate, which is looked into in section 7.2.3.

7.2.3 Final corrections of σ_β

Once the analysis has yielded weighted β values for a large data sample, it is possible to investigate how well the calculated σ_β values are in agreement with the actual spread of β values. All further investigations of errors should ideally be performed on $\sigma_{\beta^{-1}}$ to retain the gaussian shapes, but due to the lack of calibrated time data for the MDT and RPC, all three technologies are treated in the same manner by considering σ_β.

It has been investigated how well the calculated errors describe the width of the β-distribution. Pull plots with $\frac{\beta-\beta_{\text{truth}}}{\sigma_\beta}$ are filled in bins of β and η to correct for any dependence as a function of these variables. This can be done since the calibration is performed on $Z \to \mu\mu$ data where all the particles have $\beta_{\text{truth}} \simeq 1$. A correction vs. σ_β was also attempted but gave unphysical results, as illustrated on the left in figure 7.10.

The only way to obtain sufficient data for low β values is to use signal MC. A sharp rise in pull width is observed for low β in R-hadron signal samples. Such an increase in uncertainty at low speeds is to be expected, since the timing reconstruction algorithm in the calorimeters is optimised for relativistic particles and cannot retain the same accuracy at all velocities. An exponential fit is performed to describe this rise. All σ_β values are subsequently corrected by multiplication with the value of the exponential function at their respective β values. The best fit to the data is observed to over-correct the errors at the

lowest β values, and hence a slightly less aggressive calibration curve is used.

It has not been possible to devise a suitable fit function to correct for pull width variations as a function of pseudorapidity. Instead the bin values from the histogram are used directly as scaling factors. However, to ensure that the errors are not over-calibrated, a random sample corresponding to half the total data set is used to arrive at the scaling factors. Also, since the η dependence has been observed to be symmetric, the plot is presented as a function of $|\eta|$ to gain statistics in each bin. The calibration curve and factors are shown in the histograms of figure 7.9.

The resulting total β pull width for the calorimeters is shown on the right in figure 7.10. For a plot of the total distribution of weighted β values from data in the calorimeters after corrections, see figure 7.11.

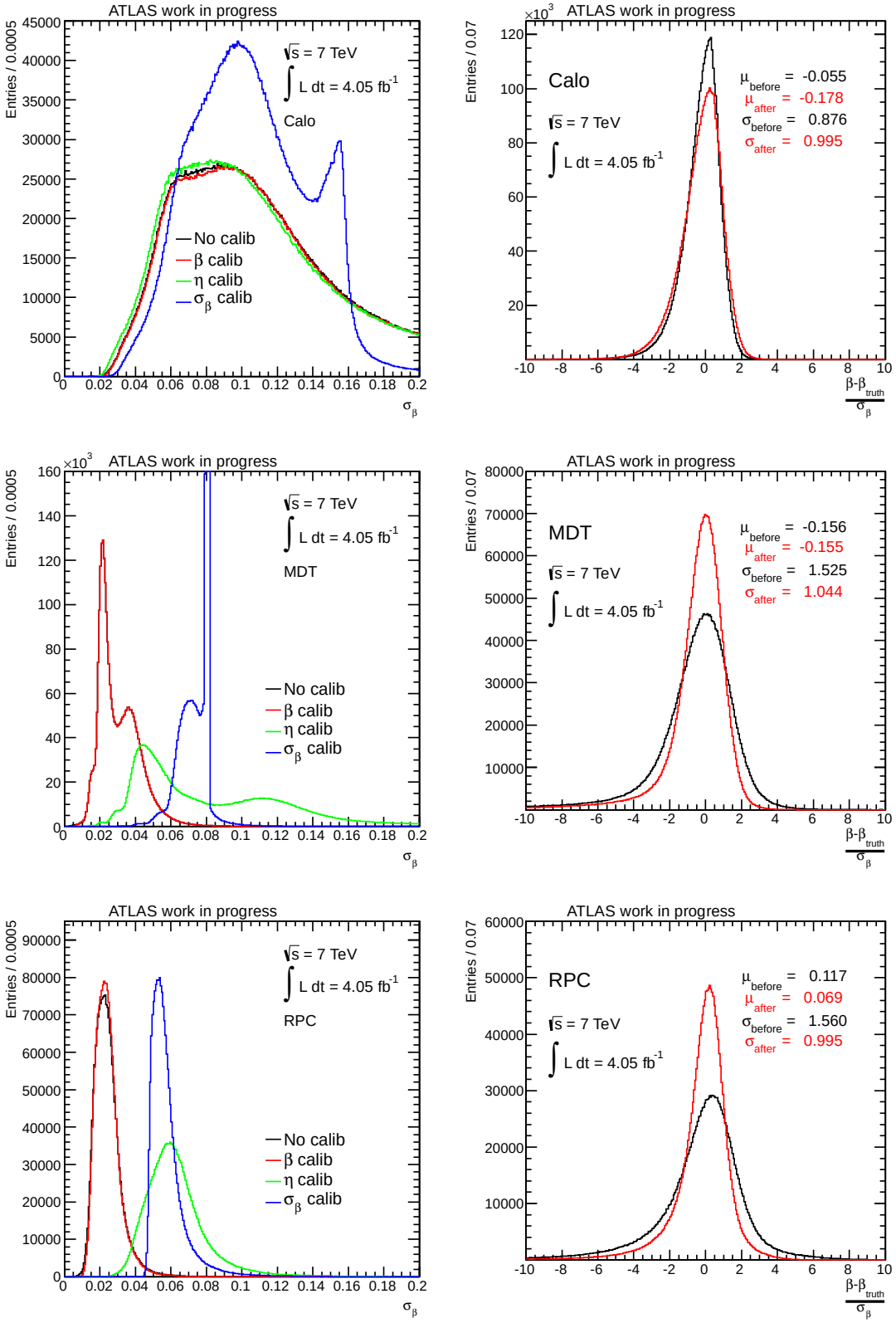

Figure 7.10: Left: distributions of σ_β for the three technologies after each error calibration step. An unphysical peak is seen for the MDT and partially in the calorimeters after the calibration vs. σ_β, and this last calibration step is omitted in the analysis. Right: pull distributions before and after the error correction for all three technologies. Pull widths are significantly closer to the ideal unit value after the correction. For the MDT the mean is not changed considerably. The RPC mean is moved closer to zero, while the calo mean is the only parameter moved further away from the ideal value. The values have been obtained by fitting the central part of the curves with a Gaussian.

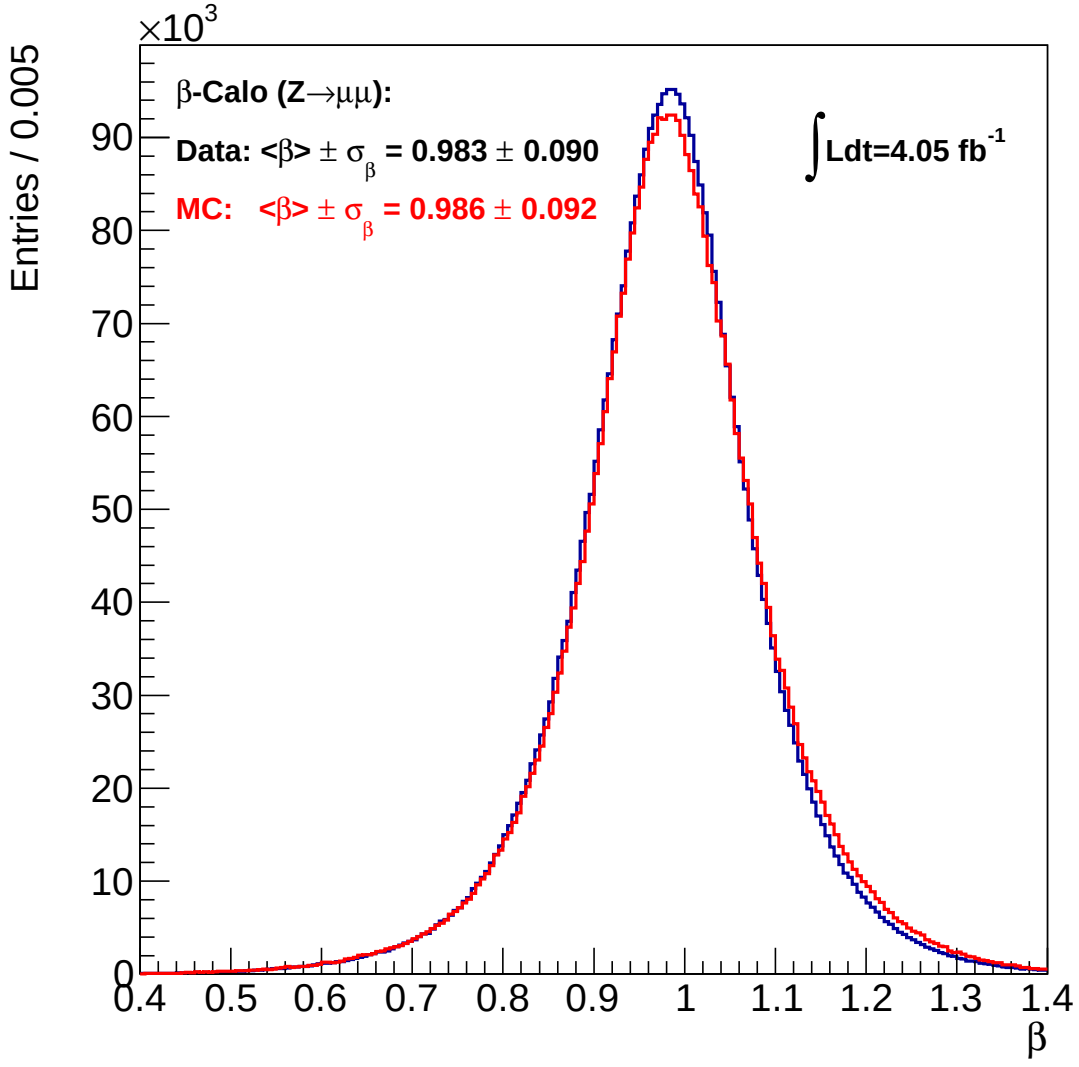

Figure 7.11: The final distribution of weighted β values after σ_β correction.

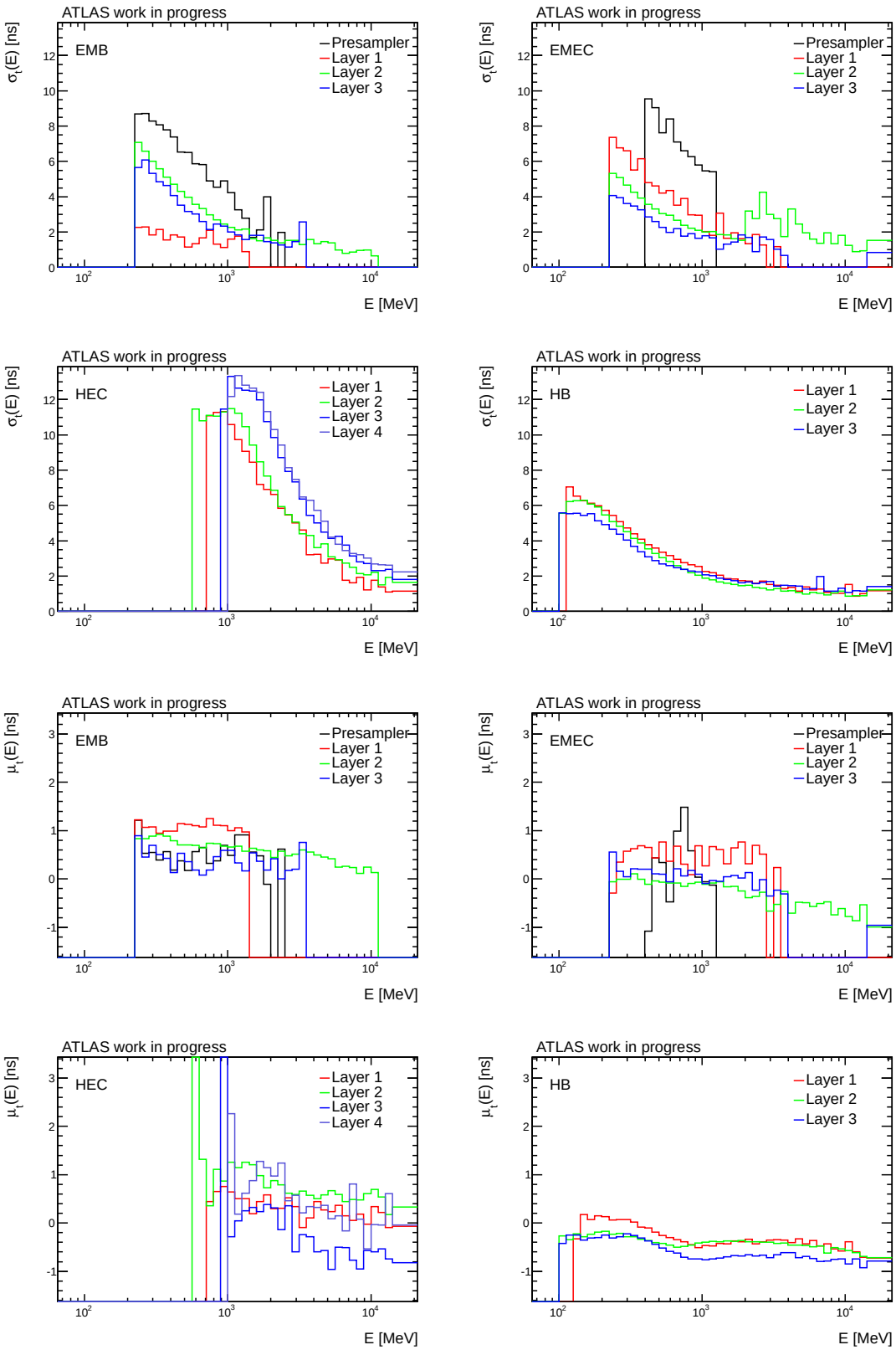

Figure 7.12: Errors (top) and mean values (bottom) of reconstructed cell times for each energy bin. At least 25 data points must be present in a bin for the values to be calculated.

Part IV

Analysis

8 Candidate selection

The selection of R-hadron candidates can be described as a two-part enterprise. The first part is concerned with track reconstruction accuracy and isolation, and is called the *pre-selection*. The second part then uses the available discriminators on the remaining data to optimise the signal over background ratio using Monte Carlo signal samples, resulting in the *final selection cuts*. The measures to ensure data quality as described in chapter 6 are implemented before the pre-selection.

8.1 Pre-selection

To ensure that the search is based on well-reconstructed tracks, a wide range of parameters originating from all parts of the Inner Dectector as well as the LAr and Tile calorimeters are considered. The values of the pre-selection cuts are based on considerations about what is needed to get accurate track measurements and isolation from other types of particles. Some cuts are also based on work done by the Muon Combined Performance Group and the Inner Tracking Combined Performance Group.

Due to the LQS in R-hadrons the quark content could change due to interactions with the detector material. This could lead to R-hadrons that start out neutral (charged) but become charged (neutral) at some point while traversing the detector. The probability of detecting each R-hadron therefore increases with the number of subdetectors used. The choice in this analysis has been to rely on Inner Detector tracks with associated energy depositions in the calorimeters, since calibration constants for the muon spectrometer have not been available. The search is therefore *muon agnostic*.

The theoretical production cross section is event based. Consequently it is imperative to consider at most *one* R-hadron canditate from each event. This is ensured by randomly selecting a single candidate in those cases where more than one reconstructed track passed the preselection in the same event. Extra potential for discrimination could in principle be attained by performing a parallel search only using the events with two candidates. However, this would require the calculation of separate theoretical cross sections as well as background estimation. When relying on a data-driven approach, the latter is not feasible considering the amount of statistics obtained in the 2011 data set. Only about 4% of the events after preselection contain more than one candidate.

Description	Value
Largest number of tracks from any vertex	$N_{\text{tracks}}^{\text{vertex}} \geq 4$
SCT hits (or passed dead sensors)	$N_{\text{SCT}}^{\text{hits}} + N_{\text{SCT}}^{\text{dead sensors}} \geq 6$
TRT hits (within η reach)	$N_{\text{TRT}}^{\text{hits}} \geq 7$ (for $\lvert\eta\rvert < 1.9$)
Longitudinal vertex position	$\lvert z_0\rvert < 10$ mm
Radial vertex position	$d_0 < 2$ mm
Shared Pixel clusters	$N_{\text{Pix}}^{\text{shared}} = 0$
Pseudorapidity	$\lvert\eta\rvert < 2.5$
Transverse momentum	$p_T > 10$ GeV
Total absolute momentum	20 GeV $< p <$ 3.5 TeV
Minimum distance to other high momentum track	$\Delta R_{\text{track}} > 0.25$ (tracks with $p_T > 10$ GeV)
Minimum distance to high momentum jet	$\Delta R_{\text{jet}} > 0.30$ (jets with $p_T > 40$ GeV)
Number of good Pixel clusters	$N_{\text{Pix}}^{\text{good hits}} \geq 2$
Pixel dE/dx value	$0 < dE/dx_{\text{Pix}} < 20$ [MeVg^{-1}cm^2]
Pixel $\beta\gamma$ value	$0 < \beta\gamma_{\text{Pix}} < 10$
β value	$0.0 < \beta < 2.0$
Error on β measurement	$\sigma_\beta < 0.1$
χ^2 probability for combined β	$P_\beta^{\chi^2} > 0.001$

Table 8.1: List of all pre-selection cuts. The top part contains variables found from ID tracking, the center part has Pixel dE/dx measurements, and the bottom part lists the variables pertaining to calorimeter β reconstruction. The last greyed-out selection cut was excluded from the analysis, since the drop in signal efficiency did not justify the small reduction of background.

8.1.1 Description of pre-selection cut variables

After applying MET triggering and the good run list, the pre-selection consists of cuts on the variables seen in table 8.1, where the chosen cut values are also given. The following is a short description of a subset of the the pre-selection variables.

Number of associated tracks

An efficient way to avoid contamination by cosmic particles that happen to be reconstructed as tracks in the detector is to demand that at least *one* primary vertex in any event has more than three associated tracks, which would need multiple simultaneous cosmics to fake. The variable $N_{\text{tracks}}^{\text{vertex}}$ is available directly at D3PD level and gives the number of tracks belonging to the primary vertex with the most associated tracks.

Track isolation

To prevent inaccurate energy measurements in the calorimeters, it must be ensured that a maximum of one particle passes through each individual calorimeter cell at any given time. A track isolation cut is introduced to remove any tracks that are not sufficiently separated in η-ϕ space, through the variable $\Delta R_{\text{track}} = \min\{\Delta R_i\}$, where $\Delta R_i = \sqrt{\eta_i^2 + \phi_i^2}$ with i running over all other reconstructed tracks in the event with $p_T > 10$ GeV. The lowest granularity is found in the LAr hadronic endcap, which has a resolution of $0.2(\eta) \times 0.2(\phi)$.

A compromise between track isolation and loss of statistics has given a cut value of $\Delta R_{\text{track}} = 0.25$.

Jet isolation

In analogy with the above track isolation variable, ΔR_{jet} gives the isolation of a track with respect to all reconstructed jets in the event. The R-hadrons can become jet candidates themselves when depositing energy in the calorimeters. To prevent the removal of the R-hadrons, only jet candidates with $p_T > 40$ GeV are considered when calculating ΔR_{jet}.

Longitudinal and radial vertex position

If the p-p collision is too remote compared to the center of the detector, the reconstruction could be problematic. Also, the η cut on whether or not to demand TRT hits would no longer be accurate if the vertex was off in the z-direction, since it would depend on the sign of η. The longitudinal position with respect to the primary vertex must be kept within $|z_0| < 10$ mm, whereas the radial distance is limited to $d_0 < 2$ mm.

Pixel clusters

If the dE/dx measurement from the Pixel detector is to be trusted, each pixel cluster may only be crossed by a maximum of one track at any given time to prevent simultaneous energy depositions. $N_{\text{Pix}}^{\text{shared}} = 0$ ensures that none of the pixel clusters traversed by a track are shared with other tracks. The algorithm also depends on at least two good dE/dx measurements, making $N_{\text{Pix}}^{\text{good hits}} \geq 2$ another demand to pass the pre-selection.

β measurement

A number of quality assessments are made before allowing the reconstructed β value to pass. If the estimated error σ_β is too large, the measurement is not trusted. If a track produces several measurements of β_i, these are combined and a χ^2 calculated as described in section 7.1.6. If the χ^2 probability is close to zero it means that the measurements are likely to be inconsistent. A sharp rise in the number of tracks is seen for $P_\beta^{\chi^2} < 0.001$. These values are discarded.

Even if the estimated error and the χ^2 probability seem acceptable it is still possible that the β value is clearly wrong. Only values in the interval $0.0 < \beta < 2.0$ are accepted.

Cut	$\tilde{g}_{m=500\text{GeV}}$	$\tilde{g}_{m=900\text{GeV}}$	$\tilde{g}_{m=1300\text{GeV}}$	Data
Triggered	8.9	11.6	9.9	100.0
$N_{\text{tracks}}^{\text{vertex}} \geq 4$	8.9	11.6	9.9	100.0
$N_{\text{SCT}}^{\text{hits}} + N_{\text{SCT}}^{\text{dead sensors}} \geq 6$	8.9	11.6	9.9	99.7
$N_{\text{TRT}}^{\text{hits}} \geq 7$ (for $\lvert\eta\rvert < 1.9$)	8.8	11.5	9.7	99.3
$\lvert z_0\rvert < 10$ mm	8.8	11.5	9.7	98.3
$d_0 < 2$ mm	8.8	11.5	9.7	98.2
$N_{\text{Pix}}^{\text{shared}} = 0$	8.8	11.5	9.7	98.2
$\lvert\eta\rvert < 2.5$	8.7	11.4	9.7	98.1
$p_T > 10$ GeV	8.7	11.4	9.7	95.0
20 GeV $< p <$ 3.5 TeV	8.7	11.4	9.5	93.7
$\Delta R_{\text{track}} > 0.25$	8.7	11.4	9.5	45.6
$\Delta R_{\text{jet}} > 0.30$	8.6	11.3	9.4	16.7
$N_{\text{Pix}}^{\text{good hits}} \geq 2$	8.4	10.9	9.1	15.8
$0 < dE/dx_{\text{Pix}} < 20$	8.4	10.9	9.0	15.8
$0 < \beta\gamma_{\text{Pix}} < 10$	8.3	10.6	8.7	14.4
$0.0 < \beta < 2.0$	8.0	10.4	8.6	13.2
$\sigma_\beta < 0.1$	7.4	9.6	8.1	8.1
$P_\beta^{\chi^2} > 0.001$	6.9	8.8	6.9	8.0

Table 8.2: Pre-selection cut-flow table in percent for three gluino mass hypotheses and data. The percentage of events passing the triggers is only known for Monte Carlo. The last greyed-out selection cut was excluded from the analysis.

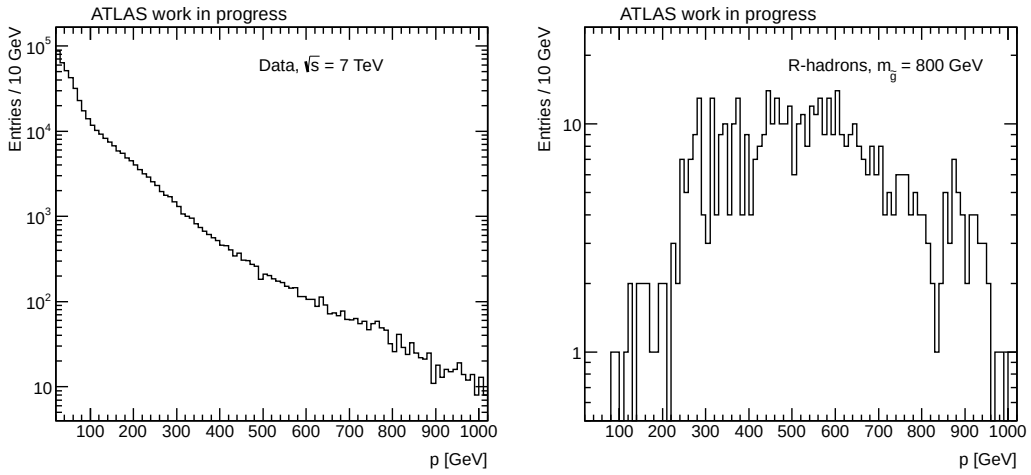

Figure 8.1: The momentum distribution for all data passing the pre-selection cuts (left) and for 800 GeV R-hadrons (right).

8.2 Final selection

The available discriminators for the final R-hadron selection are the momentum p, the particle speed β measured by the calorimeters, the $\beta\gamma$ measurement found from Pixel dE/dx as well as the masses derived from the latter two, m_β and $m_{\beta\gamma}$. These criteria together define the signal region.

8.2.1 Momentum selection

A good starting point for defining an approximate signal region is by studying the momentum distribution. Figure 8.1 shows the momentum of all data passing the pre-selection compared to 800 GeV R-hadrons. The overwhelming majority of the data is situated at low momentum compared to the R-hadrons. The data at low momentum can therefore be used as a region of approximately pure background. A cut for the signal region at $p > 140$ GeV has been chosen based on the signal distributions at all mass hypotheses while ensuring that the signal efficiency is not adversely affected.

By defining the background and signal region in momentum, the selection on the remaining variables can be done by plotting the values in data in the momentum-background region, while the signal events are plotted only for the momentum-signal region.

8.2.2 Selection on β and $\beta\gamma$

To ensure the highest possible signal purity the values of the selection cuts need to be optimised. The following method is only applied to β and $\beta\gamma$. Through the construction of an estimator, each selection variable needs to be divided into an *acceptance region* where the background hypothesis is assumed to be true, and a *critical region* where the signal hypothesis should be true. After optimisation the two regions are then separated by a decision boundary at the value of the selection cut to be used in the analysis. If a

completely specified distribution is given for both background and signal, the Neyman-Pearson test [39] can be used for an N-dimensional parameter space. By constructing a test statistic t and choosing a level of significance α, the power of the test $1-\beta$ can be optimised, where

$$\alpha = \int_{t_{\text{cut}}}^{\infty} f(t|H_0)\mathrm{d}t \tag{8.2.1}$$

$$1-\beta = \int_{t_{\text{cut}}}^{\infty} f(t|H_1)\mathrm{d}t \tag{8.2.2}$$

with H_0 being the background or 'null' hypothesis, and H_1 the signal hypothesis. By constructing a likelihood ratio

$$\frac{f(t|H_1)}{f(t|H_0)} > c \tag{8.2.3}$$

with c in the inequality chosen to correspond to the choice of significance α, the optimal value of t can be obtained. Values of t for which the inequality holds define the region where the signal hypothesis is accepted.

However, the available distributions are not completely specified since they are not continuous. An analytical function cannot easily be obtained to describe the distributions. In such cases several other expressions involving the signal count S and the background B are available for estimating the optimal value to discriminate between signal and background. A Poisson likelihood ratio is advocated by members of the ATLAS Statistics Forum in [42] given as

$$P_1 = \sqrt{2((S+B)\ln(1+S/B)-S)}. \tag{8.2.4}$$

Another commonly used approximation of purity is

$$P_2 = \frac{S}{\sqrt{S+B}}, \tag{8.2.5}$$

while the expression for significance traditionally used to claim discoveries is

$$P_3 = \frac{S}{\sqrt{B}}. \tag{8.2.6}$$

Problems arise with infinities in both expression 8.2.4 and 8.2.6 when the expected background is zero. As this is the case for very low values of β and $\beta\gamma$, the only reliable estimator is expression 8.2.5 which will be used for the cut optimisation.

The optimisations of the β and $\beta\gamma$ cuts are dependent on each other and should in principle be performed using a 2-dimensional integral over both variables simultaneously, but this gives an increase of $N^2 - 2N$ in the number of bins to distribute the data in. The available statistics is not high enough to reliably perform the cut optimisation in this manner. Instead, the following procedure is used (for each mass hypothesis separately) as a compromise:

1. Create two histograms with the same number of bins. Fill one with background and the other with signal. Do this for both β and $\beta\gamma$.
2. For each variable, scale the two histograms to have the same integral/area.
3. Calculate $P = S/\sqrt{S+B}$ with the decision boundary placed at every bin in the histograms to find the optimal cut value P_{opt}.
4. Find max $\left\{P^{\beta}_{\text{opt}} \cdot \varepsilon_{\beta}, P^{\beta\gamma}_{\text{opt}} \cdot \varepsilon_{\beta\gamma}\right\}$, where ε is the efficiency of the respective selection variable.
5. Apply the cut associated with the maximum P-value found in the previous step and refill the histograms belonging to the other selection variable.
6. Repeat step 2 and 3 to find the cut value for the second selection variable.

Since no a priori knowledge is assumed regarding the production cross section of gluinos in any of the mass hypotheses, nothing can dictate how to scale the signal histograms. Optimal cut values could vary with the assumed scale factor. The chosen convention is to scale the signal histogram to the same area as data, which leads to a comparison between signal and background based solely on the shape of the distributions. Accordingly, the obtained cut values are conservative since the expected cross section is lower than what is implied by the chosen scaling.

8.2.3 Selection on m_{β} and $m_{\beta\gamma}$

The two masses m_{β} and $m_{\beta\gamma}$ are naturally highly correlated since their calculations share the same momentum measurement. Instead of a significance-based selection as in section 8.2.2 the mass variables will define the final signal region through the geometric shape of their distribution. The signal will resemble a two-dimensional Gaussian, and the lines of constant value in such a Gaussian are always ellipses. One way to perform the mass selection is therefore to define the size and shape of an ellipse by choosing a percentage of coverage, or equivalently a number of standard deviations, which then defines the signal region.

By obtaining the covariance matrix $\mathbf{\Sigma}$ and the mean values $\bar{m}_{\beta}$ and $\bar{m}_{\beta\gamma}$ for the distributions of reconstructed masses in the signal samples, the signal region can be defined as the area for which the following inequality holds [44]:

$$(\mathbf{m} - \bar{\mathbf{m}})^T \mathbf{\Sigma}^{-1} (\mathbf{m} - \bar{\mathbf{m}}) < k, \tag{8.2.7}$$

where $\mathbf{m} = (m_{\beta}, m_{\beta\gamma})$ and k is the χ^2 value corresponding to the coverage. As an example, a 2σ coverage with two degrees of freedom gives $k \simeq 6.18$.

Using only this ellipse would diminish the signal efficiency, since the part of the signal with very high values of the mass estimates will lie outside the ellipse although no background is expected here. A remedy would be to take the union of the area covered by the ellipse and the area defined by $m_{\beta} \geq \bar{m}_{\beta} \wedge m_{\beta\gamma} \geq \bar{m}_{\beta\gamma}$. The approach using the 2D elliptical area has been an attempt at an alternative way of defining the signal region. Although

it gives the area with the highest concentration of signal for a given percentage of coverage, it accepts more background than necessary. An obvious choice is simple 1D selection cuts at $M - 2\sigma$ from a Gaussian fit to the m_β and $m_{\beta\gamma}$ distributions, where M is the mass of the produced R-hadrons. The ellipse includes lower values along the $m_\beta = m_{\beta\gamma}$ line, which is where the background is most prevalent. It therefore leads to less powerful limit setting for the lower mass hypotheses, where there is significant background, while the limits on R-hadrons with high masses are almost unchanged compared to the 1D cuts. The analysis will therefore be based on the 1D cut approach to attain the strongest achievable limits on production cross sections, but with the elliptical signal region included in the plots as a showcase. Examples of the mass signal regions for two R-hadron mass hypotheses are shown in figure 8.2.

The optimal way to select the signal region would be to calculate $S/\sqrt{S+B}$ for every bin in the 2D mass histogram and rank them accordingly. A rank threshold could then be obtained by demanding a certain coverage. This would ensure the lowest amount of background with the highest signal efficiency. However, time restrictions did not allow the inclusion of this method.

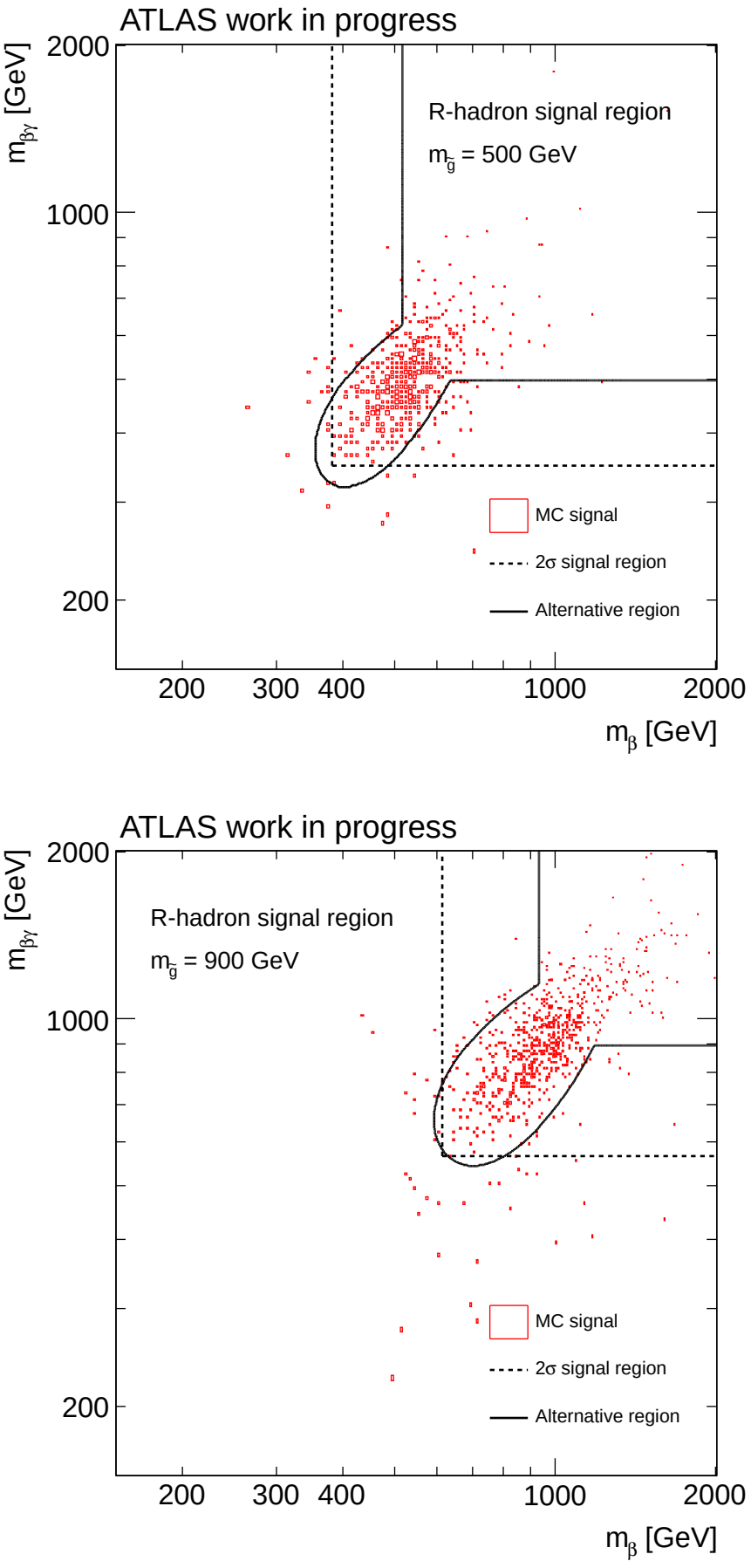

Figure 8.2: Signal regions for the two mass cut methods for $m_{\tilde{g}} = 500$ GeV (left) and $m_{\tilde{g}} = 900$ GeV (right).

9 Background estimation

During the decision stage of the collaborative effort [43] it was found that the Monte Carlo simulations were unable to accurately predict the amount of background at high masses due to insufficient statistics. Also, the finer details of the β and $\beta\gamma$ distributions were not recovered in simulations. Consequently, a data-driven approach which does not use MC has been chosen to estimate the amount of background in the R-hadron search.

9.1 Initial considerations

When estimating the amount and shape of the background directly from data, caution is needed to ensure that no undesirable effects are included. It is not possible to avoid that signal is included in the data used for simulating the background. A decisive factor for the feasibility of the method is therefore the assumption that the signal to background ratio is very small, ensuring that the effects of the included signal are negligible.

Correlations between the variables used to generate the background (henceforth the 'source variables') also have to be considered. The background is needed in the form of masses, which are calculated as

$$m = \frac{p}{\beta\gamma}. \tag{9.1.1}$$

Two different masses m_β and $m_{\beta\gamma}$ are calculated using the measurement of β and $\beta\gamma$ respectively. In the calculation of m_β the γ-factor is found using $\gamma = 1/\sqrt{1-\beta^2}$. Although m_β and $m_{\beta\gamma}$ are clearly correlated, the source variables β and $\beta\gamma$ should each be as uncorrelated as possible with respect to the momentum p. The most abundant background consists of minimum ionizing particles (MIPs) traveling at relativistic speeds and having no particular correlation between their energy deposition in the detector and their mass/speed. The variables used to calculate discriminators for the search (ToF, p, dE/dx) can therefore be considered approximately independent. A small correlation could be present through their dependence on pseudorapidity η, which can be reduced by making sure that each mass is generated using values from the same η region.

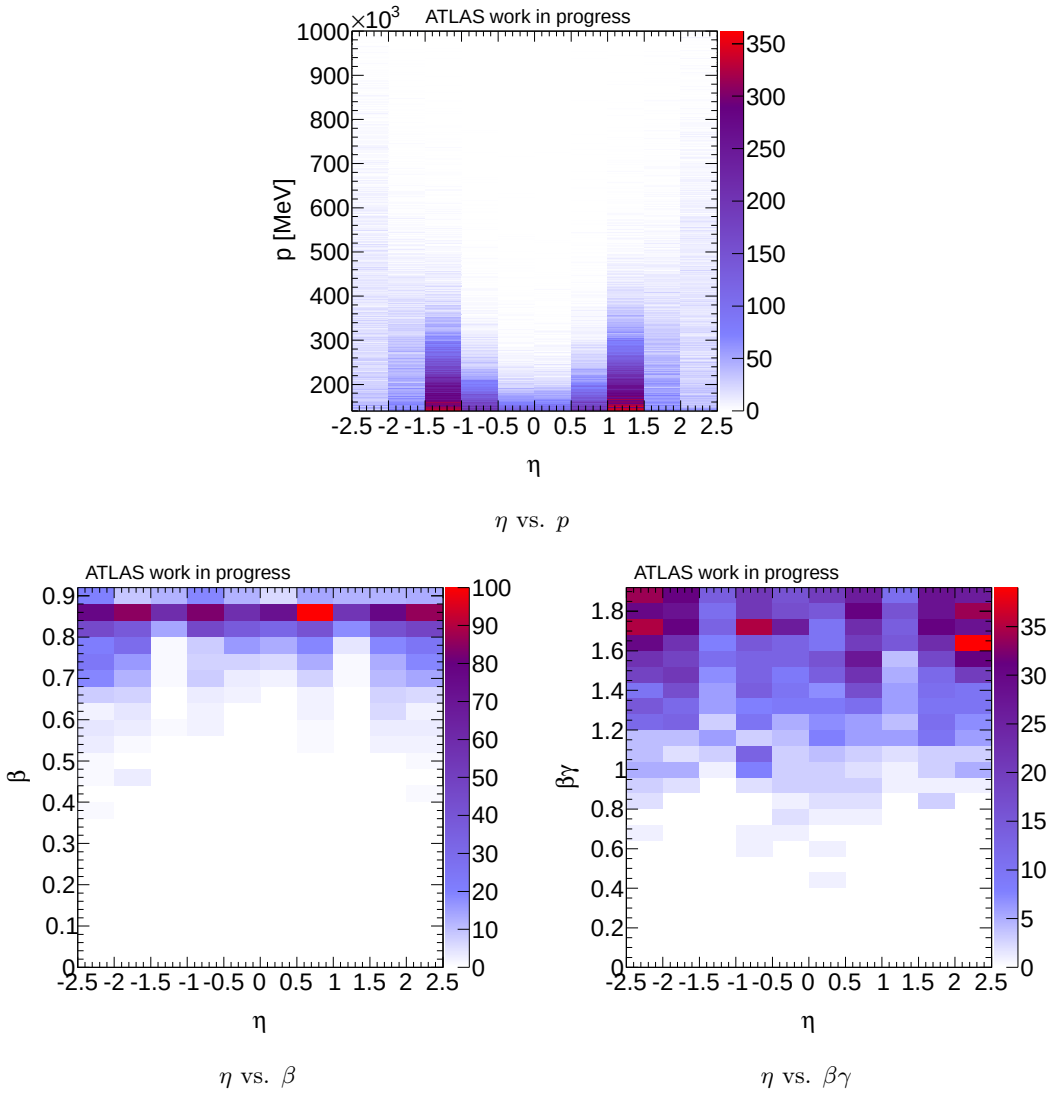

Figure 9.1: An example of the three background source histograms for 200 GeV R-hadrons.

9.2 Preparing source histograms

The background generation is based on a random sampling of three 2D source histograms that are filled with η values paired with values of p, β and $\beta\gamma$ respectively. The distributions of data in the three histograms define the probability density functions for selecting values used to generate the masses. An example is shown in figure 9.1.

Background that shows up as R-hadron candidates in data is necessarily subject to exactly the same selection cuts as the signal events. To accurately predict the shape of the background, all pre-selection cuts as well as the final cuts from sections 8.1 and 8.2 (except the mass cuts) should be applied before filling the three source histograms. Treating data and the input to the background generation in an identical manner should in principle ensure that the estimated background mimicks the background in data as

Histogram	Cuts applied
η–p	Preselection, p
η–β	Preselection, p, β, $\beta\gamma$
η–$\beta\gamma$	Preselection, p, β, $\beta\gamma$

Table 9.1: Cuts applied before generating background.

closely as possible.

However, a few compromises have to be made due to lack of statistics. Firstly, only the final momentum cut is applied to the η–p histogram. Secondly, the high mass hypotheses need extra attenton. After applying the final momentum cut and the β and $\beta\gamma$ selection cuts found in section 8.2 the resulting η–β and η–$\beta\gamma$ source histograms for mass hypotheses above ∼1000 GeV have very low statistics. This can easily lead to an uneven distribution of the estimated background in an $(m_\beta, m_{\beta\gamma})$ histogram with visible 'striping' as a result of re-using the same few values to calculate the masses. The chosen compromise is to reduce the number of bins in the η–β and η–$\beta\gamma$ histograms. The descriptive power of the data-driven background method is thereby potentially reduced, but it results in a more evenly distributed background, since the values are chosen according to the distribution in the bins and not the exact values of their content.

9.3 Generating background

Once the source histograms have been prepared, a random η–p pair is chosen from the first histogram using the *GetRandom2* function of the *TH2* class. Values of β and $\beta\gamma$ are then sampled from the remaining two histograms in the same η bin. If that particular η bin contains no data, which can happen occasionally for the highest mass points, the η value is discarded and a new one is generated. Equation 9.1.1 is then used to calculate the two mass values. Repetition of this procedure results in a chosen total number of 300000 events describing the shape of the estimated background.

Apart from the background shape, the actual amount needs to be estimated. By comparing the integral of the mass sideband below the two final mass cuts in the generated background and in data, a scale factor is found and applied. The distributions of background, data and signal for two specific mass hypotheses are illustrated in figure 9.3.

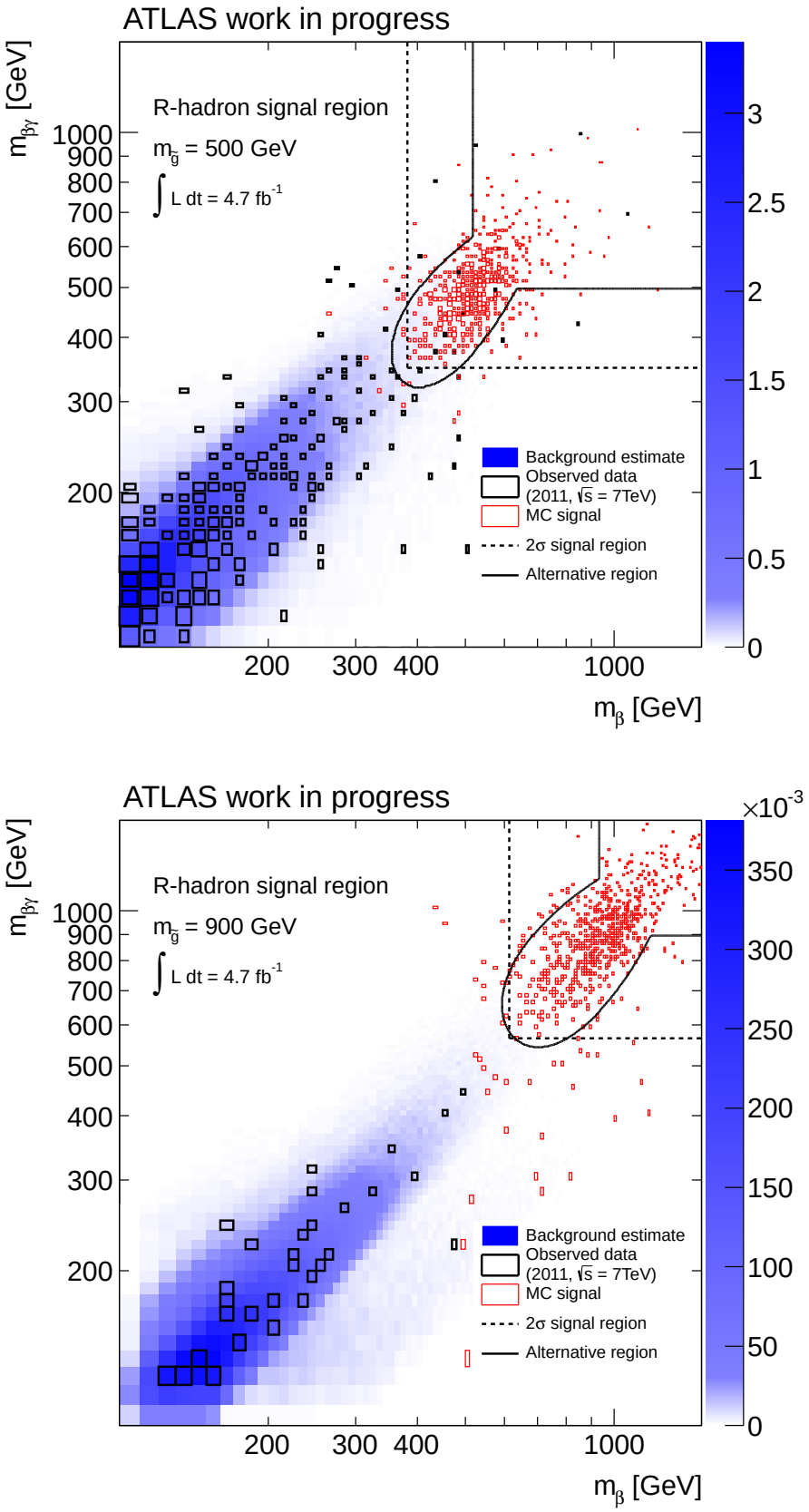

Figure 9.2: 2D view of the distributions of background, data and signal for $m_{\tilde{g}} = 500$ GeV (top) and $m_{\tilde{g}} = 900$ GeV (bottom).

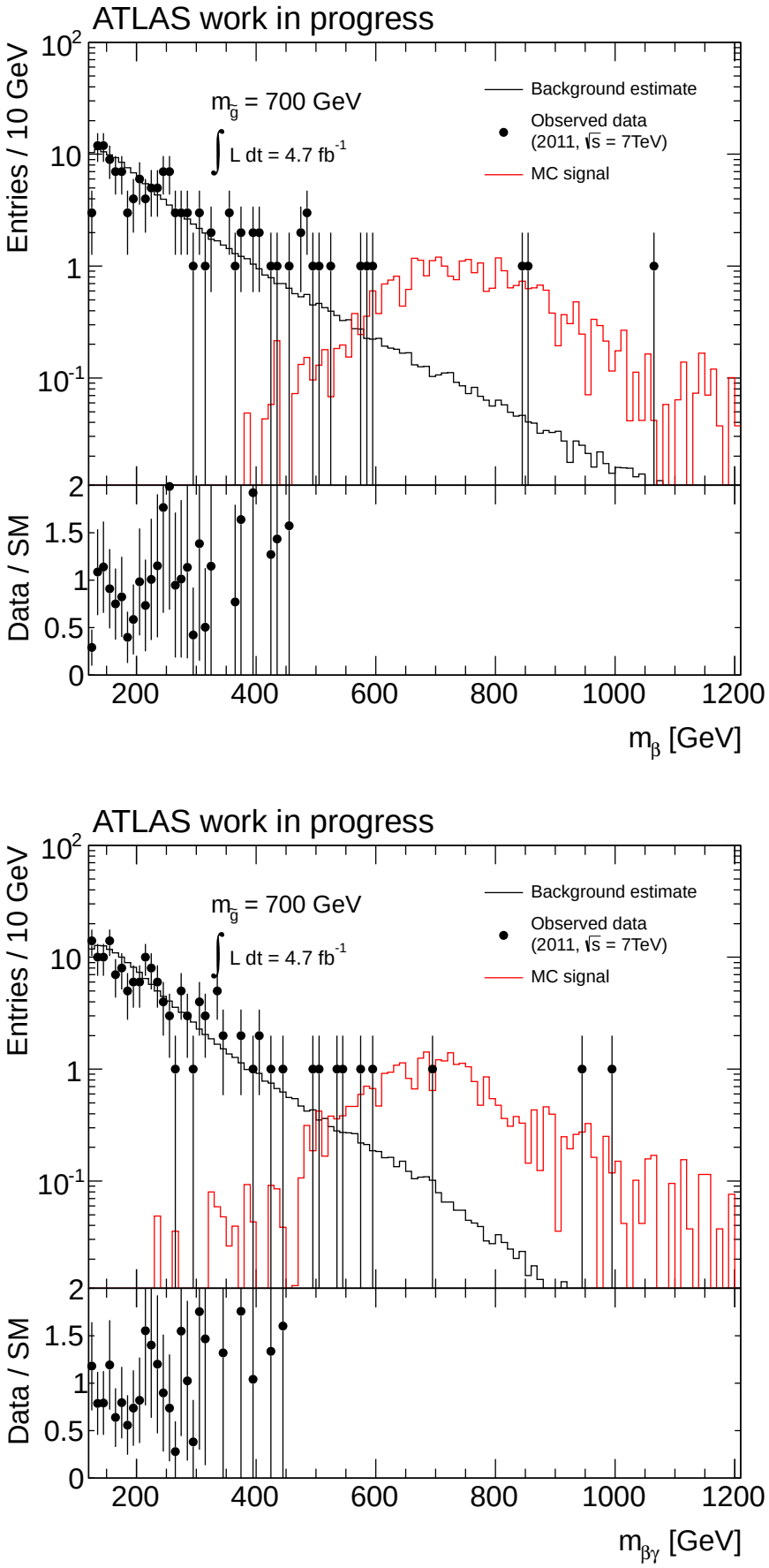

Figure 9.3: Distributions of m_{β} (top) and $m_{\beta\gamma}$ (bottom) showing background, data and signal for $m_{\tilde{g}} = 700$ GeV.

10 Systematic uncertainties

Uncertainties arising from other sources than statistical fluctuations need to be taken into account to realistically estimate the errors on a measurement. Such *systematic* uncertainties can come from an abundance of sources when dealing with an experiment on the complexity scale of a modern particle detector. If e.g. the momentum of the particles was systematically measured a certain number of MeV too high compared to the correct value, this would invalidate the simple error estimation based on the standard deviation of the distribution of measurements, and the error would propagate through to any quantity calculated using the momentum.

It can be extremely difficult to identify and estimate all sources of systematic uncertainties in a particular experiment, and there is never any guarantee that all such errors have been taken into account. The studies of systematic errors presented in the sections below represent both the work of the author and that of the collaboration.

10.1 Theoretical uncertainties

Prospino cross sections

The theoretical production cross section for gluinos is not known to arbitrary precision. Within a specific model, parameters such as the renormalisation and factorisation scales influence the calculated value. To estimate the uncertainties on the calculated cross section these scales are varied. The concensus in the community has become the procedure to set the scales at the mass of the final state particles and to change the values up and down by a factor of two. This leads to a theoretical error of 15-30% on the cross sections depending on the mass hypothesis.

Production and interaction models

The chosen model for the production of R-hadrons through hadronization of the gluinos and the model for their interactions with the detector can lead to variations in the number of detected R-hadrons and thus on the experimental limit. It can be discussed at length how wide the selection of models should be when determining this uncertainty. This analysis will follow the argument in [43] and restrict the applicability of the obtained result to the specific R-hadron model used in Pythia to generate the signal samples. The size of the incongruence between realistic models was in the cited paper found to be on the order of 20%.

10.2 Experimental uncertainties

Luminosity

A study dedicated to the determination of luminosity at $\sqrt{s} = 7$ TeV was conducted by the ATLAS Collaboration in 2011 [45]. The systematic uncertainty on the luminosity measurements was estimated to be 3.7%.

Initial and final state radiation

The amount of ISR and FSR is an important factor in the efficency of the MET trigger. To get a large amount of missing transverse momentum to trigger on, the R-hadrons need to be boosted through the production of a jet stemming from a gluon emitted in the initial of final state. In the collaborative R-hadron search [43] the uncertainty on the trigger efficiency was evaluated by simulating 1 TeV gluino pair production in Pythia while varying the amount of ISR and FSR. The variation in the trigger efficiency between the samples was found to be 7.4% by applying the XE60_noMU trigger onset curve.

MET trigger efficiency

An uncertainty on the MET trigger efficiency also needs to be obtained by comparing data and MC. In [43] this was done using high-p_T $Z \to \mu\mu$ events. The trigger onset was evaluated by fitting the distributions in data and MC to the function

$$\varepsilon(E_T^{\text{miss}}) = \frac{A}{2}\left[1 + \text{erf}\left(\frac{E_T^{\text{miss}} - B}{\sqrt{2}C}\right)\right], \tag{10.2.1}$$

where A is the plateau value reached after the onset, B is the effective E_T^{miss} threshold at 50% efficiency and C is the standard deviation of the Gaussian function modelling the slope. The estimate was obtained by considering the relative difference between $Z \to \mu\mu$ data and pileup-reweighted MC, as well as $\pm 1\sigma$ variations of the B and C parameters. A total systematic uncertainty from these contributions was found to be 4%.

Pre-selection efficiency

If the selection efficiency is different in data and MC it should be included as a systematic uncertainty on the signal efficiency. For simplicity, the efficiency studies are done using the pre-selection cuts only (i.e. not considering the final p, β and $\beta\gamma$ cuts). The uncertainty can be found in two ways. The first way would be to run through all cuts to find a combined efficiency of all pre-selection cuts. This will give an estimate of the total uncertainty on the efficiency after pre-selection. If one suspects a few specific selection cuts to skew the result too much, an RMS of the individual cut efficiencies is an alternative.

Table 10.1 clearly shows that the β related cuts are the biggest contributors to the difference in efficiency between MC and data. Disregarding the small fraction of very low speed ($\beta \lesssim 0.5$) R-hadrons having large errors (figure 7.9), σ_β is expected to be distributed at lower values on average for R-hadrons compared to muons due to their higher number

Cut	Data	MC	$\tilde{g}_{m=1000\text{GeV}}$
$N_{\text{tracks}}^{\text{vertex}} \geq 4$	100.0	100.0	100.0
$N_{\text{SCT}}^{\text{hits}} + N_{\text{SCT}}^{\text{dead sensors}} \geq 6$	100.0	99.8	99.4
$N_{\text{TRT}}^{\text{hits}} \geq 7$ (for $\lvert\eta\rvert < 1.9$)	100.0	100.0	99.4
$\lvert z_0\rvert < 10$ mm	99.8	99.5	100.0
$d_0 < 2$ mm	100.0	100.0	100.0
$N_{\text{Pix}}^{\text{shared}} = 0$	100.0	100.0	100.0
$\lvert\eta\rvert < 2.5$	100.0	99.5	99.8
$p_T > 10$ GeV	100.0	99.2	100.0
20 GeV $< p <$ 3.5 TeV	100.0	99.7	99.8
$\Delta R_{\text{track}} > 0.25$	98.6	99.9	99.8
$\Delta R_{\text{jet}} > 0.30$	98.5	99.8	98.8
$N_{\text{Pix}}^{\text{good hits}} \geq 2$	99.3	98.4	96.2
$0 < dE/dx_{\text{Pix}} < 20$	100.0	100.0	100.0
$0 < \beta\gamma_{\text{Pix}} < 10$	97.3	97.8	98.4
$0.0 < \beta < 2.0$	95.2	93.2	99.3
$\sigma_\beta < 0.1$	62.0	60.2	94.7
$P_\beta^{\chi^2} > 0.001$	99.4	99.7	88.4

Table 10.1: Individual pre-selection cut efficiencies for $Z \to \mu\mu$ in data and MC as well as 1000 GeV R-hadrons.

of energy depositions (figure 7.2). The efficiency reduction by the σ_β cut is therefore less drastic in the R-hadron signal samples than for muons as seen in table 10.1. Hence, the σ_β cut is less dominating for R-hadrons, and the estimate from the $Z \to \mu\mu$ samples would put too much weight on this particular cut.

An RMS of the deviations between each cut was therefore used to estimate the systematic uncertainty, which was found to be 0.9%.

Pileup conditions

Although MC has undergone pileup reweighting as described in section 6.2.1, the conditions in data can rarely be reproduced exactly. A study was conducted to ensure that any lingering uncertainties on the selection efficiency due to pileup were accounted for. For a signal sample of 800 GeV R-hadrons the events were divided into a sample with low pileup ($N_{\text{vertex}} \leq 8$) and a sample with high pileup ($N_{\text{vertex}} > 8$). The pre-selection efficiency for the sample with low pileup came out as 9.7%, while the sample with high pileup had an efficiency of 9.5%. The relative difference of 2.1% can be taken as an estimate of the uncertainty due to pileup variations.

Momentum resolution

The tracking is in general very well described in MC [43] giving a very low systematic uncertainty. An estimate using ID smearing from 2010 data was found by the local group

at NBI to be 1.3%. This number overestimates the error since the tracking performance has increased since 2010, and the quoted error can be considered a conservative estimate.

β calibration uncertainty in the calorimeters

The calibration constants for the offsets and resolutions of the calorimeter timing have been produced using both muons from $Z \to \mu\mu$ events as well as jets from di-jet events. To check whether the choice of calibration has any effect on the signal efficiency, the β values of a signal sample with 800 GeV R-hadrons were calculated using both calibrations, which can be seen in figure 10.1. Two systematic effects were considered, one being the total number of accepted measurements between the two distributions, and the other being the fraction of events with $\beta > 0.9$. The efficiences of the total number of measurements are $3344/10000 = (33.44 \pm 0.47)\%$ for the muon calibration and $3331/10000 = (33.31 \pm 0.47\%)$ for the jet calibration. The uncertainty due to the timing calibration can therefore be estimated to be below 0.5%.

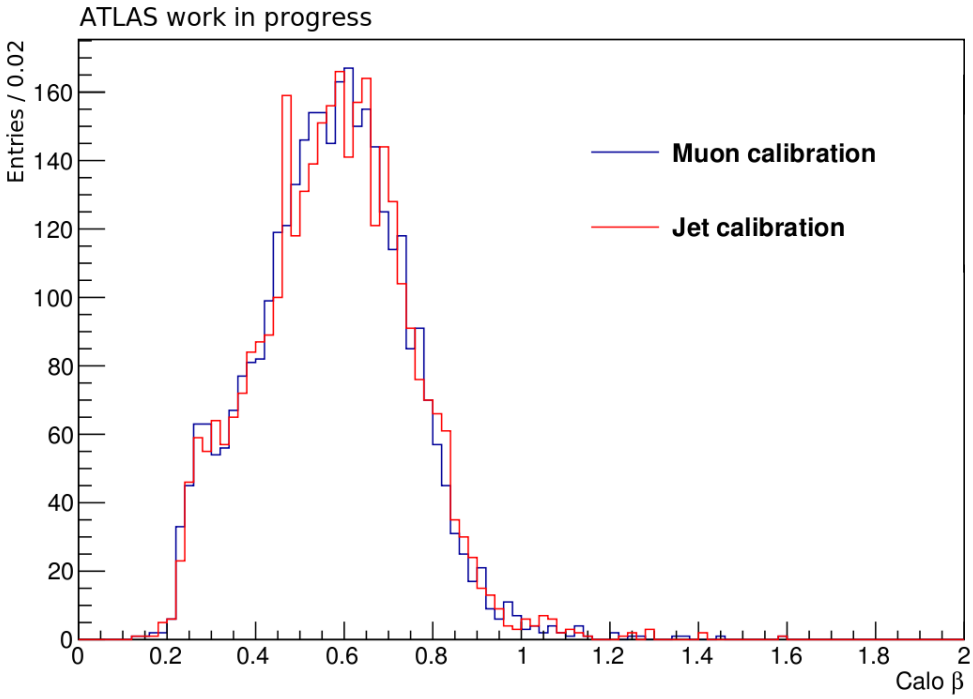

Figure 10.1: The β distribution for the 800 GeV R-hadron signal sample calibrated with calorimeter timing data from muons (blue) and jets (red). The distributions are in good agreement.

The timing reconstruction from energy depositions in the calorimeters is based on a sampling of the signal each 25 ns. The reconstruction is calibrated to give the most precise measurement for $t = 0$ ($\beta = 1$). Particles with considerably lower speeds can lead to a bias in the value of t. The bias in the LAr calorimeters compared to the true time is shown to the left in figure 10.2 as a function of the true time. It is seen that for slower particles the reconstructed time is underestimated by an increasing amount. Applying these values to the time measurements from the LAr calorimeter layers results in the red histogram to the

right in figure 10.2, which shows the number of β values for 1000 GeV R-hadrons residing in the signal region ($\beta < 0.8$) before and after applying the effect. The variation in the number of of particles within the signal region is less than 1%.

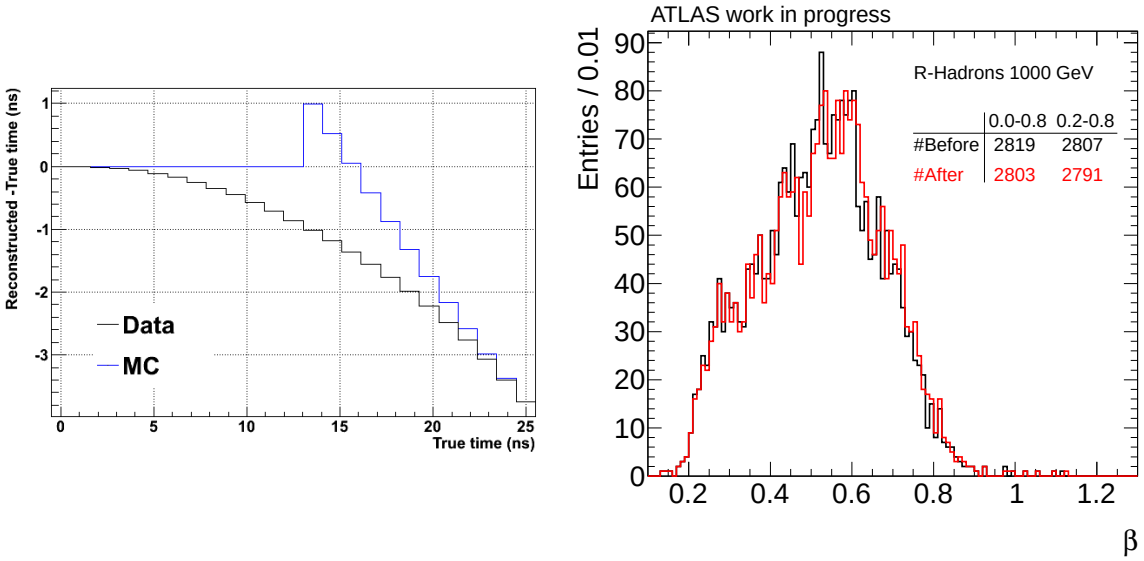

Figure 10.2: Left: the bias of the reconstructed time in the LAr calorimeters compared to truth [54]. Right: the effect of applying the LAr timing bias to 1000 GeV R-hadrons.

Background estimation

With the chosen data-driven method for background estimation, the precision of the background generation depends on the statistics available in the high mass region. The uncertainty on the final estimated background has been evaluated by studying the signal region for R-hadrons with low (500 GeV) and high (1000 GeV) mass respectively. The uncertainty due to low statistics was found by dividing the source histograms into two exclusive samples of the same size. The distribution of m_β for the two samples generated for 1000 GeV R-hadrons is shown in figure 10.3.

The relative difference between the background estimates in the two samples was 2% for 500 GeV R-hadrons, while the background for 1000 GeV R-hadrons had a difference of 10%. This larger relative difference is easily understood from the signal regions of the two mass hypotheses. A higher R-hadron mass results in the signal being placed at a region with lower background statistics, and thus a higher uncertainty on the generated background. For simplicity the systematic uncertainty on the estimated background will be assumed to be 10% for all mass hypotheses as a conservative estimate.

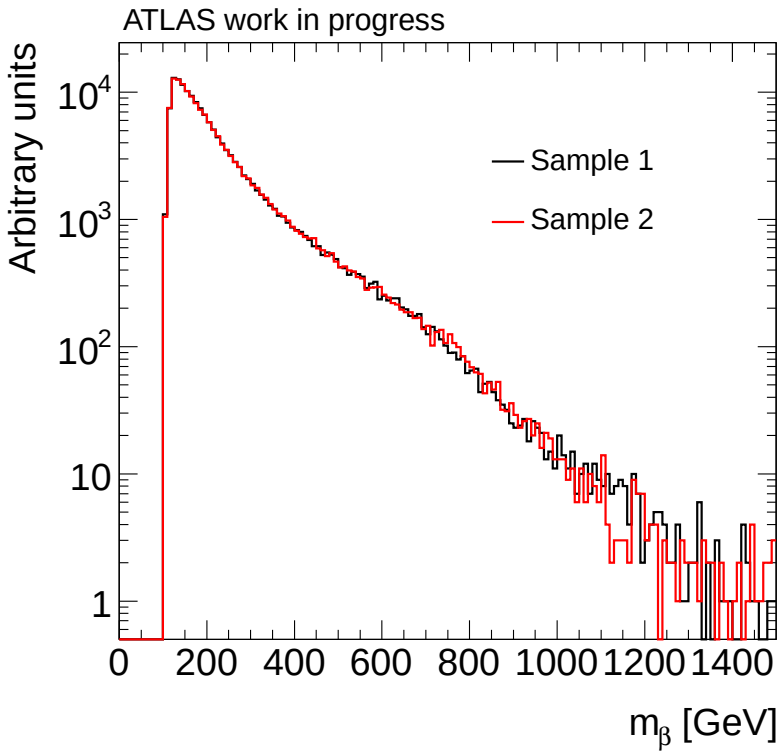

Figure 10.3: Distribution of m_β for 300000 generated background events in the case of 1000 GeV R-hadrons, randomly split into two samples of equal size. The variation in the high mass region between the samples gives an estimate of the systematic uncertainty on the amount of background.

10.3 Combination of errors

All systematic errors are assumed to be uncorrelated, which enables a quadratic error combination according to

$$\sigma_{\text{tot}}^{\text{syst}} = \sqrt{\sum_i (\sigma_i^{\text{syst}})^2}. \tag{10.3.1}$$

The errors contributing to the uncertainty on the theoretical production cross section, the experimentally obtained signal efficiency and the experimental background estimation have individual $\sum_i$. Table 10.2 gives a summary of all systematic uncertainties.

Description	Size
Total theoretical uncertainty on signal cross section	15-30%
Renormalisation and factorisation scale	$\geq$15%
PDF variations*	5%
Total experimental uncertainty on signal efficiency	9.6%
Luminosity	3.7%
Initial and final state radiation*	7.4%
MET trigger efficiency*	4%
Pre-selection efficiency	0.9%
Pileup conditions	2.1%
Momentum resolution*	1.3%
Calo β calibration with muons/jets	1%
Total experimental uncertainty on background estimate	10%

Table 10.2: List of all considered systematic uncertainties. The value of the uncertainty due to renormalisation and factorisation scale varies with the mass hypothesis, but has a value of at least 15% for all mass points. Values taken from the collaborative R-hadron search [43] that have not been evaluated directly by the author are marked with a *.

11 Results

The search for R-hadrons is based on a statistical analysis. By choosing the part of the available parameter space in which R-hadrons are expected to reside, a comparison can be made between the observed number of events from data in this region and the expected backround. If a large disparity is observed between these numbers, it can be assumed that a new particle exists with properties consistent with those of R-hadrons. If the observed number does not deviate from the expected background, a less powerful result can be obtained by estimating the maximum production cross section of R-hadrons allowed by the data.

11.1 Significance

At the most basic level the desired limit is the result of a counting experiment. For each R-hadron mass hypothesis the number of observed events in data that pass the selection cuts defined in section 8.1 and 8.2 is compared to the expected background. The observed number is event-based and is necessarily an integer value. On the other hand, the expected background can take any numeric value, since the background has been generated as an arbitrary (but statistically significant) number of random samplings of the background p, β and $\beta\gamma$ distributions, which is then rescaled to fit the observed data in the sideband region.

In order to compare the observed number of events with expected background, an expression for the probability of the observed number under the background-only hypothesis (null hypothesis) is required. The experiment operates at the low-statistics limit and the numbers can be assumed to follow Poisson distributions. This means that even if the observed number of events exceed the expected background, it is still possible to have a large probability that the observation can be described by background alone. To quantify this, the statistical significance is given as the probability that the expected number of background events b fluctuates to the observed number n_{obs} or higher, and can be written as [39]

$$\alpha = \sum_{i=n_{\text{obs}}}^{\infty} \frac{b^i e^{-b}}{i!}. \tag{11.1.1}$$

In the limit $\alpha \to 0$ it is no longer possible for the background-only hypothesis to describe the data. The level of incompatibility with, or deviation from, the background model is customarily stated in terms of the corresponding number of standard deviations in a

one-tailed Gaussian. A 3σ effect can be considered *evidence* of new physics, while a 5σ deviation is accepted as a *discovery*.

11.2 Limit setting

Considering the number of candidate events and the expected background summarised in table 11.1 no evidence of a signal is observed at any of the investigated mass hypotheses. The next step is to continue to set limits on the production cross section of R-hadrons at each mass. Assuming a particular theoretical model for the production of R-hadrons it is then possible to quote a mass exclusion limit, below which R-hadrons of that model can be ruled out at a certain Bayesian confidence level. If a certain hypothesis has significance α, i.e. the probability of getting some particular measurement under that hypothesis is α, then using Bayesian reasoning one can state that the hypothesis is ruled out at a confidence level of $1 - \alpha$.

As a first step, the upper limit on the number of signal events should be found. Given the observation of n_{obs} events, this states the maximum number of signal events that could be present in addition to the expected background at some confidence level using the signal+background hypothesis. In other words, the number of signal events s should be maximised in the following expression while assuming a background b and demanding a specific significance α:

$$\text{CL}_{s+b} = \alpha = \sum_{i=0}^{n_{\text{obs}}} e^{-(s+b)} \frac{(s+b)^i}{i!}. \tag{11.2.1}$$

It is customary to fix the confidence level at 95%, which means that the probability of getting s or more signal events is $\alpha = 5\%$. A potentially important warning should follow the use of equation 11.2.1, since it does not take into account fluctuations of the background. To circumvent this problem, statisticians in the particle physics field recommend using the CL_s method [40, 41]. It defines a likelihood ratio between the signal+background hypothesis and the background-only hypothesis

$$\text{CL}_s = \frac{\text{CL}_{s+b}}{\text{CL}_b} = \frac{\sum_{i=0}^{n_{\text{obs}}} \frac{(s+b)^i}{i!} e^{-(s+b)}}{\sum_{i=0}^{n_{\text{obs}}} \frac{b^i}{i!} e^{-b}}, \tag{11.2.2}$$

which removes the effect of background fluctuations.

One more complication is needed to account for the systematic uncertainties treated in chapter 10. The respective errors should be applied to s and b in equation 11.2.2, and this is done by performing a smearing of both numbers using Gaussian distributions with the appropriate widths. By performing N pseudo-experiments (for large N), each with new smearing values, the final signal limit can be found by maximising s_j for each pseudo-experiment j to find $s_{\text{up}} = \frac{1}{N} \sum_{j=1}^{N} s_j$. Calculating the smearing of s_j and b_j with Gaussian distributions having widths in percent corresponding to the final systematic uncertainties given in table 10.2, and denoting each particular smearing factor as ρ_{s_j} and ρ_{b_j}, each s_j should be maximised using

$$\mathrm{CL}_s = \frac{\sum_{i=0}^{n_{\mathrm{obs}}} \frac{\left(s_j(1+\rho_{s_j})+b(1+\rho_{b_j})\right)^i}{i!} e^{-\left(s_j(1+\rho_{s_j})+b(1+\rho_{b_j})\right)}}{\sum_{i=0}^{n_{\mathrm{obs}}} \frac{\left(b(1+\rho_{b_j})\right)^i}{i!} e^{-b(1+\rho_{b_j})}} \tag{11.2.3}$$

Once s_{up} has been found, the observed upper limit on the production cross section $\sigma_{\tilde{g}}$ can be calculated as

$$\sigma_{\tilde{g}} = \frac{s_{\mathrm{up}}}{A\varepsilon\mathcal{L}}, \tag{11.2.4}$$

where A is the geometric detector acceptance, ε is the R-hadron selection efficiency and $\mathcal{L}$ is the integrated luminosity for which s_{up} has been maximised. The product $A\varepsilon$ is found using the simulated R-hadron signal samples. These are run through the same analysis as the collected ATLAS data. The fraction of events that pass all selection cuts is compared to the number of generated events at each mass hypothesis *after* performing pileup reweighting and weighting each MC signal event by the relative production cross section of gg fusion and $q\bar{q}$ annihilation as described in table 6.2.

Expected limit

To compare the obtained cross section limits to what would be expected assuming the background-only hypothesis, another maximisation is performed [46]. A large number of pseudo-experiments are generated under the null hypothesis by assuming a Poisson distribution for the number of detected events, with a mean corresponding to the estimated background. Plugging in this number of 'observed' events for each pseudo-experiment into equation 11.2.3 gives a distribution of optimised signal values s_{up} at 95% CL.

The median of the s_{up} distribution for each mass hypothesis is then quoted as the expected limit on the R-hadron signal, which is again converted to a limit on the production cross section through equation 11.2.4. To obtain the ± 1 and ± 2 σ uncertainty bands, the distribution is integrated iteratively with one end of the interval at the median to find the $\pm 1\sigma$ values at which $\sim 68\%$ of the data above/below the median is included, and the $\pm 2\sigma$ values at which the inclusion reaches $\sim 95\%$.

An important comment needs to be made about the -1σ and -2σ uncertainty bands when reaching the zero-backround regime. The upper one-sided 95% limit for the mean of a Poisson variable is 3.0 (see [1, p. 359] and appendix A for an illustration). The only way to get values of the optimised signal below this threshold is through the smearing done by the systematic uncertainty on the signal. The justification of these lower bands can therefore be discussed, but they are included here for completeness.

$m_{\tilde{g}}$ [GeV]	Signal eff. [%]	Obs. data [events]	Exp. bkg. [events]	Exp. limit [fb]	$+2\sigma$ [fb]	-2σ [fb]	Obs. limit [fb]
200	3.9	334	279.9	189.6	522.3	73.8	482.9
300	4.4	161	128.9	115.6	284.7	52.1	269.0
400	4.6	28	30.0	59.2	120.8	28.3	52.9
500	6.9	15	13.8	28.1	61.3	14.4	32.1
600	7.6	8	8.1	20.7	42.4	10.7	21.2
700	8.7	4	3.9	14.1	27.5	7.9	14.8
800	7.7	2	1.3	11.5	23.5	7.1	14.7
900	8.9	0	0.6	8.9	17.0	5.9	7.3
1000	8.4	0	0.5	8.5	17.5	6.3	7.7
1100	9.1	0	0.5	8.0	15.4	5.8	7.2
1200	8.6	0	0.2	7.7	14.1	6.0	7.5
1300	7.5	0	0.2	8.7	15.3	6.9	8.6
1400	8.7	0	0.1	7.6	13.2	5.9	7.5
1500	8.6	0	0.0	7.5	10.7	5.9	7.6

Table 11.1: Search results for all investigated R-hadron mass hypotheses. Included are the signal efficiency, expected background, events observed in data, observed limit and expected limit with $\pm 2\sigma$ bands.

11.3 Mass exclusion limit

The final limit plot is shown in figure 11.1 together with the theoretically predicted gluino production cross section found from Prospino. Within the lower 1σ value of the theoretical uncertainty on the production cross section, the 95% CL_s mass exclusion limit for gluino-based R-hadrons is found to be

$$m_{\tilde{g}} > 981 \text{ GeV}.$$

The official 2012 ATLAS R-hadron search done in part by the local group at NBI was able to include the Muon Spectrometer to achieve a better estimate on β by combining calorimeter and MS time measurements. The result of this full detector search can be seen in figure 11.2.

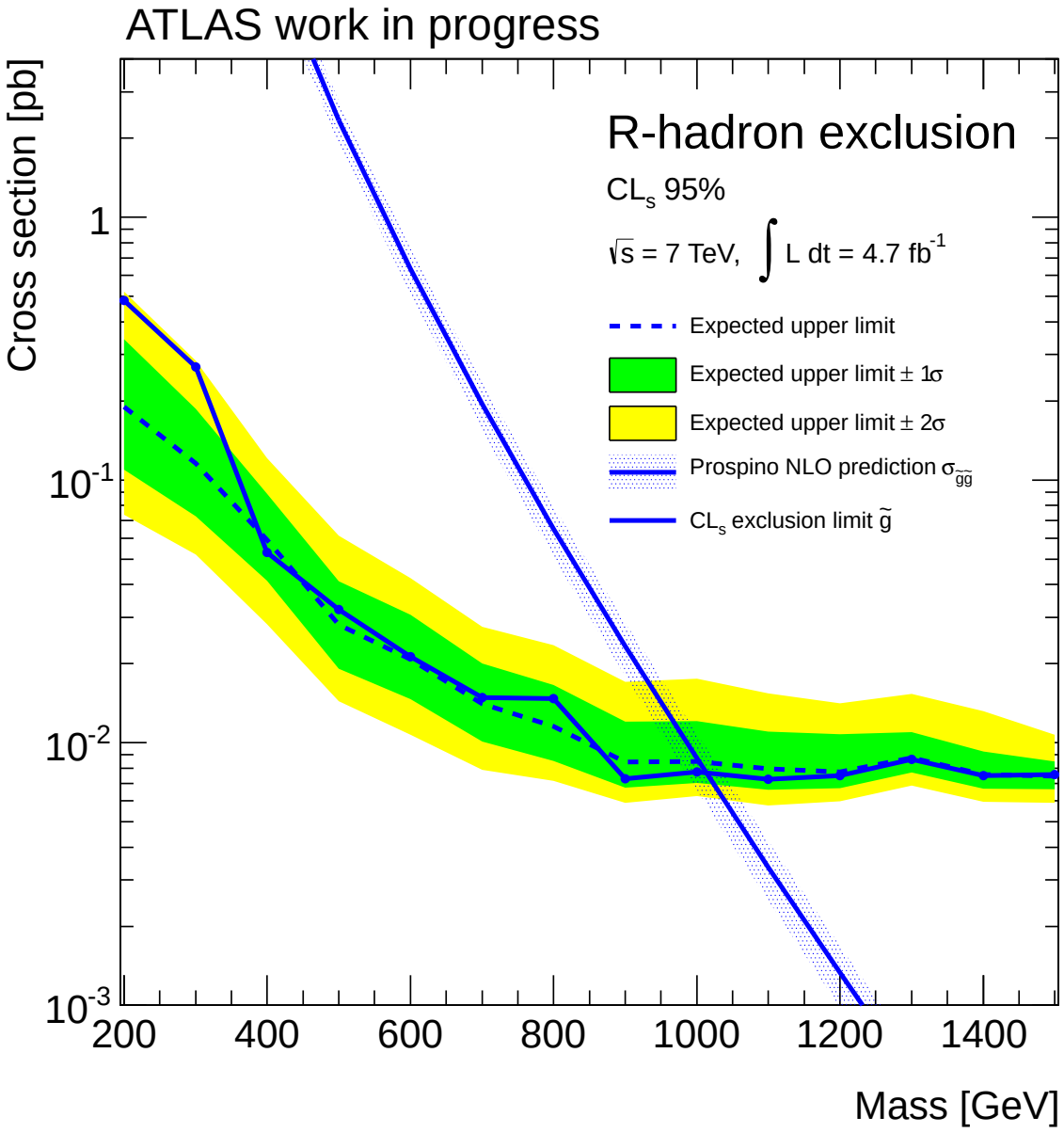

Figure 11.1: The final limit on the gluino production cross section for each mass hypothesis. Both the observed and expected limit are shown, as well as the predicted cross section from Prospino.

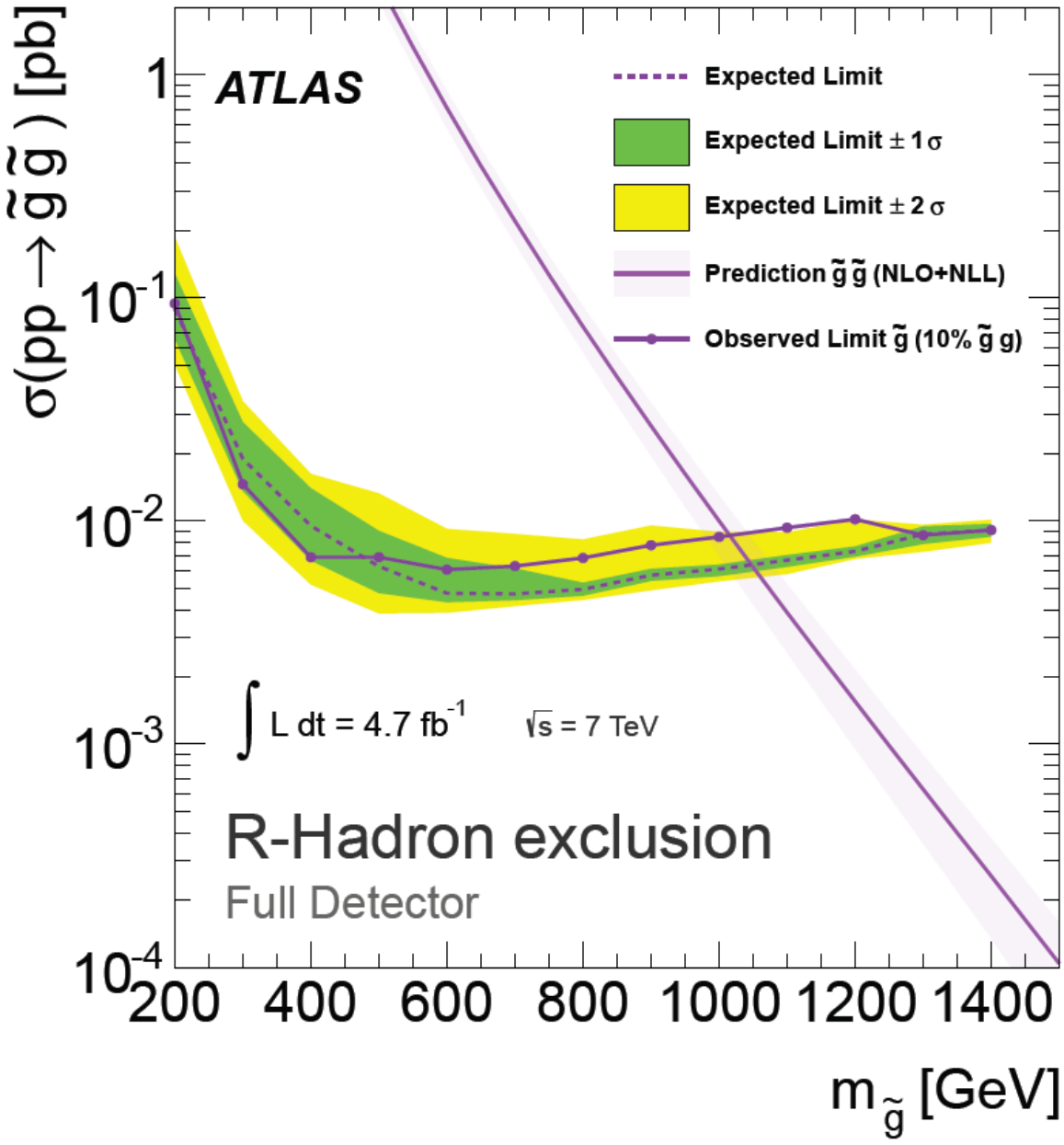

Figure 11.2: Limit plot of gluino production cross sections taken from the collaborative effort [43].

12 A preliminary study of R-hadron identification by charge alteration

As mentioned in section 3.3 an R-hadron could exchange quarks in its light quark system and thereby alter its electric charge. In the following, an attempt is made to develop a method of discriminating R-hadrons with a non-constant charge during their passage through the detector. Two possible discrimination variables are constructed and evaluated, and finally they are employed in combination.

Due to the small size of the signal samples it is preferable to avoid applying any trigger cut. To make sure that the MET trigger does not bias the p_T spectrum of the R-hadrons, each track in the untriggered distribution is weighted using the difference between the two distributions at the given value of p_T.

12.1 Discrimination by momentum

Separate momentum measurements are available from the ID and MS. In the track reconstruction of combined tracks (having hits in both detector parts that are combined) a unit charge is assumed. If an R-hadron is produced and traverses the ID with unit charge which gets altered to the opposite sign before reaching the MS, the product of the particle's charge and momentum qp will also change sign, and the ratio $(qp)_{\mathrm{ID}}/(qp)_{\mathrm{MS}}$ is expected to have a negative value close to unity. A charge alteration from ± 1 to ± 2 (or the reverse) will change the curvature of the track in the MS compared to the ID, which will result in p_{MS} being reconstructed as half (twice) the size of p_{ID}. Hence we expect $(qp)_{\mathrm{ID}}/(qp)_{\mathrm{MS}} \simeq \pm\frac{1}{2}$, or ± 2 in the reverse case. This inconsistency between the momentum measurements may provide discrimination power.

Figure 12.1 shows the ratio between the ID and MS momentum measurements for R-hadrons and data. If the MC truth momentum is used in place of the reconstructed ID momentum, a clear peak at $p_{\mathrm{MS}}/p_{\mathrm{truth}} = \frac{1}{2}$ is seen. This confirms that the MC interaction model includes the possibility of charge alteration through the detector. However, the reconstructed data does not show such a clear peak; the uncertainty on momentum is the main factor for the potential of identifying charge alteration in the detector. As the relative momentum error increases rapidly with the momentum and therefore the mass of the SMP, the method will be most effective at lower masses. However, only R-hadrons with masses

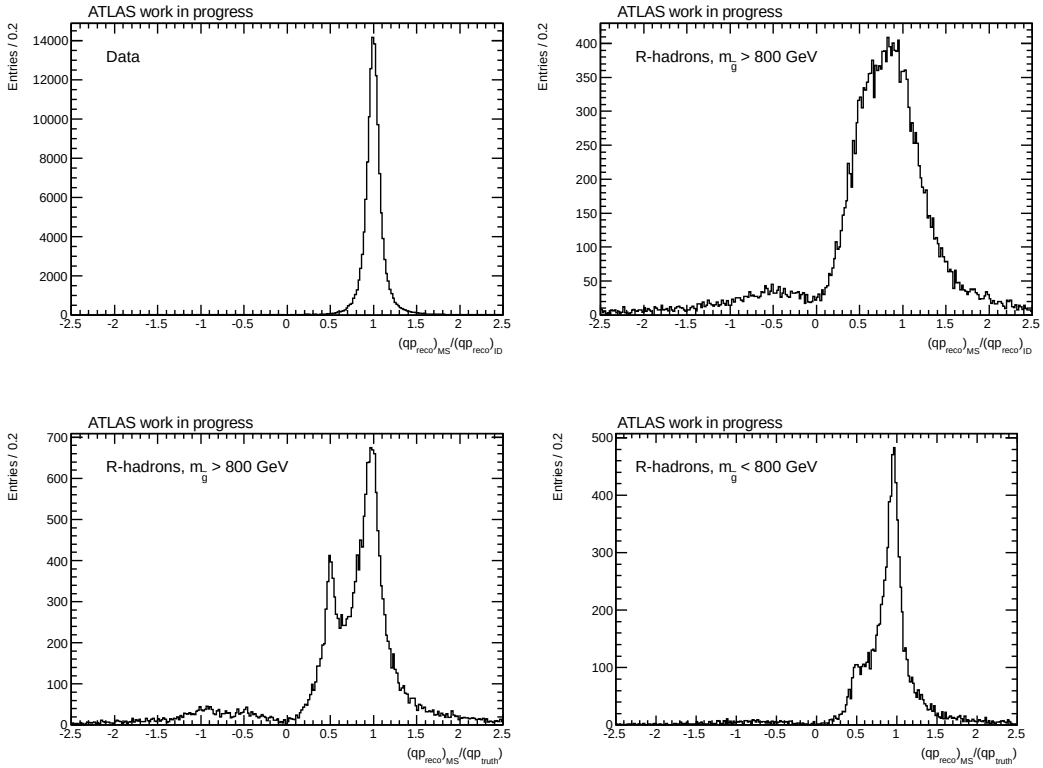

Figure 12.1: Ratio of the momentum measurements in the Muon Spectrometer and the Inner Detector. By exploiting the truth momentum in the signal samples (bottom) a clear peak at 1/2 is observed. This peak is most prominent for high R-hadron masses. The reconstructed momentum smears this peak considerably (top right).

of 800 GeV or above are found to undergo this charge alteration in significant numbers[1]. This observation may render the method less powerful in the search for R-hadrons and other SMPs with exclusion limits already in the TeV range. Nevertheless, roughly 10% of the R-hadrons with masses of 800 GeV or above undergo this charge alteration making it a potentially interesting handle on R-hadron detection.

12.2 Discrimination by ionization (dE/dx)

When particles pass through the active layers in e.g. the calorimeters they can undergo multiple scattering or have different incident angles, which leads to a correction of the otherwise Gaussian shape of the energy depositions. The values will follow a Landau distribution with a peak at the most probable value (MPV) and with a tail towards higher values. The tails of the dE/dx distributions are generally longer for R-hadrons compared to SM particles, but the most probable values (MPVs) are in good agreement in the calorimeter layers. When performing a search for R-hadrons it is not known which particles, if any, are R-hadrons, and hence the same MPVs must be used for all detected particles. These

[1]This is found strange, since no dependence of the interactions on R-hadron mass is expected

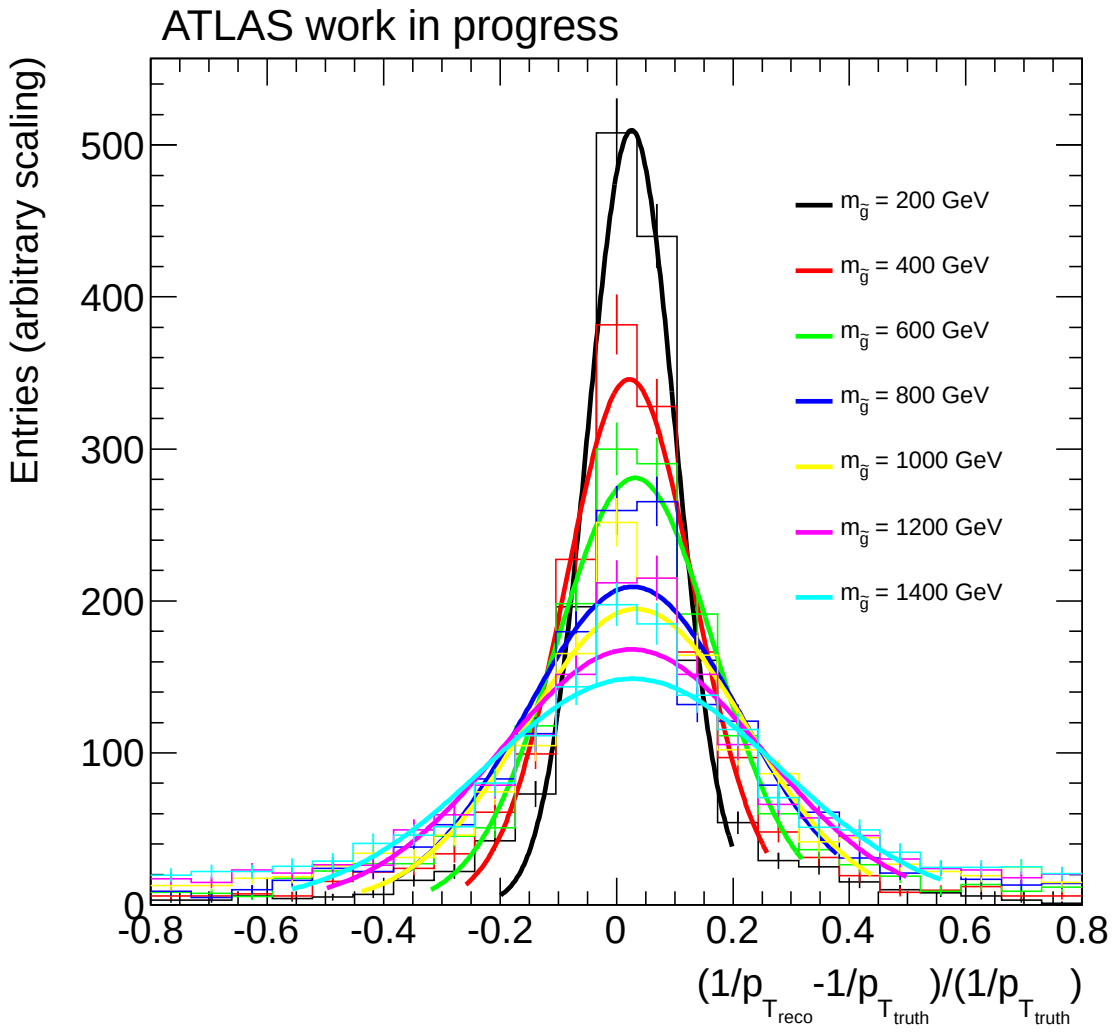

Figure 12.2: Momentum resolution of R-hadrons measured as the difference between reconstructed and truth values. A Gaussian fit is applied to each distribution.

are obtained from data. The dE/dx distributions for $Z \to \mu\mu$ muons are shown for each calorimeter layer in figure 12.4 fitted by a Landau folded with a Gaussian. Already in the D3PD's the corresponding EM layers in barrel and endcap have been combined (presampler with presampler etc.), and the numbering scheme is given in table 12.1.

It has not been possible to obtain dE/dx values from the muon spectrometer, although they exist by now. Thus the available energy loss measurements come from the Pixel detector, the TRT and the calorimeters. The TRT is only accurate for energy losses less than ~ 4 MIPs, since the measurement saturates above this value and no longer gives a correct estimate. Measurements from the TRT are therefore not included. In figure 12.3 is shown the dE/dx distributions in the Pixel detector for muons and R-hadrons. The relatively large difference in the position of the MPV makes it unfit for the method described in the following. Consequently, only measurements from the calorimeter layers are utilised.

Number	Layer	μ	σ
1	EM presampler	1.76	0.47
2	EM layer 1	0.58	0.14
3	EM layer 2	0.53	0.18
4	EM layer 3	0.72	0.31
5	Tile layer 1	0.98	0.35
6	Tile layer 2	1.14	0.28
7	Tile layer 3	1.14	0.31
8	HEC layer 1	3.25	0.56
9	HEC layer 2	1.87	0.39
10	HEC layer 3	3.08	0.72
11	HEC layer 4	3.07	0.69

Table 12.1: Numbering scheme for the calorimeter layer dE/dx values. The EMB and EMEC have been combined. The MPV (μ) and HWHM (σ) is given for $Z \to \mu\mu$ data for each layer.

Development of a discrimination variable

The purpose of this section is to arrive at a variable that combines the information stored in all calorimeter layers traversed by a particle. As demonstrated in section 12.1 the only abundantly observed charge transition is $1 \to 2$, and by consulting equation 3.2.1 it is seen that a doubling of a particle's charge results in a fourfold increase in ionisation. By comparing the energy depositions in each calorimeter layer it should in principle be possible to observe a sudden change towards higher values if the charge of the particle was altered.

A potentially more reliable way to quantify this than simply looking for a single layer where the energy loss increases would be to perform a minimisation of the χ^2 expression

$$\chi^2 = \sum_i \frac{(dE/dx_i - \mu_i)^2}{\sigma_i^2} + \sum_o \frac{(dE/dx_o - 4\mu_o)^2}{(2\sigma_o)^2}, \tag{12.2.1}$$

by defining $\sum_i$ to run over all inner layers until the charge alteration has taken place and $\sum_o$ to run over the remaining outer layers. μ_j is the MPV of the dE/dx distribution (for $Z \to \mu\mu$ data) in the j'th layer, while σ_j is the HWHM of the distribution. By iteratively calculating the χ^2 value for all possible divisions of the layers into inner and outer groups, the most probable position of the particle at the time of charge alteration can be found while taking into account the widths of the distributions in each layer. In accordance with equation 3.2.1 the means of the outer group of layers have been multiplied by four. The dE/dx uncertainty is expected to follow the expression [2]

$$\frac{\sigma(E)}{E} = \frac{a}{\sqrt{E}} \oplus b, \tag{12.2.2}$$

where a is the stochastic term and b a constant term. At most energies the stochastic term will dominate, so the constant term will be neglected. A fourfold increase in energy deposition will then double the error according to $\sigma(4E) = a\sqrt{4E} = 2\sigma(E)$.

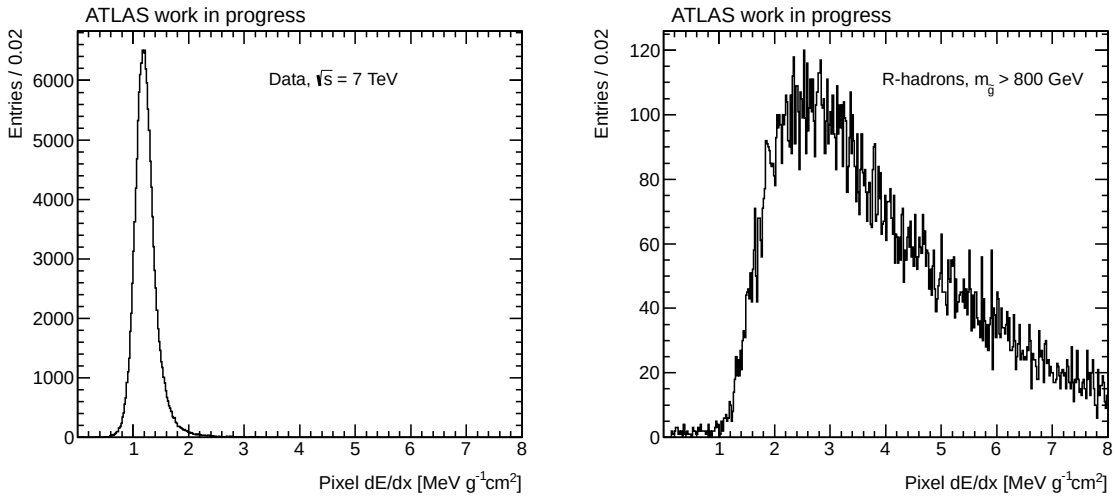

Figure 12.3: Distributions of dE/dx in the Pixel detector for data (left) and heavy R-hadrons (right). The large discrepancy makes the measurements unfit for inclusion in the dE/dx-based charge discrimination.

A complicating factor that needs to be taken into account before performing the minimisation is the fact that the mean ionization changes with $\beta\gamma$ according to equation 3.2.1. This is not a problem for muons which are produced with highly relativistic speeds, but R-hadrons occupy a much larger interval of $\beta\gamma$ values. A correction factor as a function of $\beta\gamma$ is introduced to counter this problem. During the author's studies for a statistics Master course, it was found that the dE/dx rise towards lower $\beta\gamma$ values can be adequately described by an exponential function [51]. A function of the form

$$f(\beta\gamma) = c_0 + c_1 \exp(c_2 x) \tag{12.2.3}$$

is therefore matched to the lower dE/dx band corresponding to the singly charged R-hadrons in the EM calorimeter layer 1 (see figure 12.6). While the means differ in each layer, the characteristics of the rise are generally the same. The value of $f(\beta\gamma)/c_0$ is then used as a multiplicative correction factor for the signal samples.

When the minimisation has been performed and layers have been grouped, the values of dE/dx_{inner} and dE/dx_{outer} are found as the mean values in each group. For this mean to be meaningful however, the individual values need to be shifted according to μ in each layer to make the values compatible. The final discrimination variable is then the ratio $(dE/dx_{\text{outer}})/(dE/dx_{\text{inner}})$. For SM particles and the subset of R-hadrons that do not undergo charge alteration a value of 1 is expected, while theoretically the doubly charged R-hadrons should have a ratio of 4. Examples of dE/dx measurements are shown in figure 12.8 collected into an inner and outer group through the minimisation of 12.2.1. The left plot shows a track with a successful χ^2 minimisation yielding a dE/dx ratio close to 4. The right plot shows data for a track with the typical problem of too few high dE/dx measurements and with a ratio considerably less than 4. The generally low number of measurements in the outer layers is a potential explanation for the absense of a clear

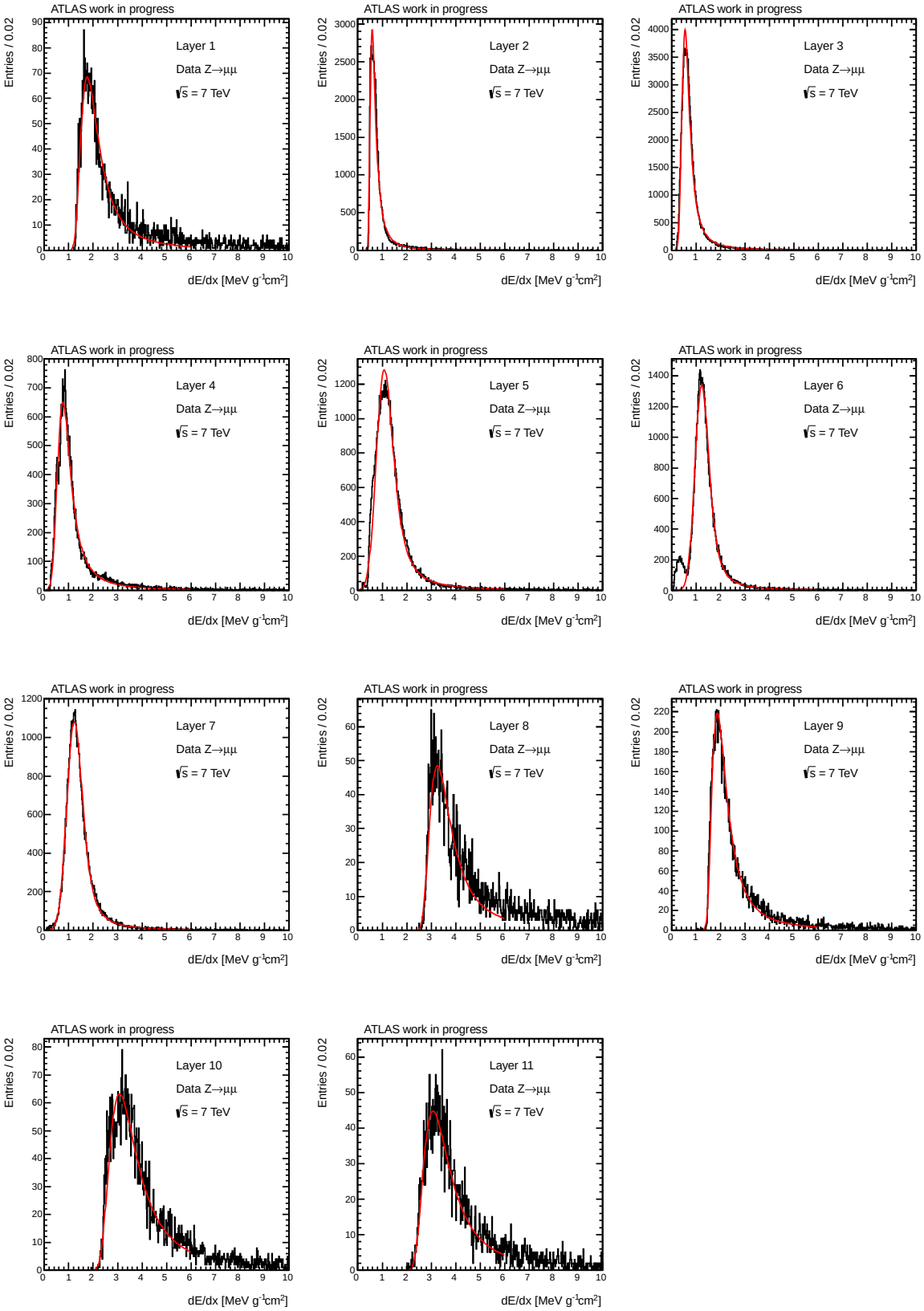

Figure 12.4: Distributions of dE/dx in each calorimeter layer fitted to a Landau function convoluted with a Gaussian. The distributions are obtained from data period D.

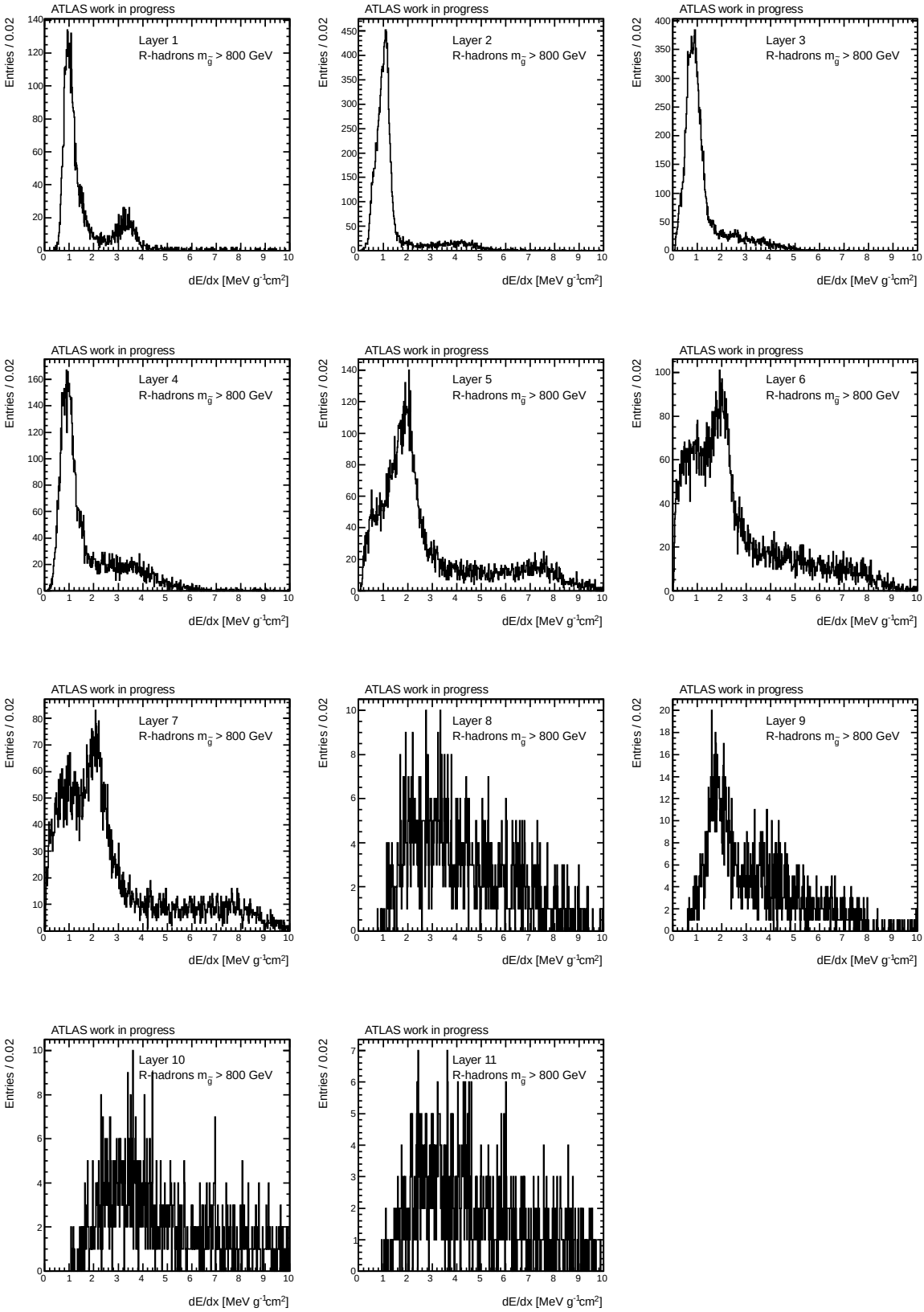

Figure 12.5: Distributions of dE/dx in each calorimeter layer for R-hadrons corrected as a function of $\beta\gamma$. Some layers such as 1, 2, 4 and 5 show an extra peak at ~ 4 times the value of the MPV of the main peak, or a tail extending out to this value.

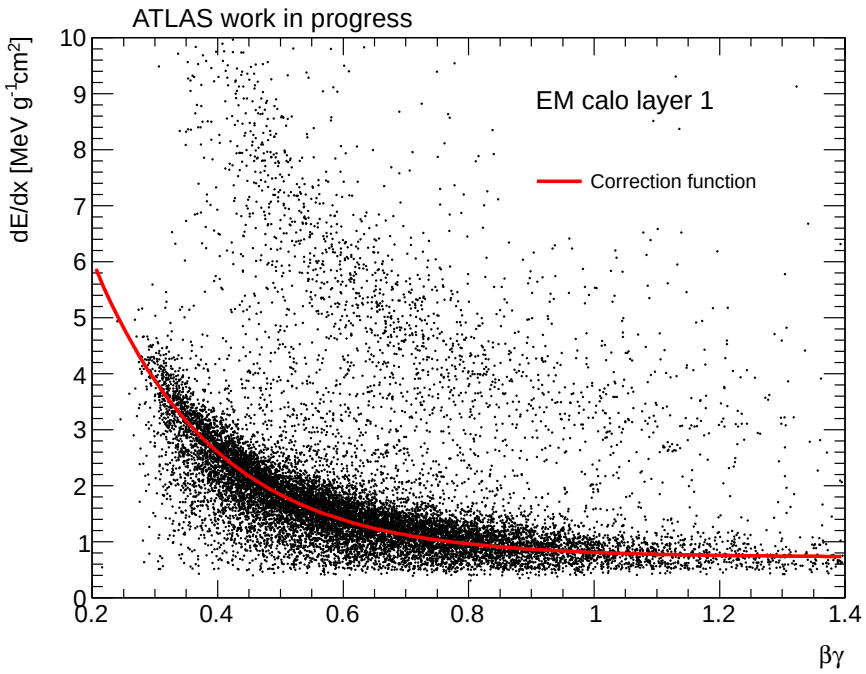

Figure 12.6: Exponential fit to the dE/dx rise at low $\beta\gamma$ for R-hadrons in the EM calorimeter layer 1. Notice also the visible band for the doubly charged particles at 4 times the ionization.

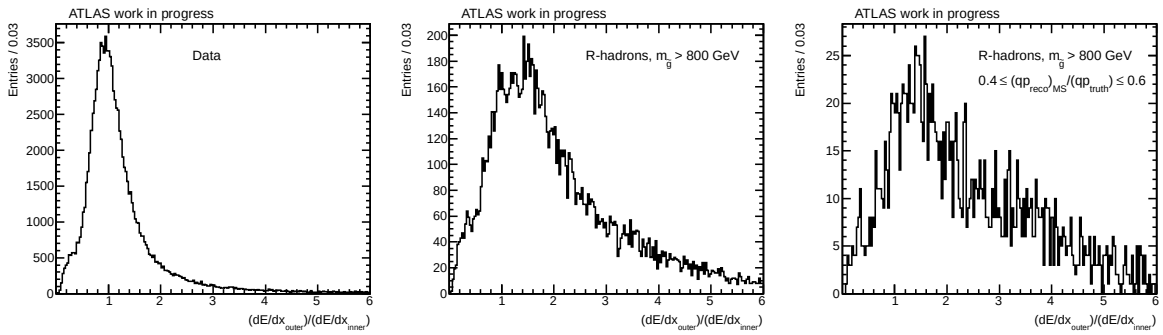

Figure 12.7: dE/dx ratio found by comparing the means of the inner and outer grouping of calorimeter layers. The subset of values for R-hadrons at the $(qp)_{\mathrm{ID}}/(qp)_{\mathrm{MS}} = 1/2$ peak show a slight bias towards higher values.

peak at or close to four in the R-hadron plots in figure 12.7. The figure shows the dE/dx ratio for $Z \to \mu\mu$ muons, heavy R-hadrons and finally the subset of the R-hadrons having $0.4 \leq (qp)_{\mathrm{ID}}/(qp)_{\mathrm{MS}} \leq 0.6$. No clear peak is observed at a value of 4, but a slight bias towards higher values is observed when restricting the value of the momentum ratio.

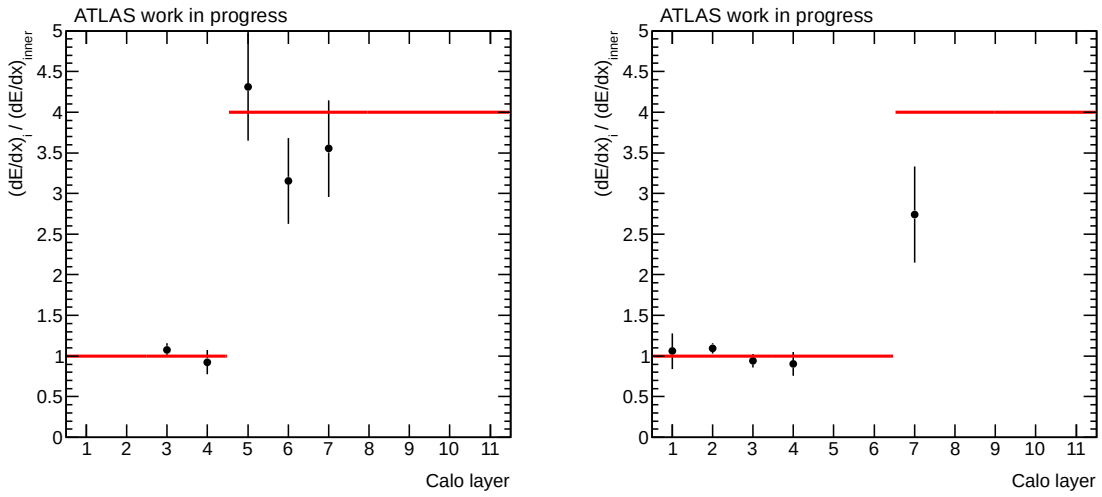

Figure 12.8: Examples of dE/dx measurements in each calorimeter layer for two tracks. The values are normalised to the estimated value of dE/dx_{inner}. The red lines show the optimal means of the ionization values in the cells before/after the charge has changed. Both tracks are from the subset having $0.4 \leq (qp_{\text{reco}})_{\text{MS}}/(qp_{\text{truth}}) \leq 0.6$.

12.3 Results

Slight variations in both discrimination variables are observed between data and signal samples promising a non-negligible discrimination power. An improved discrimination cut may be found by viewing the quantities together. A 2D plot of $S/\sqrt{S+B}$ with S being signal and B background is shown in figure 12.10. A proposed cut barrier is inserted that exploits the 2D shape of the distribution. The dE/dx ratio adds little to the discrimination, and the largest problems described above are the generally low number of good measurements forming the basis for the inner/outer layer division, and the less than optimal compatibility between the dE/dx distributions in each layer when comparing data to signal samples, even after correcting for $\beta\gamma$. This correction is not accurate for all tracks, as a small portion of data points in figure 12.6 are seen not to follow the rise at low $\beta\gamma$. The presampler has good precision, and figure 12.9 shows that a larger fraction of the tracks with momentum ratio 0.5 have a large value of dE/dx. This effect is only visible in a few layers, and the χ^2 optimisation has very little to work with in the outer layers.

The studies performed above are a proof-of-concept but can in no way be considered mature enough to be included in the search. More work needs to be done if the Pixel detector is to be included, and it is possible that the dE/dx ratio can be optimised further. More potent results are also expected if the muon system is added, since the probability of charge alteration increases with the amount of material traversed. The $\beta\gamma$ correction may be improved by studying the actual length of material traversed in each calorimeter layer depending on the incident angle. The largest factor subtracting from the usefulness of the method is the low statistics in the outer calorimeter layers and the generally low quality of these measurements. Even the hypothesis of only one charge alteration through

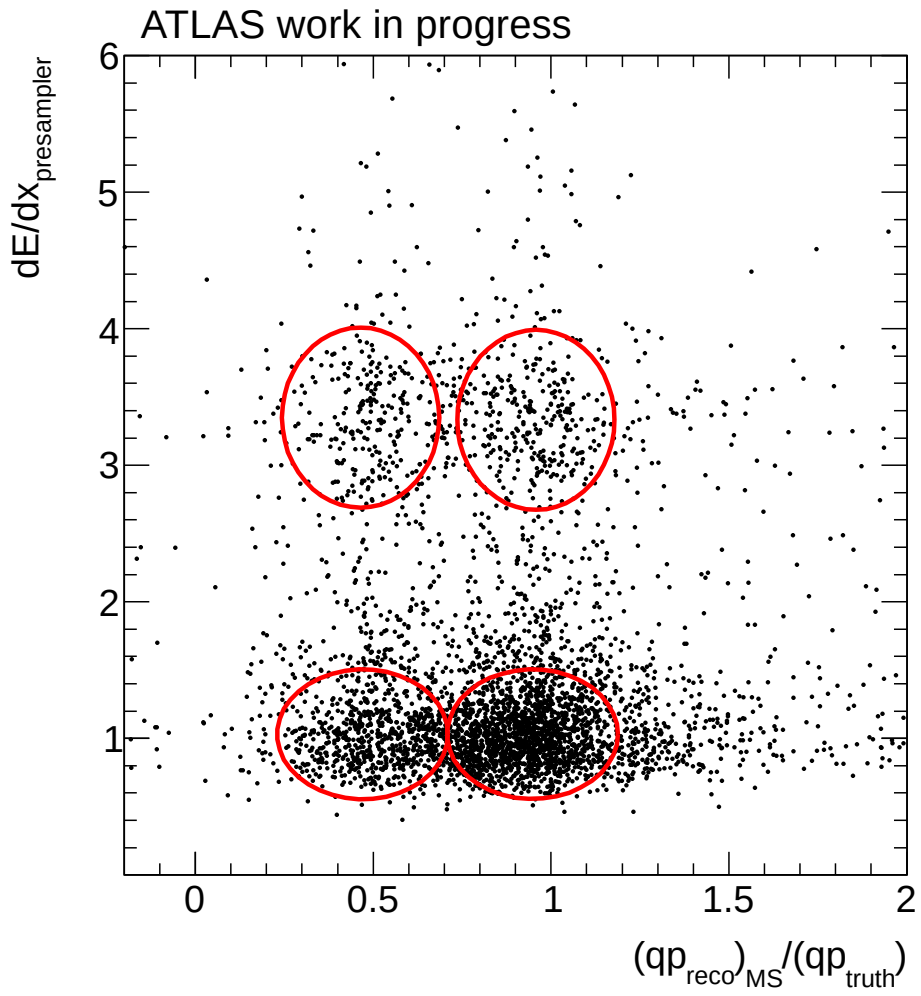

Figure 12.9: 2D plot showing the $\beta\gamma$ corrected dE/dx measurements in the EM presampler vs. the momentum ratio of MS and truth. The four regions of interest have been marked by ellipses. The ratio of events in the high and low dE/dx region for momentum ratio ~ 0.5 is 0.39, while the same ratio for momentum ratio ~ 1.0 is 0.18.

the calorimeters is questionable due to work done in [52] showing non-negligible transition probabilities between charge states from each successive calorimeter layer to the next. A much more promising (and simpler) analysis would be to ignore the calorimeters and only investigate the dE/dx measurements from ID and MS.

An alternative approach to the dE/dx ratio described in more detail in [52] is to divide the $(\beta\gamma, dE/dx)$ distribution into geometric regions corresponding to the singly and doubly charged bands found in each layer. Discrimination of particles with charge 2 could then be achieved if a sufficient number of layers showed data in the appropriate region.

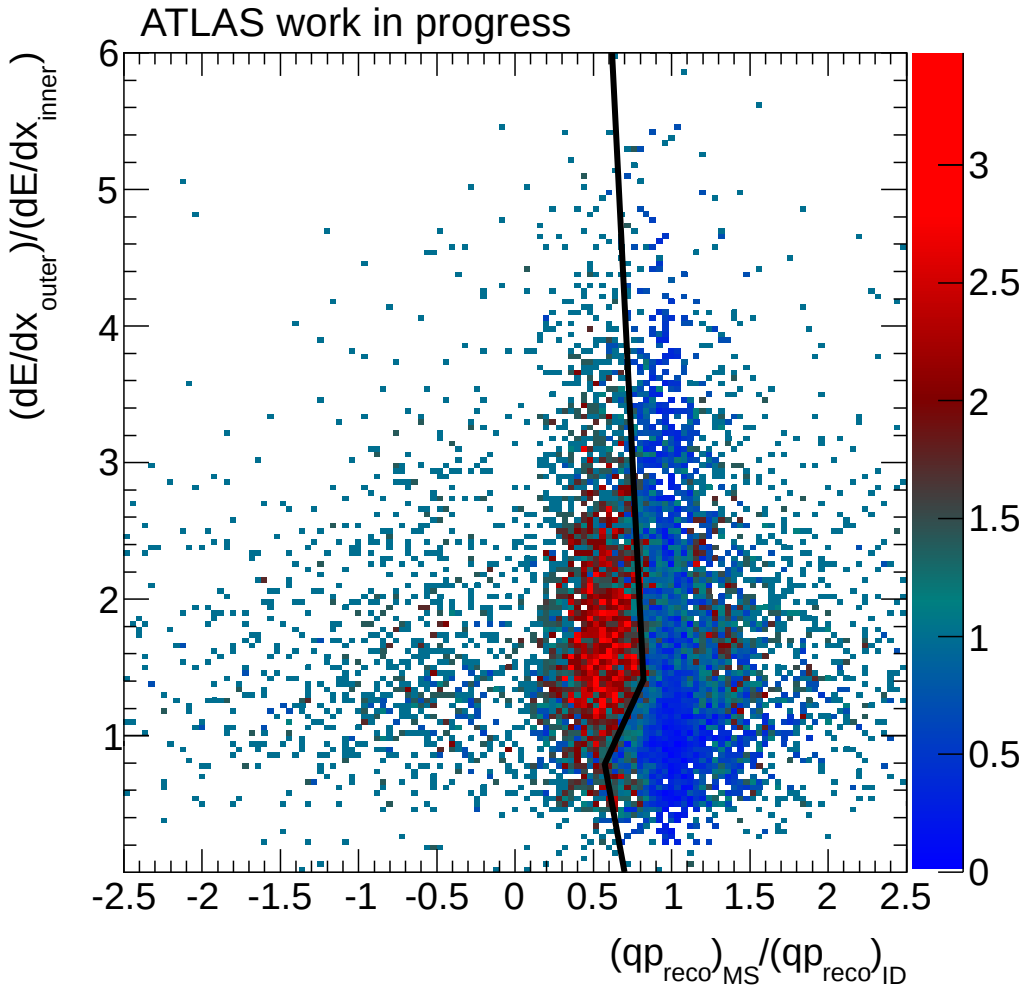

Figure 12.10: 2D plot showing the combined discrimination potential of both variables combined in the form of $S/\sqrt{S+B}$. A proposed cut barrier is given by the black line. The algorithm for finding the dE/dx ratio is far from optimal due to low statistics and large errors on measurements from the outer calorimeter layers. No concentration of signal is seen at a dE/dx ratio of four. Instead a smeared out distribution extends to ~ 3.

13 Conclusion

In a search for R-hadrons one of the most potent discriminators is the particle speed β, which is expected to be considerably lower than for any Standard Model particles due to the large mass of the R-hadrons. In this thesis a discriminator based on β was developed from the time-of-flight measurement capabilities of the ATLAS calorimeters. The values were calibrated using a sample of $Z \to \mu\mu$ muons in both data and MC, and the result was compared to a second calibration done in parallel using jets, the conclusion of which was that the type of relativistic particles used for the calibration has a negligible impact. Consequently, future analyses can benefit from a calibration using inclusive muons, enabling a drastic increase in the number of calibration constants, if beneficial.

The reconstructed β values from each calorimeter layer were subsequently weighted by their error to form a combined best estimate from the calorimeter system, and a final error correction was performed using pull distributions on the data from the calorimeters as well as data from the MDT and RPC technologies in the muon system supplied by the NBI group.

The β discriminator was used as part of a search for gluino-based R-hadrons. Furthermore it made use of $\beta\gamma$ estimates found from Pixel dE/dx measurements and the mass estimates m_β and $m_{\beta\gamma}$. Using the 2011 ATLAS data set comprising 4.7 fb^{-1} of data collected at a center-of-mass energy of $\sqrt{s} = 7$ TeV, the search placed upper limits on the production cross sections of R-hadrons with masses ranging from 200 MeV to 1.5 TeV. Comparing the upper limits on production cross sections with the theoretically predicted values at each mass point found from Prospino gave a competitive lower limit on the gluino mass of 981 GeV.

The official 2012 ATLAS R-hadron and slepton search [43], in which the developed β calibration was also employed, was able to set limits of 985 GeV (muon agnostic search) and 989 GeV (full detector search). Future searches, after the imminent long shutdown, done at $\sqrt{s} = 14$ TeV and at the LHC's design luminosity will be able to extend the limit setting well into the TeV range.

A preliminary study was done on the potential of discrimination of R-hadrons that have their charges altered during their passage through the detector. While some discrimination power is present for both the ratio of momentum measurements in ID and MS as well as the dE/dx measurements in the calorimeters, the technique needs further development to be a viable option.

14 Outlook

During the period of working on this thesis many ideas regarding the refinement of β measurements materialised, but were not included in the analysis. They were either too time consuming to justify the necessary effort to include them, or the 2011 data set simply did not have enough statistics to make them feasible.

One straightforward development would be to improve the granularity of the timing calibration. Enough statistics is available in both the 2011 and 2012 ATLAS data to drastically increase the number of calibration constants using inclusive muons, even to the point of performing the calibration on cell level, giving on the order of 10^5 constants. In the 2011 analysis the RPC timing calibration was performed using roughly 12 calibration constants. This has been increased by several orders of magnitude in 2012 [53]. This gives a twice as precise β measurement, which could further improve the R-hadron discrimination. However, to arrive at a solid conclusion regarding the choice of particle type for the timing calibration it was necessary to use a sample of tracks from $Z \rightarrow \mu\mu$ events. Having arrived at the conclusion that choosing muons or jets has virtually no impact on the calibration result, the NBI group is planning to use inclusive muons to achieve the cell-based calibration.

From equation 7.1.6 error propagation gives that the accuracy of the β measurement increases with the distance to the calorimeter cell d_{cell} according to the expression

$$\sigma_\beta = \frac{\beta^2 c}{d_{\text{cell}}} \tag{14.0.1}$$

assuming that the error on d_{cell} is negligible compared to the time uncertainty. A larger distance means a smaller relative error at the same value of β. The uncertainty on the timing measurement is worse in the endcap calorimeters, but not enough to counter the increase in accuracy from the distance. In a future analysis, this could be taken into account by making the σ_β cut dependent on d_{cell}. This could also be done on cell-level by requiring a specific data efficiency when determining the σ_β selection cut for each cell. This would take into account not just the distance to the cell, but also the distribution of energy depositions and the resulting values of σ_t, thereby giving an optimal cut for each cell. The cut on all cells could then be defined and varied through the desired data efficiency.

A detail that was only briefly mentioned through figure 3.3 is the possibility of producing a single gluino together with a squark. The theoretically predicted production cross section from Prospino used in the search assumes gluino pair production, and if the production rate from the diagrams resulting in a single gluino is non-negligible, this could in principle alter the result of the search.

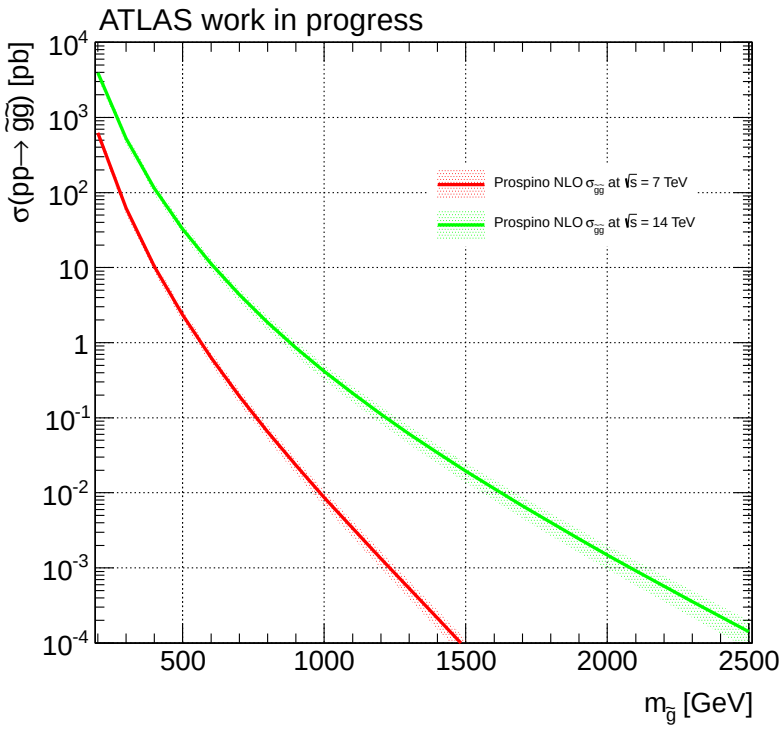

Figure 14.1: Gluino pair production cross sections simulated with Prospino at center-of-mass energies of 7 and 14 TeV, the latter of which the LHC is expected to reach in late 2014 or early 2015.

Advantages in future data sets

The full integrated luminosity collected in 2012 is predicted to reach roughly 20 fb^{-1}. This would give a total data sample of 25 fb^{-1}. Disregarding the increase in center-of-mass energy to 8 TeV and any other differences in operating parameters compared to 2011, a naïve projection of the possibilities for limit setting on gluino-based R-hadrons in the zero-background regime could then be given as a result of the five-fold increase in integrated luminosity through equation 11.2.4. Instead of the $\sim$ 8 fb it would be possible to reach an exclusion of $8/5 \simeq$ 1-2 fb, giving a mass exclusion approaching 1200 MeV.

After the scheduled long shutdown beginning in early 2013 the LHC is planned to begin collisions at its design center-of-mass energy of 13-14 TeV and with a bunch crossing interval of 25 ns in late 2014 or early 2015. Increasing the bunch crossing rate will result in a worse collision environment for the muon trigger system regarding the detection of particles at low speeds, where out-of-time problems will increase. The trigger efficiency for R-hadron events is thus expected to drop, but may be partly saved by triggering on associated production of other particles with high speeds. The increase in pileup at higher luminosities is expected to have little impact on the discovery potential for R-hadrons as the change in signal efficiency with pileup conditions estimated in chapter 10 is low and will be overshadowed by the increase in statistics. However, the greatest advantage comes

from the increase in center-of-mass energy. Comparing the gluino pair production cross sections as a function of mass given in figure 14.1 for $\sqrt{s} = 7$ TeV and 14 TeV, we see the cross sections increase by 1–2 orders of mangitude. If the LHC shutdown is successful, it will reach its design luminosity of 10^{34} cm^{-2}s^{-1} giving a projected integrated luminosity over one year of ~ 40 fb^{-1}. Assuming similar signal efficiencies as in 2011 this will result in cross section limits of roughly 1 fb using the 2015 data alone, and a mass limit approaching 2 TeV.

Appendices

A Signal optimisation

When optimising the upper limit on the signal of a given process using a 95% confidence level under the signal+background hypothesis, the value of s_{up} depends on the number of observed events N and the estimated background b. This dependency is altered drastically in the high background limit going from $\mathrm{CL_{s+b}}$ to $\mathrm{CL_s}$. For the specific case of zero observed events The $\mathrm{CL_s}$ technique does not depend on the estimated background due to its normalisation with the value from $\mathrm{CL_b}$. The difference between the two methods is illustrated in figure A.1.

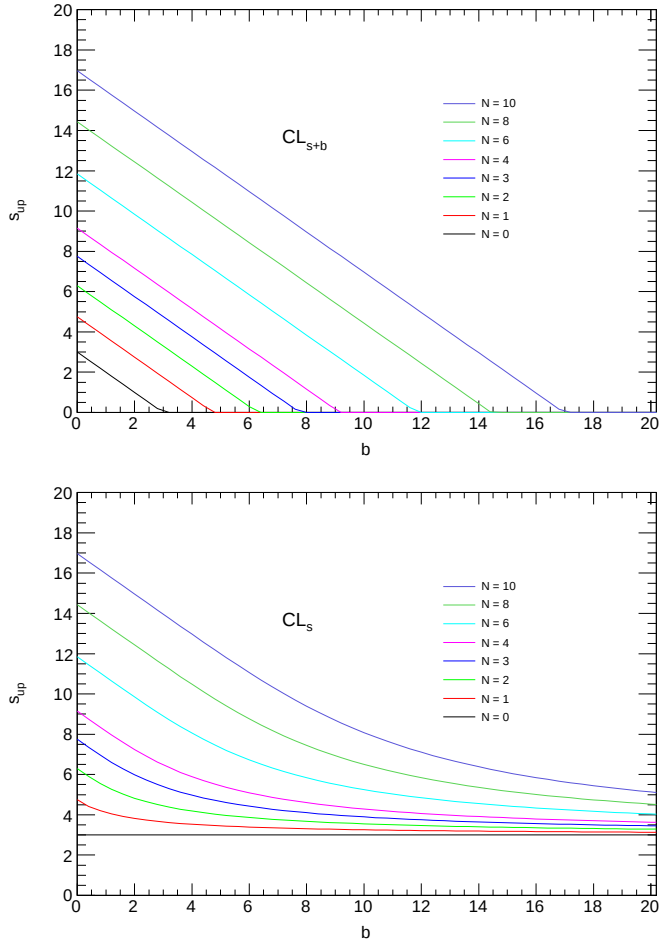

Figure A.1: Optimised signal s_{up} for a range of values of the observed number of events N and the background b given for $\mathrm{CL_{s+b}}$ (top) and $\mathrm{CL_s}$ (bottom). Notice the constant value for $N = 0$ in the case of $\mathrm{CL_s}$.

Acknowledgements

The writing of this thesis would not have been as rewarding or as enjoyable without the friendly atmosphere in the high energy physics group at the Niels Bohr Institute. The help and advice given to me by the people in the group have been an indispensable part of the process.

It has been a pleasure to work with Troels C. Petersen as my supervisor. The many informative talks we have had during the year about physics and data analysis have given me much new insight into experimental particle physics and have been paramount for my successfully completing the project.

My thanks also go out to Simon, Sascha and Morten from the SMP analysis team. Simon has been a great help with the many quirks of C++ programming in ROOT and SFrame. Sascha and Morten have also helped to guide me though the winding road of SMP searches.

Lastly, I also wish to thank my fellow students at the office: Bjørn, Lars, Gorm and Christian.

List of Figures

List of Tables

Bibliography

[1] K. Nakamura et al. (Particle Data Group), "The Review of Particle Physics," *JP G 37, 075021*, 2010.

[2] The ATLAS Collaboration, "The ATLAS Experiment at the CERN Large Hadron Collider," *J. Instrum.*, vol. 3, p. S08003. 437 p, 2008. Also published by CERN Geneva in 2010.

[3] L. Evans and P. Bryant, "Lhc machine," *JINST*, vol. 3, p. S08001, 2008.

[4] S. Hellman, M. Johansen, R. Mackeprang, P. Mermod, D. Milstead, C. Ohm, and A. Solodkov, "Measuring time-of-flight and identifying exotic stable massive particles with the ATLAS Tile calorimeter," Tech. Rep. ATL-COM-TILECAL-2009-028, CERN, Geneva, Nov 2009.

[5] M. Bajko et al., "Report of the Task Force on the Incident of 19th September 2008 at the LHC," Tech. Rep. LHC-PROJECT-Report-1168., CERN, Geneva, March 2008.

[6] M. E. Peskin and D. V. Schroeder, *An Introduction to Quantum Field Theory*. Westview Press, 1995.

[7] R. Leitner, V. V. Shmakova, and P. Tas, "Time resolution of the ATLAS Tile calorimeter and its performance for a measurement of heavy stable particles," tech. rep., CERN, Geneva, Mar 2007.

[8] W. H. Bell, *Minimum Bias Physics at the LHC with the ATLAS Detector*. Université de Genève, Section de Physique, 2009.

[9] R. J. Barlow, *Statistics: A Guide to the Use of Statistical Methods in the Physical Sciences*. John Wiley and Sons, 1989.

[10] P. R. Bevington and D. K. Robinson, *Data Reduction and Error Analysis for the Physical Sciences*. Mc Graw Hill, 3rd ed., 2003.

[11] B. Martin and G. Shaw, *Particle Physics*. WILEY, third ed., 2008.

[12] S. Menke, "ATLAS Physics Workshop," 2005.

[13] Forthommel, *Map of the CERN accelerator complex*. Date: 2012-09-07. http://en.wikipedia.org/wiki/CERN,.

[14] http://en.wikipedia.org/wiki/Standard_model. Date: 2012-09-07.

[15] ATLAS Luminosity Calculator: https://atlas-lumicalc.cern.ch.

[16] twiki.cern.ch/twiki/bin/viewauth/AtlasProtected/PileupReweighting.

[17] twiki.cern.ch/twiki/bin/viewauth/Atlas/PixelToTTuning.

[18] S. Schael *et al.*, "Precision electroweak measurements on the Z resonance," *Phys.Rept.*, vol. 427, pp. 257–454, 2006.

[19] ATLAS Collaboration, "Search for down-type fourth generation quarks with the ATLAS detector in events with one lepton and hadronically decaying W bosons," *Phys.Rev.Lett. 109, 032001*, 2012.

[20] Y. Fukuda et al, "Evidence for oscillation of atmospheric neutrinos," *Physical Review Letters 81 (8): 1562-1567*, 1998.

[21] D. Diakonov, V. Petro, and M. Polyakov, "Exotic anti-decuplet of baryons: prediction from chiral solitons," *Zeitschrift für Physik A 359 (3): 305*, 1997.

[22] The ATLAS Collaboration, "Observation of a New Particle in the Search for the Standard Model Higgs Boson with the ATLAS Detector at the LHC," *Physics Letters B716 1-29*, 2012.

[23] The CMS Collaboration, "Observation of a new boson at a mass of 125 GeV with the CMS experiment at the LHC," *Physics Letters B*, 2012.

[24] D. I. Kazakov, "Beyond the Standard Model (In Search of Supersymmetry)," *arXiv, hep-ph*, 2000.

[25] Sir Isaac Newton, Thomas Leseur and François Jacquier, *Philosophiæ Naturalis Principia Mathematica, volumes 1-2.* Jan 1822.

[26] The ATLAS Collaboration, "Public results," 2012.

[27] Necia Grant Cooper and Geoffrey B. West, *Particle Physics: A Los Alamos Primer.* 1988.

[28] M. Fairbairn, A. Kraan, D. Milstead, T. Sjöstrand, P. Skands, and T. Sloan, "Stable Massive Particles at Colliders," *Phys.Rept.438:1-63*, 2007.

[29] R. Mackeprang and D. Milstead, "An Updated Description of Heavy-Hadron Interactions in Geant4," *arXiv:0908.1868*, 2009.

[30] W. Beenakker, R. Höpker, M. Spira, and P. M. Zerwas, "Squarks and Gluino Production at Hadron Colliders," *Nucl. Phys. B492:51-103*, 1997.

[31] G. Farrar and P. Fayet *Phys. Lett. B76*, 1978.

[32] The Super-Kamiokande Collaboration, "Search for Proton Decay into Muon plus Neutral Kaon in Super-Kamiokande I, II, and III," *Phys. Rev. D 86, 012006*, 2012.

[33] P. Gambino, G. F. Giudice, and P. Slavich, "Gluino Decays in Split Supersymmetry," *Nucl.Phys. B726 35-52*, 2005.

[34] A. C. Kraan, *Interactions and Detection of R-Hadrons.* PhD thesis, University of Copenhagen, Niels Bohr Institute, Nov 2004.

[35] A. C. Kraan, "Interactions of heavy stable hadronizing particles," *Eur.Phys.J. C37 91-104*, 2004.

[36] S. Alekhin, J. Blumlein, and S. Moch, "Parton distribution functions and benchmark cross sections at NNLO," *arXiv:1202.2281*, 2012.

[37] J. C. Collins, D. E. Soper, and G. Sterman, "Factorization of Hard Processes in QCD," *arXiv:hep-ph/0409313v1*, 2004.

[38] P. Abreu et al, "Performance of the DELPHI Detector," *Nucl. Instrum. Meth. Phys Res. A378*, 1996.

[39] G. Cowan, *Statistical Data Analysis.* 1998.

[40] A. L. Read, "Modified Frequentist Analysis of Search Results (The CL_s Method)," *CERN open 2000-205*, 2000.

[41] A. L. Read, "Presentation of search results: the CL_s technique," *J. Phys. G: Nucl. Part. Phys. 28 2693*, 2002.

[42] G. Cowan, K. Cranmer, E. Gross, and O. Vitells, "Asymptotic formulae for likelihood-based tests of new physics," *Eur. Phys J. C71:1554*, 2011.

[43] S. Mehlhase, T. C. Petersen, L. Rossi, and S. Tarem, "Searches for heavy long-lived sleptons and R-hadrons with the ATLAS detector in pp collisions at $\sqrt{s} = 7$ TeV," *Phys. Lett. B.*, 2012.

[44] I. Ihrke, "Some notes on ellipses." University of Saarland, February 2011.

[45] "Luminosity Determination in pp Collisions at $\sqrt{s} = 7$ TeV using the ATLAS Detector in 2011," Tech. Rep. ATLAS-CONF-2011-116, CERN, Geneva, Aug 2011.

[46] ATLAS statistics forum, "Frequentist Limit Recommendation," June 2011.

[47] J. Ambjørn and J. L. Petersen, *Quantum Field Theory - lecture notes.* 1999.

[48] J. H. Christenson, J. Cronin, V. L. Fitch, and R. Turlay, *Evidence for the 2π Decay of the K_2^0 Meson.* 1964.

[49] The Geant4 documentation working group, "Physics Reference Manual," 2011.

[50] A. Martin, W. Stirling, and G. W. R.S. Thorne, "Parton distributions for the LHC," *Eur. Phys. J.C63:189-285*, 2009.

[51] M. Spangenberg and R. Matin, "Investigating high-threshold hits in the TRT-detector of ATLAS," 2010. Project for the Applied Statistics course at NBI.

[52] M. D. Jørgensen, "Search for long lived massive particles with the ATLAS detector at the LHC," *Niels Bohr Institute, University of Copenhagen*, 2010.

[53] Private communications with Troels C. Petersen. 2012.

[54] Private communications with Guillaume Unal. 2012.